New Physics in Double Higgs Production at NLO

by

Bo-Yan Huang
B.S., National Tsing Hua University, 2006
M.S., National Taiwan University, 2008

Thesis submitted in partial fulfillment of the requirements
for the degree of Doctor of Philosophy in Physics
in the Graduate College of the
University of Illinois at Chicago, 2021

Chicago, Illinois

Defense Committee:
Wai Yee Keung, Chair and Advisor
Piotr Gmytrasiewicz, Computer Science
Mikhail Stephanov
Ho-Ung Yee
Zhen-Yu Ye

This thesis is dedicated to my family,

for their infinite love and support

ACKNOWLEDGMENTS

Firstly, I would like to show my sincere gratitude here to my advisor Prof. Keung for his inspiration, helpful advice and continuous support during my Ph.D study. I appreciate the rest of my thesis committee: Prof. Piotr Gmytrasiewicz!, Prf. Mikhail Stephanov, and Prof. James Unwin, Prof. Ho-Ung Yee, and Prof. Zhen-Yu Ye, for their keen comments and suggestions.

I would also like to thank my peers Dr. Shi Yong Li, Qing Yun Wang, and Xiao Wang for their helpful advises and discussions.

I am extremely grateful to my family, who encourage me all the time wholeheartedly. Lastly, I would like to thank all of my friends I met during my life, for all the great time we have had together.

CONTRIBUTION OF AUTHORS

In Chapter 4, calculations of amplitude for NLO $qg \to qHH$ were done by Bo-Yan Huang. The calculations of the simulations in Chapter 5 were also done by Bo-Yan Huang.

TABLE OF CONTENTS

TABLE OF CONTENTS (Continued)

CHAPTER **PAGE**

LIST OF TABLES

LIST OF FIGURES

LIST OF FIGURES (Continued)

FIGURE **PAGE**

LIST OF FIGURES (Continued)

SUMMARY

After observing the Higgs boson by the ATLAS and CMS experiments at the LHC, accurate measurements of its properties, which allow us to study the electroweak symmetry breaking mechanism, become a high priority for particle physics. The most promising of extracting the Higgs self-coupling at hadron colliders is by examining the double Higgs production, especially in the $b\bar{b}\gamma\gamma$ channel. In this work, we presented full loop calculation for both SM and New Physics effects of the Higgs pair production to next-to-leading-order (NLO), including loop-induced processes $gg \to HH$, $gg \to HHg$, and $qg \to qHH$. We also included the calculation of the corrections from diagrams with only one QCD coupling in $qg \to qHH$, which was neglected in the previous studies. With the latest observed limit on the HH production cross-section, we studied the constraints on the effective Higgs couplings for the LHC at center-of-mass energies of 14 TeV and a provisional 100 TeV proton collider within the Future-Circular-Collider (FCC) project. To obtain results better than using total cross-section alone, we focused on the $b\bar{b}\gamma\gamma$ channel and divided the differential cross-section into low and high bins based on the total invariant mass and p_T spectra. The new physics effects are further constrained by including extra kinematic information. However, some degeneracy persists, as shown in previous studies, especially in determining the Higgs trilinear coupling. Our analysis shows that the degeneracy is reduced by including the full NLO corrections.

CHAPTER 1

INTRODUCTION

In 2012, a new scalar resonance [4, 5] with a mass of 125.09 ± 0.24 GeV [6] was discovered at the Large Hadron Collider (LHC). After analyzing all the Run I data, the Standard Model (SM) Higgs boson provides best explanation for the measured properties of the new particle [7, 8, 9, 10, 11, 12]. Since then, high priority analyses at the Large Hadron Collider (LHC) always include the detailed study of the properties of this particle.

Theoretical uncertainties limit the reachable accuracies at the LHC. However, a wider range of Higgs couplings investigated at the LHC, and the increase of the variety of processes that involves the Higgs boson can partially compensate for this restriction. The most constrained condition is the gauge-Higgs coupling $C_v \equiv g = 0.94 + 0.11$, which is very close to the SM expectation. Furthermore, due to the fact that the observed Higgs candidate particle is produced at roughly the SM rate, the extensions of the Higgs sector beyond the Standard Model are extremely constrained.

A simple model with a fourth generation of heavy quarks, for example, is excluded by the limits on Higgs production for any Higgs mass below around 600 GeV [13, 14] since such model predicts large deviations in the Higgs production rates from SM value [15, 16, 17, 18, 19]. Unlike C_v, the Yukawa couplings of top-Higgs and bottom-Higgs are not constrained precisely by the data up to date. Moreover, they are within $30 - 40\%$ of the SM expectations [20, 21].

Testing the Higgs boson's self-interactions is particularly interesting. It is the only unmeasured experimentally property of the Higgs boson and provides the only window to probe the Higgs scalar potential, which is the origin of spontaneous symmetry breaking of the gauge symmetry and the origin of the particle masses in the Standard Model.

1.1 Trilinear Higgs Coupling

One of the most promising probes is Higgs pair production at the LHC. These processes provide direct measurements of the trilinear Higgs self-couplings at leading-order. Moreover, these processes complement indirect effects caused by the self-interactions of Higgs bosons in single-Higgs processes and radiative corrections to electroweak observables [22, 23] contaminated by possible interference effects with different models of New Physics.

Unfortunately, the Standard Model expectation of this production rate is only 0.034 pb at the Large Hadron Collider with CM energy equal to 14 TeV [24]. One of the reasons for such a low rate is that the SM contributions from the box diagram in Figure 3(a) and the triangle diagram in Figure 3(b) interfere destructively near kinematic threshold [25]. However, the Standard Model cross-section rises dramatically to 1.54 pb at a future 100 TeV proton-proton collider since the luminosity increases in the parton distribution function of gluon at lower x, the Bjorken scale, which provides a chance to measure the Higgs self-couplings precisely [26, 27].

The SM Higgs potential describes the self-interactions of Higgs bosons, and it reads

$$V = \frac{\lambda}{2}\left(\phi^\dagger\phi - \frac{v^2}{2}\right)^2, \tag{1.1}$$

where v denotes the vacuum expectation value (vev) , and λ is the strength of SM Higgs field self-interaction and ϕ is the Higgs doublet, which reads

$$\phi = \begin{pmatrix} 0 \\ \\ \frac{v+H}{\sqrt{2}} \end{pmatrix} \tag{1.2}$$

in unitary gauge with H denoting the physical Higgs field. In the Standard Model, the Higgs mass is $m_H = \sqrt{2\lambda v^2}$. By expanding Equation 1.1 around the vev in terms of the Higgs field, we can write the Higgs self-couplings as

$$g_{H^3} = 3\frac{m_H^2}{v}, \qquad g_{H^4} = 3\frac{m_H^2}{v^2}\,, \tag{1.3}$$

where g_{H^4}, and g_{H^3} are the quartic and trilinear Higgs self-coupling, respectively.

Four major classes of processes are responsible for the production of Higgs pair at hadron colliders. First, we have $gg \to HH$, the gluon fusion process, with a loop of heavy quark, which has a strong coupling to the Higgs boson [28, 29, 30, 31]. The second class is $qq' \to qq'V^*V^* \to qq'HH$ $(V = Z, W)$, the vector bosons fusion (VBF) processes, which generate two jets and two Higgs bosons in the final state [28, 32, 33, 34, 35]. The third class is $q\bar{q}' \to V^* \to VHH$ $(V = Z, W)$, the double Higgs–strahlung process, where a vector boson, W or Z, radiates the Higgs bosons [36]. The last one has associated producing a pair of top quarks with two Higgs bosons, $pp \to t\bar{t}HH$ [37].

Compared to single Higgs production, these processes have at least two orders of magnitude smaller production cross-sections as the phase space is small since the final state consists of two heavy particles. They have electroweak couplings of higher-order. Besides, other topologies which are irrelevant to the trilinear Higgs coupling, where the gauge boson or fermion lines radiate both Higgs bosons, which produce the same final state as the diagrams with $H^* \to HH$ splitting. Thus, these topologies pollute the correlation between the g_{H^3} coupling and the double Higgs production rate. It is extremely difficult to measuring the trilinear Higgs coupling, and very high energies along with very high collider luminosities are therefore required.

1.2 Next-to-Leading Order and Beyond Standard Model

It is almost impossible to measure the quartic Higgs coupling, g_{H^4}, in the near future as an extra v further suppresses it in the denominator compared to the triple Higgs self-coupling, and the smallness of the triple-Higgs production rate prohibit it from being probed directly [38, 39, 40, 41, 42][1]. We can directly measure the trilinear Higgs coupling through Higgs-pair production, where Higgs pairs are dominantly produced in the gluon-fusion process mediated mainly by top-quark loops while the contribution of b-quark loops is negligible. Two types of diagrams, triangle, and box, contribute to the gluon-fusion process $gg \to HH$, where the triangle diagrams involve the trilinear Higgs coupling, and the interference between the one-loop box and triangle diagrams are destructive [29, 31]. The dominant contributions to the cross-section come from the box diagrams. The approximate relation, $\Delta\sigma/\sigma \sim -\Delta g_{H^3}/g_{H^3}$, gives a

[1]The quartic Higgs coupling is indirectly constrained by Higgs pair production [43, 44, 45].

rough estimate of the correlation of the size of the trilinear Higgs self-coupling in the vicinity of the SM value of g_{H^3} and the cross-section. Therefore, small uncertainties of the relevant cross-section, which can be achieved by calculating higher-order corrections, are required to determine the trilinear Higgs coupling. The next-to-leading order (NLO) QCD corrections [46, 47, 48] and next-to-next-to-leading order (NNLO) corrections, which adopt heavy top quark approximation [49, 50, 51], are fully known. The NLO corrections are significant, and therefore must be included. Comparing NLO corrections, the NNLO contributions are much smaller but still considerable. The QCD next-to-next-to-next-to-leading order (N^3LO) corrections to the effective couplings of Higgs and Higgs-pair to gluons are recently computed in heavy top quark approximation limit [52] and lead to a minor modification to the cross-section [53, 54, 55]. The LO contributions and the higher-order corrections contribute equally to the total production rate. Lately, the NLO results have been matched to parton showers [56, 57], and the NLO mass effects with the additional top-mass effects in the double-real corrections have been merged with the full NNLO QCD results in the heavy-top limit [58]. The full NLO QCD corrections to the production of Higgs pair with the anomalous trilinear Higgs self-coupling effects have been calculated in [24]. In this work, we calculated full NLO results, including weak interaction contributions from $qg \to HHq$.

Although verifying that a scalar vev spontaneously breaks the electroweak symmetry is crucial, discovering new physics beyond the SM is always the final goal. Multiple new physics that could potentially affect this specific channel must be considered while analyzing the double Higgs production. One possible new physics from a new diagram involving the anomalous

quartic coupling, $HHt\bar{t}t$, as shown in Figure 3(c) could give significant effect [59, 60, 61]. The presence of this quartic coupling makes the total production rate insensitive to the Higgs self-coupling and makes measuring this coupling incredibly difficult [62],.

1.3 Recent Searches in a Rare Particle Decay

The most significant double Higgs decay channel in the important low-mass region is the bottom quark pair plus photons pair channel, $HH \to \gamma\gamma b\bar{b}$. Recently, new analysis techniques for searching this rare process have been developed by physicists in ATLAS collaboration. To optimize the sensitivity to the self-coupling of Higgs bosons, they first split the pp collision events into low and high invariant mass groups. After that, they used a multivariate discriminant (Boosted Decision Tree) to separate the events that can be categorized as the $HH \to \gamma\gamma b\bar{b}$ process from those that can not. Finally, the Higgs-pair production rate is determined first, and then they observed how the production rate varies as a function of the Higgs boson self-coupling to its SM value ratio λ/λ_{SM}. By using the above procedures, the ATLAS team constrained the self-coupling of Higgs boson and allowed it to vary between -1.5 and 6.7 times the SM value. Physicists, therefore, can set a currently best limit on the Higgs pair production rate of 4.1 times the SM value.

However, the work is far from being done. A huge amount of data is required to precisely measure the Higgs self-coupling and see if it were close to its SM value. The High-Luminosity upgrade of the LHC, scheduled to be operational in the late 2020s, is planned to operate at higher collision energy and deliver a dataset 20 times larger than used in this analysis. The Higgs pair production will be observed in this huge dataset if the Higgs pair production indeed

behaves as predicted by the Standard Model, and a more quantitative statement will be made on the strength of the Higgs boson self-coupling.

1.4 Overview of This Thesis

This paper aims to learn how multiple new physics effects interplay in different kinematic distributions and the total cross-section at next-to-leading order. To research the topic more thoroughly, we also study the distributions of differential cross-sections, especially the invariant mass of the Higgs pair, m_{HH}, and the transverse momentum p_T. We study the LHC at center-of-mass energies of 14 TeV and a planning 100 TeV pp collider in the project of Future-Circular-Collider (FCC) [2, 3].

This thesis is organized as follows. In Chapter 2, we introduce the Glashow-Salam-Weiberg model and the Standard Model Lagrangian. In Chapter 3, we discuss the required techniques and relevant formulas to compute one-loop integrals. In Chapter 4, the notation and the details of our calculation at LO and NLO are presented. We then perform the numerical analysis in Chapter 5. Finally, the conclusions are given in Chapter 6.

CHAPTER 2

THE STANDARD MODEL

In present-day particle physics, the Standard Model is the most successful theory that describesthe electromagnetic, weak, and strong interactions, except the gravitational force, in the universe and governs elementary particles discovered. The Standard Model was developed in stages throughout the latter half of the 20th century through many scientists worldwide. In the mid-1970s, experimental confirmation of the existence of quarks finalized the current formulation. The modern form of quantum electrodynamics (QED) has been established by Feynman [63], Tomonaga [64], and Schwinger [65] in the late '40s, which is still the most precise known physics theory. The abelian gauge theory, was extended to non-abelian groups to explain strong interactions by Chen Ning Yang and Robert Mills [66] in 1954. Although the non-abelian gauge theory was first designed for strong interaction, it was also used for describing weak interaction. At low energies, the electromagnetic can be accurately described by the quantum electrodynamics (QED) while the weak interactions can be described by the Fermi model. Nevertheless, it turns out that these two interactions can be described by a single model, the Glashow-Salam-Weinberg (GSW) model, which was proposed by Glashow [67], Salam [68], and Weinberg [69] in the 60s. Until now, it is still the most comprehensive theory that unifies electromagnetism with weak interaction. The GSW model is self-consistent and minimal, since the known experimental results of electroweak origin can be described by this model with the fewest necessary degrees of freedom.

The last piece of the Standard Model is strong interaction. The theory of the strong interaction, quantum chromodynamics (QCD), contributed by many, acquired its modern form in 1973 when asymptotic freedom was proposed [70, 71] and experiments confirmed that the hadrons were composed of fractionally charged quarks.[72, 73]

The term "Standard Model" was first proposed by Abraham Pais and Sam Treiman in 1975, regarding the electroweak theory with four quarks (up, down, charm, and strange quarks).

Initially, $SU(2)_W \times U(1)_Y$, used to describe unified electroweak interactions, gives rise to the massless gauge bosons. However, we know from the experiment that there are four gauge bosons, three are massive, and the other is massless. To resolve this inconsistency, the Higgs mechanism [7, 8, 9, 10, 11, 12], is introduced. The Higgs mechanism gives rise to the masses of all the elementary particles, including the masses of the W and Z bosons, and the masses of the fermions, i.e., the quarks and leptons. The gauge symmetry of non-abelian $SU(2)_W \times U(1)_Y$ is spontaneously broken by introducing a scalar field which preserves invariance under the transformation of electromagnetic subgroup, $U(1)_{em}$, and has a non-vanishing vacuum expectation value. Due to different representations of the gauge group for left-handed and right-handed fermions, the Standard Model is chiral. In the symmetric theory, fermion masses are forbidden, but they can be recovered by introducing spontaneous symmetry breaking. We obtain the quark mixing matrix, also called the CKM matrix, which is the reason for CP-violation by diagonalizing the fermion mass matrices. Although the model does not fix the number of generations of fermions, only three generations of quarks with light neutrinos are allowed due to the experiment constraints [74].

The Standard Model is free of anomalies and renormalizable, as proved by 't Hooft [75, 76], and therefore allows the perturbative computation of unique quantum corrections for observable quantities with finite number of input parameters.

The classical Lagrangian $\mathcal{L}_C$ of the SM is composed of gauge invariant sectors and can be written as

$$\mathcal{L}_C = \mathcal{L}_G + \mathcal{L}_H + \mathcal{L}_F \,, \tag{2.1}$$

where G, H and F denote Gauge field, Higgs, and Fermion field Lagrangians respectively.

2.1 The Gauge Field Lagrangian

The gauge field Lagrangian is

$$\mathcal{L}_G = -\frac{1}{4}\left(\partial_\mu W^a_\nu - \partial_\nu W^a_\mu + g_2 \varepsilon^{abc} W^b_\mu W^c_\nu\right)^2 - \frac{1}{4}\left(\partial_\mu B_\nu - \partial_\nu B_\mu\right)^2 , \tag{2.2}$$

where the isosinglet B_μ and the isotriplet W^a_μ, $a = 1, 2, 3$ associates to the weak hypercharge Y_W of the group $U(1)_Y$ and the generators I^a_W of the weak isospin group $SU(2)_W$, respectively, and ε^{abc} are the totally antisymmetric structure constants of $SU(2)$. The four gauge fields transform according to the adjoint representation $SU(2)_W \times U(1)_Y$. The covariant derivative is given by

$$D_\mu = \partial_\mu - i g_2 I^a_W W^a_\mu + i g_1 \frac{Y_W}{2} B_\mu, \tag{2.3}$$

where g_1 and g_2 are the $U(1)_Y$ and $SU(2)_W$ gauge coupling.

From the Gell-Mann Nishijima relation, we can write Q, the electric charge operator,in terms of the weak hypercharge and the weak isospin generator I_W^3.

$$Q = I_W^3 + \frac{Y_W}{2}. \tag{2.4}$$

2.2 The Higgs Lagrangian

The Higgs Lagrangian can be written as

$$\mathcal{L}_H = (D_\mu \Phi)^\dagger (D^\mu \Phi) - V(\Phi), \tag{2.5}$$

where ϕ is a complex $SU(2)_W$ doublet field with hypercharge $Y_W = 1$

$$\Phi(x) = \begin{pmatrix} \phi^+(x) \\ \\ \phi^0(x) \end{pmatrix}, \tag{2.6}$$

and the Higgs potential has the following form

$$V(\Phi) = \frac{\lambda}{4}\left(\Phi^\dagger \Phi\right)^2 - \mu^2 \Phi^\dagger \Phi. \tag{2.7}$$

To create spontaneous symmetry breaking, the parameters λ and μ are chosen to minimize the potential $V(\Phi)$ with non-zero vacuum expectation value, $\langle \Phi \rangle$, for the Higgs field.

2.3 Spontaneous Symmetry Breaking

The Standard Model is constructed so that the following relation is satisfied for the classical ground state of the scalar field.

$$|\langle\Phi\rangle|^2 = \frac{v^2}{2} = \frac{2\mu^2}{\lambda} \neq 0 \; . \tag{2.8}$$

The field expands around the ground state in perturbation theory while the phase of the field is chosen to preserve electromagnetic gauge invariance $U(1)_{em}$, and the doublet Higgs field can be written as

$$\Phi(x) = \begin{pmatrix} \phi^+(x) \\ \\ \frac{1}{\sqrt{2}}\big(v + H(x) + i\chi(x)\big) \end{pmatrix}, \tag{2.9}$$

where H, χ, and ϕ^+ are chosen to have zero vacuum expectation values. It is possible to eliminate the unphysical fields $\phi^\pm$ and χ by properly chose gauge transformation, i.e., the unitary gauge. The physical scaler field, H, has mass

$$M_H = \sqrt{2}\mu. \tag{2.10}$$

By inserting Equation 2.9 into $\mathcal{L}_C$ and diagonalizing the corresponding mass matrices, the physical gauge boson and fermion fields can be written as follows

$$\begin{aligned} W_\mu^\pm &= \tfrac{1}{\sqrt{2}}\left(W_\mu^1 \mp i W_\mu^2\right), \\ \begin{pmatrix} Z_\mu \\ A_\mu \end{pmatrix} &= \begin{pmatrix} c_W & s_W \\ -s_W & c_W \end{pmatrix} \begin{pmatrix} W_\mu^3 \\ B_\mu \end{pmatrix}, \\ f_i^L &= U_{ik}^{f,L} f'^L_k, \\ f_i^R &= U_{ik}^{f,R} f'^R_k, \end{aligned} \tag{2.11}$$

where

$$c_W = \cos\theta_W = \frac{g_2}{\sqrt{g_2^2 + g_1^2}}, \quad s_W = \sin\theta_W, \tag{2.12}$$

while f stands for fermions, l, ν, u or d, and θ_W is the weak mixing angle, also called Weinberg angle. The masses can be defined as

$$\begin{aligned} M_W &= \tfrac{1}{2} g_2 v, \qquad M_Z = \tfrac{1}{2}\sqrt{g_1^2 + g_2^2}\, v, \\ M_\gamma &= 0, \qquad m_{f,i} = U_{ik}^{f,L} G_{km}^f U_{mi}^{f,R\dagger} \tfrac{v}{\sqrt{2}}. \end{aligned} \tag{2.13}$$

From Equation 2.12 and Equation 2.13, we have

$$c_W = \frac{M_W}{M_Z}. \tag{2.14}$$

The neutrino masses would become nonzero, which contradict current experimental results, if we added the right-handed neutrinos into the model. Therefore, there is no right-handed neutrinos in the Standard Model.

The coupling of the electron to the photon field A_μ can be identified as the electrical charge, $e = \sqrt{4\pi\alpha}$. This yields

$$e = \frac{g_1 g_2}{\sqrt{g_1^2 + g_2^2}} \,. \tag{2.15}$$

The unitary quark mixing matrix is introduced by diagonalizing the fermion mass matrices.

$$V_{ij} = U_{ik}^{u,L} U_{kj}^{d,L\dagger} \tag{2.16}$$

For the lepton sector, there is no corresponding matrix. Therefore, $U^{\nu,L}$ is entirely arbitrary, and we can choose $U^{\nu,L}$ to cancel $U^{l,L}$. From the relations in (Equation 2.10, Equation 2.13, Equation 2.15, and Equation 2.16), we can replace the original set of parameters parameters

$$\lambda,\ \mu^2,\ g_1,\ g_2,\ G^l,\ G^u,\ G^d \tag{2.17}$$

by the physical parameters

$$M_H,\ M_W,\ M_Z,\ m_{f,i},\ e,\ V_{ij}. \tag{2.18}$$

Thus the Lagrangian Equation 2.1 can be expressed in terms of physical fields and parameters.

2.4 Fermion Field Lagrangian

The fermion field Lagrangian reads

$$\begin{aligned}\mathcal{L}_F &= \sum_i \left(\overline{L'}_i^L i\gamma^\mu D_\mu L'^L_i + \overline{Q'}_i^L i\gamma^\mu D_\mu Q'^L_i\right) \\ &+ \sum_i \left(\overline{l'}_i^R i\gamma^\mu D_\mu l'^R_i + \overline{u'}_i^R i\gamma^\mu D_\mu u'^R_i + \overline{d'}_i^R i\gamma^\mu D_\mu d'^R_i\right) \\ &- \sum_{ij} \left(\overline{L'}_i^L G^l_{ij} l'^R_j \Phi + \overline{Q'}_i^L G^u_{ij} u'^R_j \tilde{\Phi} + \overline{Q'}_i^L G^d_{ij} d'^R_j \Phi + h.c.\right),\end{aligned} \tag{2.19}$$

where, L and Q denotes lepton and quark $SU(2)_W$ doublets (the colour index are dropped out for simplicity), respectively,

$$Q'^L_j = P_L Q'_j = \begin{pmatrix} u'^L_j \\ \\ d'^L_j \end{pmatrix}, \quad L'^L_j = P_L L'_j = \begin{pmatrix} \nu'^L_j \\ \\ l'^L_j \end{pmatrix}, \tag{2.20}$$

and the superscripts L, R denote the chirality. The explicit form of right-handed fermion singlets are

$$u'^R_j = P_R u'_j, \quad d'^R_j = P_R d'_j, \quad l'^R_j = P_R l'_j, \tag{2.21}$$

where $\tilde{\Phi}$is the charge conjugation of the Higgs field,n$\left(\phi^{0*}, -\phi^-\right)^T$, and $\phi^- = (\phi^+)^*$. The right-handed(left-handed) states are obtained by acting the right-handed(left-handed) projection operator, $P_{R(L)} = \frac{1+(-)\gamma_5}{2}$, on a spinor. u, d, ν and l denote up quarks and down quarks,

leptons, and neutrinos, respectively, while i, j are the generation indexes. The term involving g_2 is absent in D_μ for right-handed fermions as they are $SU(2)_W$ singlets.

The covariant derivatives are diagonalized by defining the weak eigenstates of the fermions as the primed fermion fields. G^l_{ij}, G^u_{ij} and G^d_{ij} are the Yukawa coupling matrices that determine the fermion masses.

2.5 Gauge fixing

To calculate $\mathcal{L}_C$ to higher-order, the gauge needs to be fixed. We choose a renormalizable Feynman-'t Hooft gauge, which equals to $\Xi = 1$ in $R\Xi$ gauge, where most computations of Quantum Field Theories are simplest in this gauge.

$R\Xi$ gauge has the following linear gauge fixings.

$$\begin{aligned} F^\pm &= (\xi_1^W)^{-\frac{1}{2}}\partial^\mu W_\mu^\pm \mp iM_W(\xi_2^W)^{\frac{1}{2}}\phi^\pm, \\ F^Z &= (\xi_1^Z)^{-\frac{1}{2}}\partial^\mu Z_\mu - M_Z(\xi_2^Z)^{\frac{1}{2}}\chi, \\ F^\gamma &= (\xi_1^\gamma)^{-\frac{1}{2}}\partial^\mu A_\mu. \end{aligned} \tag{2.22}$$

The gauge fixing Lagrangian can be written as

$$\mathcal{L}_{fix} = -\frac{1}{2}\left[(F^\gamma)^2 + (F^Z)^2 + 2F^+F^-\right]. \tag{2.23}$$

To maintain the consistency of the path integral formulation, Faddeev Popov ghosts $u^\alpha(x)$, $\bar{u}^\alpha(x)$ $(\alpha = \pm, \gamma, Z)$ is introduced with the Lagrangian

$$\mathcal{L}_{FP} = \bar{u}^\alpha(x) \frac{\delta F^\alpha}{\delta \theta^\beta(x)} u^\beta(x), \tag{2.24}$$

where F^α is the gauge fixing operators and the infinitesimal gauge transformations is characterized by $\theta^\beta(x)$.

Notice that poles of transverse gauge fields at the lowest order coincide with the corresponding poles of the longitudinal gauge fields, ghost fields , and unphysical Higgs fields.

Finally, the complete renormalizable Lagrangian for the Standard Model is

$$\mathcal{L}_{SM} = \mathcal{L}_C + \mathcal{L}_{fix} + \mathcal{L}_{FP} \, . \tag{2.25}$$

CHAPTER 3

ONE-LOOP INTEGRALS

The methods of calculating loop integrals are first developed by Passarino and Veltman[77, 78], 't Hooft and Veltman [79], and Melrose [80]. They are further extended by Denner [81, 82, 83, 84]. In this chapter, we show the classification of these loop integrals and the techniques required.

3.1 Definitions

In quantum field theory (QFT), the generic one-loop computations have the following form

$$T_N \sim \int \frac{\mathrm{d}^4 q}{(2\pi)^4} \frac{\mathcal{N}(q)}{((q+p_0)^2 - m_0^2)((q+p_1)^2 - m_1^2)....((q+p_{N-1})^2 - m_{N-1}^2)}, \tag{3.1}$$

where the number of external particles is denoted by N (see Figure 1), and the momentum of external particles are defined as

$$p_{i0} = p_i \quad \text{and} \quad p_{ij} = p_i - p_j. \tag{3.2}$$

The integral T_N will be ultraviolet (UV) divergent if $\mathcal{N}(q)$ has the loop momentum q in a high enough power. By naive power counting, we can easily see that the ultraviolet divergence occurs when $\mathcal{N}(q)$ has rank r tensor integrals, where $r + 4 \geq 2n$ for an n-point integral. Moreover, two- and one-point scalar integrals diverge in the ultraviolet region. Notice that n

is the highest possible rank for an n-point one-loop integral. Therefore, n-point integrals can only be UV-divergent when $n < 5$, and they are always UV-finite when $n \geq 5$. The most common way to regulate the loop integrals is the dimensional regularization [85], regularizes the ultraviolet divergences by setting the dimensionality $D = 4-2\epsilon$ and takes the limit $\epsilon \to 0$ at the final step. This regularization method generalizes the dimensionality of the loop momentum q to D and the integration in Equation 3.1 becomes Equation 3.3

$$\frac{d^4q}{(2\pi)^4} \to \frac{d^Dq}{(2\pi)^D}. \tag{3.3}$$

For example if we have an q^4 integral with $\mathcal{N}(q) = q_\mu q_\nu q_\rho q_\delta$. The divergence is insensitive to external kinematic parameters since the power counting shows that it is logarithmic. Therefore, we can isolate the divergence by using

$$q_4 \to \int \frac{\mathrm{d}^Dq}{(2\pi)^D} \frac{q_\mu q_\nu q_\rho q_\delta}{[d(q)]^4} = \frac{(g_{\mu\nu}g_{\rho\delta} + g_{\mu\rho}g_{\nu\delta} + g_{\mu\delta}g_{\nu\rho})}{D(D+2)} \int \frac{\mathrm{d}^Dq}{(2\pi)^D} \frac{q^4}{[d(q)]^4}, \tag{3.4}$$

where $d(q) = q^2 - \mu^2$ and the kinematic invariant, μ, is used to regularize the divergences at small q^2. We can calculate the integral by using the following equation

$$\begin{aligned} \int \frac{d^Dq}{i\pi^{D/2}} \frac{(q^2)^r}{\left(q^2-\mu^2\right)^m} &= \frac{\Omega_D}{\pi^{D/2}} (-1)^{r-m} \mu^{D+2r-2m} \int_0^\infty dx \frac{x^{2r+D-1}}{(1+x^2)^m} \\ &= (-1)^{r-m} \mu^{D+2r-2m} \frac{\Gamma(r+D/2)\Gamma(m-r-D/2)}{\Gamma(D/2)\Gamma(m)}, \end{aligned} \tag{3.5}$$

where Ω_D is the D-dimensional solid angle, and $\Omega_D = 2\pi^{D/2}/\Gamma(D/2)$. For$D \neq 4$ with $m = 4$ and $r = 2$, Equation 3.5 gives a finite result. We can therefore regularize ultraviolet divergences from one-loop diagrams by using dimensional regularization. The parameter μ plays the role of a renormalization scale that keeps track of the correct dimension of the integral in D space-time dimensions.

Another type of singularity, collinear and soft divergences, occurs when the massless particles present appear when multiple propagators simultaneously are on the mass shell in the integrand and can also be regularized dimensionally.

Therefore, UV-divergent one-loop integrals with massless particles can be treated economically by using dimensional regularization with only one parameter $\epsilon = (4 - D)/2$. In this work, dimensional regularization is assumed to be applied to every loop integrals.

In the limit $\epsilon \to 0$, we can express T_N in terms of the scalar integrals including one- two-, three- and four-point integrals, and the rational part, $\mathcal{R}$, which is the remnant of dimensional regularization.

$$T_N = c_{4;j} I_{4;j} + c_{3;j} I_{3;j} + c_{2;j} I_{2;j} + c_{1;j} I_{1;j} + \mathcal{R} + \mathcal{O}(D - 4). \tag{3.6}$$

In Equation 3.6, we evaluate the coefficients $c_{N,j}$ ($N = 1, \ldots 4$ in $D = 4$ without dependence on ϵ. $I_{L;j}$ denotes the type j L-point scalar integral. The type j indicates the combinations of the external momenta p_{ii-1} that compose the q_i entering the main integrals in the right hand side of Equation 3.6. We can obtain Equation 3.6 by using the following two conditions:

First, the nature of four-dimensional space-time allows us to reduce Higher n-point scalar integrals to sums of four-point integrals, box diagrams. Second, the Lorentz invariance that makes decomposing tensor integrals to invariant form factors becomes possible. Thus, we can write a D-dimensional scalar five-point integral, pentagon diagram, as the sum of the five four-point integrals, obtainable by removing one propagator while neglecting $\mathcal{O}(D-4)$ terms. [80, 86, 87]. Similarly, we can recursively obtain the one-loop N-point function in D-dimensional spacetime, where $D = 4-2\epsilon$, as a linear combination of pentagon integrals [80, 86] for $N \geq 6$. From Equation 3.6, we can reduce the calculation of any one-loop integral to determining both the coefficients $c_{L;j}$ and the rational part $\mathcal{R}$ once we know every one-loop scalar integral with $N \leq 4$. As we will discuss in Section 3.6, we can also obtain the rational part and the reduction coefficients efficiently by numerical methods.

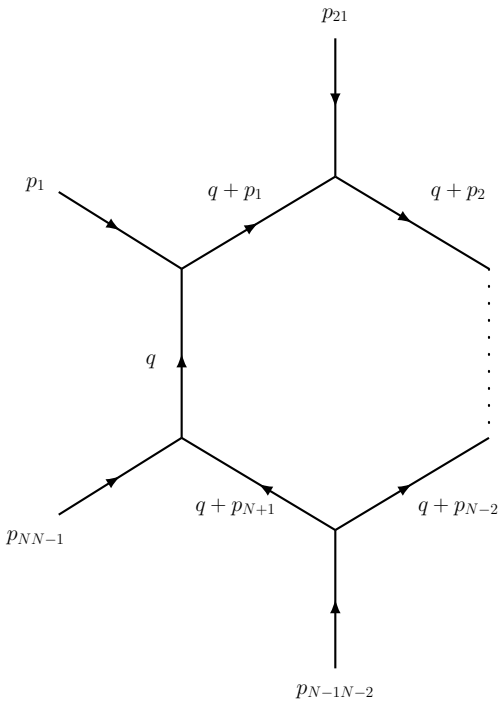

Figure 1. *The generic N-point integral.*

The general one-loop tensor integral shown in Figure 1 are defined as

$$T^N_{\mu_1\ldots\mu_r}(p_1,\ldots,p_{N-2},p_{N-1},m_0,\ldots,m_{N-2},m_{N-1}) = \frac{(2\pi\mu)^{4-D}}{i\pi^2}\int d^Dq \frac{q_{\mu_1}\cdots q_{\mu_r}}{D_0D_1\cdots D_{N-1}} \tag{3.7}$$

with

$$D_0 = q^2 - m_0^2 + i\varepsilon, \qquad D_i = (q+p_i)^2 - m_i^2 + i\varepsilon, \qquad i = 1,\ldots,N-1, \tag{3.8}$$

which is originated from the propagators in the Feynman diagrams. The tensor integrals are fully symmetric in the Lorentz indices μ_k. The singularities of the integral are regulated by introducing an infinitesimal imaginary part, $i\varepsilon$. The specific choice of this $i\varepsilon$ ensures causality and makes the logarithms and dilogarithms have correct imaginary parts after integration.

Conventionally, T^N is denoted by the N-th character in alphabetical order, i.e. $A \equiv T^1$, $B \equiv T^2$, ..., where the index 0 denotes the scalar integrals.

The tensor integrals are Lorentz covariance, which allows the metric tensor, $g_{\mu\nu}$, and the external momenta, p_i, as well as symmetric coefficient functions $T^N_{i_1 \ldots i_r}$ to reconstruct these tensor integrals.

For the lowest order integrals, the explicit Lorentz decompositions are

$$\begin{aligned} B_\mu &= p_{1\mu} B_1, \\ B_{\mu\nu} &= g_{\mu\nu} B_{00} + p_{1\mu} p_{1\nu} B_{11}, \end{aligned} \tag{3.9}$$

$$
\begin{aligned}
C_\mu &= p_{1\mu}C_1 + p_{2\mu}C_2 = \sum_{i=1}^{2} p_{i\mu}C_i, \\
C_{\mu\nu} &= g_{\mu\nu}C_{00} + p_{1\mu}p_{1\nu}C_{11} + p_{2\mu}p_{2\nu}C_{22} + (p_{1\mu}p_{2\nu} + p_{2\mu}p_{1\nu})C_{12} \\
&= g_{\mu\nu}C_{00} + \sum_{i,j=1}^{2} p_{i\mu}p_{j\nu}C_{ij}, \\
C_{\mu\nu\rho} &= (g_{\mu\nu}p_{1\rho} + g_{\nu\rho}p_{1\mu} + g_{\mu\rho}p_{1\nu})C_{001} + (g_{\mu\nu}p_{2\rho} + g_{\nu\rho}p_{2\mu} + g_{\mu\rho}p_{2\nu})C_{002} \\
&\quad + p_{1\mu}p_{1\nu}p_{1\rho}C_{111} + p_{2\mu}p_{2\nu}p_{2\rho}C_{222} \\
&\quad + (p_{1\mu}p_{1\nu}p_{2\rho} + p_{1\mu}p_{2\nu}p_{1\rho} + p_{2\mu}p_{1\nu}p_{1\rho})C_{112} \\
&\quad + (p_{2\mu}p_{2\nu}p_{1\rho} + p_{2\mu}p_{1\nu}p_{2\rho} + p_{1\mu}p_{2\nu}p_{2\rho})C_{122} \\
&= \sum_{i=1}^{2}(g_{\mu\nu}p_{i\rho} + g_{\nu\rho}p_{i\mu} + g_{\mu\rho}p_{i\nu})C_{00i} + \sum_{i,j,k=1}^{2} p_{i\mu}p_{j\nu}p_{k\rho}C_{ijk},
\end{aligned}
\tag{3.10}
$$

$$
\begin{aligned}
D_\mu &= \sum_{i=1}^{3} p_{i\mu} D_i, \\
D_{\mu\nu} &= g_{\mu\nu} D_{00} + \sum_{i,j=1}^{3} p_{i\mu} p_{j\nu} D_{ij}, \\
D_{\mu\nu\rho} &= \sum_{i=1}^{3} (g_{\mu\nu} p_{i\rho} + g_{\nu\rho} p_{i\mu} + g_{\mu\rho} p_{i\nu}) D_{00i} + \sum_{i,j,k=1}^{3} p_{i\mu} p_{j\nu} p_{k\rho} D_{ijk}, \\
D_{\mu\nu\rho\sigma} &= (g_{\mu\nu} g_{\rho\sigma} + g_{\mu\rho} g_{\nu\sigma} + g_{\mu\sigma} g_{\nu\rho}) D_{0000} \\
&\quad + \sum_{i,j=1}^{3} (g_{\mu\nu} p_{i\rho} p_{j\sigma} + g_{\nu\rho} p_{i\mu} p_{j\sigma} + g_{\mu\rho} p_{i\nu} p_{j\sigma} \\
&\qquad + g_{\mu\sigma} p_{i\nu} p_{j\rho} + g_{\nu\sigma} p_{i\mu} p_{j\rho} + g_{\rho\sigma} p_{i\mu} p_{j\nu}) D_{00ij} \\
&\quad + \sum_{i,j,k,l=1}^{3} p_{i\mu} p_{j\nu} p_{k\rho} p_{l\sigma} D_{ijkl}.
\end{aligned}
\tag{3.11}
$$

To concisely write the terms that contain $g_{\mu\nu}$, we introduce an artificial momentum p_0. The tensor integrals now reads

$$
T^N_{\mu_1 \ldots \mu_r}(p_1, \ldots, p_{N-1}, m_0, \ldots, m_{N-1}) = \sum_{i_1, \ldots, i_r = 0}^{N-1} T^N_{i_1 \ldots i_r} p_{i_1 \mu_1} \cdots p_{i_r \mu_r}. \tag{3.12}
$$

We can rewrite terms that involve $g_{\mu\nu}$ and products of even numbers of p_0's by the corresponding totally symmetric tensor structures of $g_{\mu\nu}$, e.g.

$$\begin{aligned} &\text{Odd numbers of } p_0 \quad \rightarrow \quad 0, \\ &p_{0\mu_1} p_{0\mu_2} \quad \rightarrow \quad g_{\mu_1\mu_2}, \\ &p_{0\mu_1} p_{0\mu_2} p_{0\mu_3} p_{0\mu_4} \quad \rightarrow \quad g_{\mu_1\mu_2} g_{\mu_3\mu_4} + g_{\mu_1\mu_3} g_{\mu_2\mu_4} + g_{\mu_1\mu_4} g_{\mu_2\mu_3}, \end{aligned} \tag{3.13}$$

and removing all terms with products of odd number of p_0's. In four dimensional space, the terms involving $g_{\mu\nu}$ can be omitted for $N > 4$, and we can use at most four Lorentz vectors in the decomposition Equation 3.12 since four Lorentz vectors can span the four dimensional space. For N larger or equal to five in four dimensions, the Lorentz decomposition of tensor integrals reads

$$T^N_{\mu_1\ldots\mu_r}(p_1,\ldots,p_{N-1},m_0,\ldots,m_{N-1}) = \sum_{i_1,\ldots,i_r=1}^{4} T^N_{i_1\ldots i_r} p_{i_1\mu_1}\cdots p_{i_r\mu_r}, \tag{3.14}$$

where $p_{i_1},\ldots,p_{i_p}$ is composed of any four linearly independent vectors out of $p_1,\ldots,p_{N-1}$. It can be easily seen that exchanging of the propagators will not change the result of the integrals. Consequently, the scalar coefficient functions is invariant under exchange the arguments $(p_i,m_i) \leftrightarrow (p_j,m_j)$ with corresponding indices switch $i \leftrightarrow j$, and we have the following relations

$$
\begin{aligned}
&T^N_{\ldots\underbrace{i\ldots i}_{n}\ldots\underbrace{j\ldots j}_{m}\ldots}(p_1,\ldots,p_i,\ldots,p_j,\ldots,p_{N-1},m_0,\ldots,m_i,\ldots,m_j,\ldots,m_{N-1}) \\
&= T^N_{\ldots\underbrace{i\ldots i}_{m}\ldots\underbrace{j\ldots j}_{n}\ldots}(p_1,\ldots,p_j,\ldots,p_i,\ldots,p_{N-1},m_0,\ldots,m_j,\ldots,m_i,\ldots,m_{N-1}),
\end{aligned}
\tag{3.15}
$$

e.g.

$$
\begin{aligned}
C_1(p_1,p_2,m_0,m_1,m_2) &= C_2(p_2,p_1,m_0,m_2,m_1), \\
C_{00}(p_1,p_2,m_0,m_1,m_2) &= C_{00}(p_2,p_1,m_0,m_2,m_1), \\
C_{12}(p_1,p_2,m_0,m_1,m_2) &= C_{12}(p_2,p_1,m_0,m_2,m_1).
\end{aligned}
\tag{3.16}
$$

3.2 Tensor integral reductions

It has been shown that we can iteratively reduce the invariant functions $T^N_{i_1\ldots i_r}$ to the scalar integrals T^N_0 by using Equation 3.12 [77, 78] . The product of an external momentum with the integration momentum q_μ can be rewritten as a combination of the denominators

$$
q\cdot p_k = \frac{1}{2}[(q+p_k)^2 - q^2 - p_k^2] = \frac{1}{2}[D_k - D_0 - f_k], \tag{3.17}
$$

where

$$
f_k = p_k^2 - m_k^2 + m_0^2. \tag{3.18}
$$

Multiplying Equation 3.7 with p_k and substituting Equation 3.17 yields

$$\begin{aligned} R^{N,k}_{\mu_1\ldots\mu_{r-1}} &= T^N_{\mu_1\ldots\mu_r} p_k^{\mu_r} \\ &= \frac{1}{2}\frac{(2\pi\mu)^{4-D}}{i\pi^2}\int d^Dq \left[\frac{q_{\mu_1}\cdots q_{\mu_{r-1}}}{D_0\ldots D_{k-1}D_{k+1}\ldots D_{N-1}}\right. \\ &\qquad \left. -\frac{q_{\mu_1}\cdots q_{\mu_{r-1}}}{D_1\ldots D_{N-1}} - f_k\frac{q_{\mu_1}\cdots q_{\mu_{r-1}}}{D_0\ldots D_{N-1}}\right] \\ &= \tfrac{1}{2}\left[T^{N-1}_{\mu_1\ldots\mu_{r-1}}(k) - T^{N-1}_{\mu_1\ldots\mu_{r-1}}(0) - f_k T^N_{\mu_1\ldots\mu_{r-1}}\right], \end{aligned} \tag{3.19}$$

where k indicates that D_k was cancelled. To bring $T^{N-1}_{\mu_1\ldots\mu_{r-1}}(0)$ to the form Equation 3.7, a shift of the integration momentum ($q \to q - p_1$) is required in $T^{N-1}_{\mu_1\ldots\mu_{r-1}}(0)$, the first propagator of which has an external momentum. As a result, the number of Lorentz index for tensor integrals on the RHS of Equation 3.19 is less than the original tensor integral by one. For $r \geq 2$, we have an extra relation by contracting Equation 3.7 with $g^{\mu\nu}$ and using

$$g^{\mu\nu}q_\mu q_\nu = q^2 = D_0 + m_0^2. \tag{3.20}$$

This gives

$$\begin{aligned} R^{N,00}_{\mu_1\ldots\mu_{r-2}} &= T^N_{\mu_1\ldots\mu_r} g^{\mu_{r-1}\mu_r} \\ &= \frac{(2\pi\mu)^{4-D}}{i\pi^2}\int d^Dq \left[\frac{q_{\mu_1}\cdots q_{\mu_{r-2}}}{D_1\ldots D_N} + m_0^2\frac{q_{\mu_1}\cdots q_{\mu_{r-2}}}{D_0\ldots D_N}\right] \\ &= \left[T^{N-1}_{\mu_1\ldots\mu_{r-2}}(0) + m_0^2 T^N_{\mu_1\ldots\mu_{r-2}}\right]. \end{aligned} \tag{3.21}$$

For the coefficient functions, we can obtain a set of linear equations by using the Lorentz decomposition Equation 3.12 with Equation 3.19 and Equation 3.21.

For each tensor integral, we can decompose this set into several independent sets of $N-1$ equations. Combining with Equation 3.12, the Lorentz decomposition of T_N, $R^{N,00}$, and $R^{N,k}$ reads

$$\begin{aligned} R^{N,k}_{\mu_1\ldots\mu_{r-1}} &= T^N_{\mu_1\ldots\mu_r} p_k^{\mu_r} &&= \sum_{i_1,\ldots,i_{r-1}=0}^{M} R^{N,k}_{i_1\ldots i_{r-1}} p_{i_1\mu_1}\cdots p_{i_{r-1}\mu_{r-1}}, \\ R^{N,00}_{\mu_1\ldots\mu_{r-2}} &= T^N_{\mu_1\ldots\mu_r} g^{\mu_{r-1}\mu_r} &&= \sum_{i_1,\ldots,i_{r-2}=0}^{M} R^{N,00}_{i_1\ldots i_{r-2}} p_{i_1\mu_1}\cdots p_{i_{r-2}\mu_{r-2}}. \end{aligned} \tag{3.22}$$

Inserting these decomposition into the first lines of Equation 3.19 and Equation 3.21 $T^N_{i_1\ldots i_r}$ becomes

$$\begin{aligned} T^N_{00 i_1\ldots i_{r-2}} &= \frac{1}{D+r-2-M}\left[R^{N,00}_{i_1\ldots i_{r-2}} - \sum_{k=1}^{M} R^{N,k}_{k i_1\ldots i_{r-2}}\right], \\ T^N_{k i_1\ldots i_{r-1}} &= \left(X^{-1}_{N-1}\right)_{kk'}\left[R^{N,k'}_{i_1\ldots i_{r-1}} - \sum_{r=1}^{r-1}\delta^{k'}_{i_r} T^N_{00 i_1\ldots i_{r-1} i_{r+1}\ldots i_{r-1}}\right]. \end{aligned} \tag{3.23}$$

We stress tha the factor, $F + r - 2 - M$, is always positive while $r \geq 2$ and $D > M$. Here

$$X_{N-1} = \begin{pmatrix} p_1^2 & p_1 p_2 & \cdots & p_1 p_{N-1} \\ p_2 p_1 & p_2^2 & \cdots & p_2 p_{N-1} \\ \vdots & \vdots & \ddots & \vdots \\ p_{N-1} p_1 & p_{N-1} p_2 & \cdots & p_{N-1}^2 . \end{pmatrix} \tag{3.24}$$

If the matrix X_{N-1}^{-1} is invertible, the Lorentz indices of the invariant functions $T^N_{i_1 \ldots i_r}$ can be reduced(See Equation 3.23 and Equation 3.25). By making this reduction iteratively, all tensor integrals can be expressed as a combination of scalar integrals T_0^L with $L \leq N$. However, the reduction algorithm breaks down provided the matrix X_{N-1} becomes singular (i.e., the determinant equal to zero). The collinearity of p_i usually occurs at the edge of the phase space, and this leads to the singularity. On the other hand, the singularity caused by the linear dependence of the momenta can be removed by excluding the vectors of the set $p_1, \ldots, p_{N-1}$ that is linear dependent in the Lorentz decomposition, and we can build a reduced matrix, X_M, where $M < N - 1$. The reduction works again if X_M is nonsingular.

In Section 3.4, we will discuss a different reduction algorithm [80, 88] required if the determinant of X_{N-1} vanishes while all momentum are linear independent.

Using the third lines of Equation 3.19 and Equation 3.21 , we can express the R's in terms of $T^N_{i_1\ldots i_{r-1}}$, $T^N_{i_1\ldots i_{r-2}}$, and $T^{N-1}_{i_1\ldots i_q}$, with $q < r$ as follows

$$
\begin{aligned}
R^{N,00}_{i_1\ldots i_q\underbrace{M\ldots M}_{r-2-q}} &= m_0^2 T^N_{i_1\ldots i_q\underbrace{M\ldots M}_{r-2-q}} \\
&\quad + (-1)^{P-q}\left[\tilde{T}^{N-1}_{i_1\ldots i_q}(0) + \binom{r-2-q}{1}\sum_{k_1=1}^{M-1}\tilde{T}^{N-1}_{i_1\ldots i_q k_1}(0)\right. \\
&\qquad + \binom{r-2-q}{2}\sum_{k_1,k_2=1}^{M-1}\tilde{T}^{N-1}_{i_1\ldots i_q k_1 k_2}(0) + \ldots \\
&\qquad \left. + \binom{r-2-q}{r-2-q}\sum_{k_1,\ldots,k_{r-2-q}=1}^{M-1}\tilde{T}^{N-1}_{i_1\ldots i_q k_1\ldots k_{r-2-q}}(0)\right], \\
R^{N,k}_{i_1\ldots i_q\underbrace{M\ldots M}_{r-1-q}} &= \frac{1}{2}\left\{T^{N-1}_{\tilde{i}_1\ldots\tilde{i}_q\underbrace{\tilde{M}\ldots\tilde{M}}_{r-1-q}}(k)\theta(k \mid i_1,\ldots,i_q,\underbrace{M,\ldots,M}_{r-1-q}) - f_k T^N_{i_1\ldots i_q\underbrace{M\ldots M}_{r-1-q}}\right. \qquad (3.25) \\
&\quad -(-1)^{r-1-q}\left[\tilde{T}^{N-1}_{i_1\ldots i_q}(0) + \binom{r-1-q}{1}\sum_{k_1=1}^{M-1}\tilde{T}^{N-1}_{i_1\ldots i_q k_1}(0)\right. \\
&\qquad + \binom{r-1-q}{2}\sum_{k_1,k_2=1}^{M-1}\tilde{T}^{N-1}_{i_1\ldots i_q k_1 k_2}(0) + \ldots \\
&\qquad \left.\left. + \binom{r-1-q}{r-1-q}\sum_{k_1,\ldots,k_{r-1-q}=1}^{M-1}\tilde{T}^{N-1}_{i_1\ldots i_q k_1\ldots k_{r-1-q}}(0)\right]\right\}
\end{aligned}
$$

where $i_1, \ldots, i_q \neq M$ and

$$\theta(k \mid i_1, \ldots, i_{r-1}) = \begin{cases} 1 & i_r \neq k, \quad r = 1, \ldots, r-1, \\ 0 & \text{else.} \end{cases} \tag{3.26}$$

The tilde in $\tilde{T}$ denotes that the integration variable has been shifted as $q \to q - p_M$ to retain the standard form of the integrals. The shifted terms, which also makes M asymmetric in index in the above equations, are gathered together in the square brackets of Equation 3.25. Different shifts can also cause a similar result. The i-th momentum of the corresponding T^N are denoted by $\tilde{i}$. Note that if $i > k$, T^N equals to the $(i-1)$-th momentum of $T^{N-1}(k)$, where the argument, k, indicates the cancelled propagators.

The coefficients $T_{i_1 \ldots i_r}$ are determined by the above recursion formulae regardless of their symmetries. Therefore, we can use different ways to obtain coefficients whose indices are not equal, allowing for validation of the analytical results and numerical stability.

If the dimension of space-time equals the number of linear independent momenta, $D = M$, then the terms in the Lorentz decomposition that contain $g_{\mu\nu}$ need to be removed, since $g_{\mu\nu}$ can be written in terms of the D momenta. Thus we can obtain coefficients $T^N_{i_1 \ldots i_r}$ from the second equations of Equation 3.23 and Equation 3.25 with $T^N_{00 i_1 \ldots i_{r-2}} = 0$ in this case.

3.3 Scalar one-loop integrals

As discussed in the last section, the one-loop integrals are combinations of the scalar integrals, T^N_0 provided the determinants of matrices X_M are nonvanishing. For A_0, B_0, C_0 and D_0,

general analytical results were derived in [79], and the numerical calculation algorithms based on the analytical results have been developed in [89]. All rresults for A_0, B_0, C_0 and D_0 are listed in this section.

3.3.1 Scalar one-loop one-point integral

The one-point integral is given by

$$A_0(m) = -m^2(\frac{m^2}{4\pi\mu^2})^{\frac{D-4}{2}}\Gamma(1-\frac{D}{2}) = m^2(\Delta - \log\frac{m^2}{\mu^2} + 1) + \mathcal{O}(D-4), \tag{3.27}$$

where γ_E is Euler's constant, and the UV-divergence is included in

$$\Delta = \frac{2}{4-D} - \gamma_E + \log 4\pi. \tag{3.28}$$

The $\mathcal{O}(D-4)$ terms are only applicable for the calculations with order two or higher.

3.3.2 Scalar one-loop two-point integral

The two-point integral reads

$$\begin{aligned} B_0(p_{10}, m_0, m_1) &= \Delta - \int_0^1 dx \log\frac{[p_{10}^2x^2 - x(p_{10}^2 - m_0^2 + m_1^2) + m_1^2 - i\varepsilon]}{\mu^2} + \mathcal{O}(D-4) \\ &= \Delta + 2 - \log\frac{m_0m_1}{\mu^2} + \frac{m_0^2 - m_1^2}{p_{10}^2}\log\frac{m_1}{m_0} - \frac{m_0m_1}{p_{10}^2}(\frac{1}{r} - r)\log r \\ &\quad + \mathcal{O}(D-4), \end{aligned} \tag{3.29}$$

where r and $\frac{1}{r}$ are determined from

$$x^2 + \frac{m_0^2 + m_1^2 - p_{10}^2 - i\varepsilon}{m_0 m_1}\, x + 1 = (x + r)(x + \frac{1}{r}). \tag{3.30}$$

The derivative of B_0 with respect to p_{10}^2, which can be obtained by differentiating Equation 3.29, is required for the field renormalization constants.

$$\begin{aligned} \frac{\partial}{\partial p_{10}^2} B_0(p_{10}, m_0, m_1) &= -\frac{m_0^2 - m_1^2}{p_{10}^4} \log\frac{m_1}{m_0} + \frac{m_0 m_1}{p_{10}^4}(\frac{1}{r} - r)\log r \\ &\quad -\frac{1}{p_{10}^2}\Big(1 + \frac{r^2+1}{r^2-1}\log r\Big) + \mathcal{O}(D-4). \end{aligned} \tag{3.31}$$

3.3.3 Scalar one-loop three-point integral

The scalar three-point integral calculated by [79] is valid for physical masses and momenta. It has the following symmetric form

$$\begin{aligned} &C_0(p_{10}, p_{20}, m_0, m_1, m_2) = \\ &\quad -\int_0^1 dx \int_0^x dy [p_{21}^2 x^2 + p_{10}^2 y^2 + (p_{20}^2 - p_{10}^2 - p_{21}^2)xy \\ &\qquad + (m_1^2 - m_2^2 - p_{21}^2)x + (m_0^2 - m_1^2 + p_{21}^2 - p_{20}^2)y + m_2^2 - i\varepsilon]^{-1} \qquad (3.32) \\ &= \frac{1}{\alpha}\sum_{i=0}^{2}\Bigg\{\sum_{\sigma=\pm}\Bigg[\mathrm{Li}_2\Big(\frac{y_{0i}-1}{y_{i\sigma}}\Big) - \mathrm{Li}_2\Big(\frac{y_{0i}}{y_{i\sigma}}\Big) \\ &\qquad +\eta\Big(1 - x_{i\sigma}, \frac{1}{y_{i\sigma}}\Big)\log\frac{y_{0i}-1}{y_{i\sigma}} - \eta\Big(-x_{i\sigma}, \frac{1}{y_{i\sigma}}\Big)\log\frac{y_{0i}}{y_{i\sigma}}\Bigg] \\ &\quad -\Big[\eta(-x_{i+}, -x_{i-}) - \eta(y_{i+}, y_{i-}) - 2\pi i\theta(-p_{jk}^2)\theta\big(-\mathrm{Im}(y_{i+}y_{i-})\big)\Big]\log\frac{1-y_{i0}}{-y_{i0}}\Bigg\}, \end{aligned}$$

with cyclic $i, j, k = 0, 1, 2$, and

$$\begin{aligned}
y_{0i} &= \frac{1}{2\alpha p_{jk}^2}\big[p_{jk}^2(p_{jk}^2 - p_{ki}^2 - p_{ij}^2 + 2m_i^2 - m_j^2 - m_k^2) \\
&\quad -(p_{ki}^2 - p_{ij}^2)(m_j^2 - m_k^2) + \alpha(p_{jk}^2 - m_j^2 + m_k^2)\big], \\
x_{i\pm} &= \frac{1}{2p_{jk}^2}\big[p_{jk}^2 - m_j^2 + m_k^2 \pm \alpha_i\big], \\
y_{i\pm} &= y_{0i} - x_{i\pm}, \\
\alpha &= \sqrt{\lambda(p_{10}^2, p_{21}^2, p_{20}^2)}, \\
\alpha_i &= \sqrt{\lambda(p_{jk}^2, m_j^2, m_k^2)}\,(1 + i\varepsilon p_{jk}^2), \text{‘}
\end{aligned} \tag{3.33}$$

and

$$\lambda(x, y, z) = x^2 + y^2 + z^2 - 2(xy + yz + zx). \tag{3.34}$$

The definition of the dilogarithm function $\mathrm{Li}_2(x)$, also called Spence function, is

$$\mathrm{Li}_2(x) = -\int_0^1 \frac{dt}{t}\log(1 - xt), \qquad |\arg(1 - x)| < \pi. \tag{3.35}$$

The cut crossings on the Riemann surface of the logarithms and dilogarithms are compensated by η function defined by

$$\log(ab) = \log(a) + \log(b) + \eta(a, b). \tag{3.36}$$

Notice that η functions in (Equation 3.32) vanish if the masses m_i and α are all real, which occurs for all on-shell scattering and decay processes.

3.3.4 Scalar one-loop four-point integral

Compared to 24 dilogarithms solusions for D_0 given in [79], a new formula involving only 16 dilogarithms given in [81] will be presented in what follows. Here are some useful functions and variables needed to be introduced first. We define

$$k_{ij} = \frac{m_i^2 + m_j^2 - p_{ij}^2}{m_i m_j}, \quad i,j = 0,1,2,3, \tag{3.37}$$

and $\tilde{r}_{ij}$ and r_{ij} by

$$x^2 + (k_{ij} - i\varepsilon)x + 1 = (x + \tilde{r}_{ij})(x + 1/\tilde{r}_{ij}). \tag{3.38}$$

and

$$x^2 + k_{ij}x + 1 = (x + r_{ij})(x + 1/r_{ij}), \tag{3.39}$$

The r_{ij}'s locate either on the complex unit circle or on the real axis for real k_{ij}. Moreover,

$$P(y_0,y_1,y_2,y_3) = \sum_{0\le i<j\le 3} k_{ij}y_iy_j + \sum_{j=0}^{3} y_j^2, \tag{3.40}$$

$$Q(y_0,y_1,0,y_3) = (1/r_{02} - r_{02})y_0 + (k_{12} - r_{02}k_{01})y_1 + (k_{23} - r_{02}k_{03})y_3, \tag{3.41}$$

$$\overline{Q}(y_0,0,y_2,y_3) = (1/r_{13} - r_{13})y_3 + (k_{12} - r_{13}k_{23})y_2 + (k_{01} - r_{13}k_{03})y_0. \tag{3.42}$$

and $x_{1,2}$ is defined by

$$\begin{aligned}\frac{r_{02}r_{13}}{x}\Big\{&\Big[P(1,\frac{x}{r_{13}},0,0)-i\varepsilon\Big]\Big[P(0,0,\frac{1}{r_{02}},x)-i\varepsilon\Big]\\&-\Big[P(0,\frac{x}{r_{13}},\frac{1}{r_{02}},0)-i\varepsilon\Big]\Big[P(1,0,0,x)-i\varepsilon\Big]\Big\}\end{aligned}\tag{3.43}$$

$$= ax^2+bx+c+i\varepsilon d = a(x-x_1)(x-x_2),$$

where

$$\begin{aligned}a &= k_{23}/r_{13}+r_{02}k_{01}-k_{03}r_{02}/r_{13}-k_{12},\\ b &= (r_{13}-1/r_{13})(r_{02}-1/r_{02})+k_{01}k_{23}-k_{03}k_{12},\\ c &= k_{01}/r_{02}+r_{13}k_{23}-k_{03}r_{13}/r_{02}-k_{12},\\ d &= k_{12}-r_{02}k_{01}-r_{13}k_{23}+r_{02}r_{13}k_{03}.\end{aligned}\tag{3.44}$$

Moreover, we define

$$\gamma_{kl} = sign\,\mathrm{Re}[a(x_k-x_l)],\quad k,l=1,2,\tag{3.45}$$

and

$$\begin{aligned} x_{k0} &= x_k, & s_0 &= \tilde{r}_{03}, \\ x_{k1} &= x_k/r_{13}, & s_1 &= \tilde{r}_{01}, \\ x_{k2} &= x_k r_{02}/r_{13}, & s_2 &= \tilde{r}_{12}, \\ x_{k3} &= x_k r_{02}, & s_3 &= \tilde{r}_{23}. \end{aligned} \tag{3.46}$$

as well as

$$x_{kj}^{(0)} = \lim_{\varepsilon\to 0} x_{kj} \quad \text{as} \quad r_{ij} = \lim_{\varepsilon\to 0} \tilde{r}_{ij}. \tag{3.47}$$

Finally we need

$$\tilde{\eta}(a,\tilde{b}) \;=\; \begin{cases} \eta(a,b) & \text{for } b \text{ not real}, \\ 2\pi i \left[\theta(-\operatorname{Im} a)\theta(-\operatorname{Im}\tilde{b}) - \theta(\operatorname{Im} a)\theta(\operatorname{Im}\tilde{b})\right] & \text{for } b<0, \\ 0 & \text{for } b>0 \end{cases} \tag{3.48}$$

where $b = \lim_{\varepsilon\to 0}\tilde{b}$.

Then for real r_{02}, the result can be written as

$$
\begin{aligned}
D_0(p_{10},p_{20},p_{30},m_0,m_1,m_2,m_3) &= \frac{1}{m_1m_2m_3m_4a(x_1-x_2)} \\
&\Bigg\{\sum_{j=0}^{3}\sum_{k=1}^{2}(-1)^{j+k}\Bigg[\mathrm{Li}_2(1+s_jx_{kj})+\eta(-x_{kj},s_j)\log(1+s_jx_{kj}) \\
&\qquad +\mathrm{Li}_2(1+\frac{x_{kj}}{s_j})+\eta(-x_{kj},\frac{1}{s_j})\log(1+\frac{x_{kj}}{s_j})\Bigg] \\
&+\sum_{k=1}^{2}(-1)^{k+1}\Bigg[\tilde{\eta}(-x_k,\tilde{r}_{02})\Bigg[\log(r_{02}x_k)+\log\Big(Q(\frac{1}{x_k^{(0)}},0,0,1)-i\varepsilon\Big) \\
&\qquad +\log\Big(\frac{\overline{Q}(0,0,1,r_{02}x_k^{(0)})}{d}+i\varepsilon\gamma_{k,3-k}sign(r_{02}\mathrm{Im}\,\tilde{r}_{13})\Big)\Bigg] \\
&\quad +\tilde{\eta}(-x_k,\frac{1}{\tilde{r}_{13}})\Bigg[\log\Big(\frac{x_k}{r_{13}}\Big)+\log\Big(Q(\frac{r_{13}}{x_k^{(0)}},1,0,0)-i\varepsilon\Big) \\
&\qquad +\log\Big(\frac{\overline{Q}(1,0,0,x_k^{(0)})}{d}+i\varepsilon\gamma_{k,3-k}sign(\mathrm{Im}\,\tilde{r}_{13})\Big)\Bigg] \\
&\quad -\Big[\tilde{\eta}(-x_k,\frac{\tilde{r}_{02}}{\tilde{r}_{13}})+\eta(\tilde{r}_{02},\frac{1}{\tilde{r}_{13}})\Big]\Bigg[\log\Big(\frac{r_{02}x_k}{r_{13}}\Big)+\log\Big(Q(\frac{r_{13}}{x_k^{(0)}},1,0,0)-i\varepsilon\Big) \\
&\qquad +\log\Big(\frac{\overline{Q}(0,0,1,r_{02}x_k^{(0)})}{d}+i\varepsilon\gamma_{k,3-k}sign(r_{02}\mathrm{Im}\,\tilde{r}_{13})\Big)\Bigg] \\
&\quad +\eta(\tilde{r}_{02},\frac{1}{\tilde{r}_{13}})\tilde{\eta}(-x_k,-\frac{\tilde{r}_{02}}{\tilde{r}_{13}})\Bigg]\Bigg\}\,. \qquad (3.49)
\end{aligned}
$$

In the case that $|r_{ij}|=1$ for all r_{ij}, the result reads:

$$D_0(p_{10},p_{20},p_{30},m_0,m_1,m_2,m_3)=\frac{1}{m_1m_2m_3m_4a(x_1-x_2)}$$
$$\Bigg\{\sum_{j=0}^{3}\sum_{k=1}^{2}(-1)^{j+k}\Big[\mathrm{Li}_2(1+s_jx_{kj})+\eta(-x_{kj},s_j)\log(1+s_jx_{kj})$$
$$+\mathrm{Li}_2(1+\frac{x_{kj}}{s_j})+\eta(-x_{kj},\frac{1}{s_j})\log(1+\frac{x_{kj}}{s_j})\Big]$$
$$+\sum_{k=1}^{2}(-1)^{k+1}\Bigg[\eta(-x_k,\frac{1}{r_{13}})\Bigg[\log\Big(\frac{r_{13}}{x_k^{(0)}}P(1,\frac{x_k^{(0)}}{r_{13}},0,0)-\frac{x_k^{(0)}}{r_{13}}\varepsilon b\gamma_{k,3-k}\Big)+\log\Big(\frac{x_k^{(0)}}{r_{13}}\Big)\Bigg]$$
$$+\eta(-x_k,r_{02})\left[\log\Big(\frac{1}{r_{02}x_k^{(0)}}P(0,0,1,r_{02}x_k^{(0)})-r_{02}x_k^{(0)}\varepsilon b\gamma_{k,3-k}\Big)+\log(r_{02}x_k^{(0)})\right]$$
$$-\left[\eta(-x_k,\frac{r_{02}}{r_{13}})+\eta(r_{02},\frac{1}{r_{13}})\right]\left[\log\Big(\frac{r_{13}}{r_{02}x_k^{(0)}}P(0,1,\frac{r_{02}x_k^{(0)}}{r_{13}},0)-\frac{r_{02}x_k^{(0)}}{r_{13}}\varepsilon b\gamma_{k,3-k}\Big)\right.$$
$$\left.+\log\Big(\frac{r_{02}x_k^{(0)}}{r_{13}}\Big)\right]+\Big(1-\gamma_{k,3-k}sign(b)\Big)\eta(-x_k,-\frac{r_{02}}{r_{13}})\eta(r_{02},\frac{1}{r_{13}})\Bigg]\Bigg\},$$

where ε is infinetesimal.

3.4 Tensor integrals reduction for zero Gram determinant

The scalar five-point integral can be written in terms of five scalar four-point integrals [80, 89] in the four-dimensional spacetime. Moreover, when the Gram determinant of the external momenta of T^N is zero, we can still express tensor integral, T^N, in terms of N integrals T^{N-1}

$$|X_{N-1}|=\begin{vmatrix} p_1^2 & p_1p_2 & \cdots & p_1p_{N-1}\\ p_2p_1 & p_2^2 & \cdots & p_2p_{N-1}\\ \vdots & \vdots & \ddots & \vdots\\ p_{N-1}p_1 & p_{N-1}p_2 & \cdots & p_{N-1}^2 \end{vmatrix}=0, \tag{3.50}$$

The Gram determinant is always zero for $N \geq 6$, since any five momenta must be linearly dependent in the four-dimensional spacetime.

3.4.1 The tensor five-point integral reductions

In this subsection, we show the reduction of tensor five-point integrals while strictly following the notation of [90, 91]. The four and five-point integrals are defined as

$$\begin{aligned} & D\_(p_1, p_2, p_3, m_0, m_1, m_2, m_3) \\ & \quad = \frac{(2\mu\pi)^{(4-D)}}{\mathrm{i}\pi^2} \int \mathrm{d}^D q \, \frac{\text{product of q's}}{D_0 D_1 D_2 D_3}, \\ & E\_(p_1, \cdots, p_4, m_0, m_1, \cdots, m_4) \\ & \quad = \frac{1}{\mathrm{i}\pi^2} \int \mathrm{d}^4 q \, \frac{\text{product of q's}}{D_0 D_1 D_2 D_3 D_4}. \end{aligned} \tag{3.51}$$

Here the underscore denotes all possible Lorentz indices $(0, \mu, \mu\nu, \mu\nu\rho, \mu\nu\rho\sigma, \mu\nu\rho\sigma\tau$ etc...) with the corresponding product of q's $(1, q_\mu, q_\mu q_\nu, q_\mu q_\nu q_\rho, q_\mu q_\nu q_\rho q_\sigma, q_\mu q_\nu q_\rho q_\sigma q_\tau$ etc..), and the denominator factors. In four dimensions, $D = 4$, all above tensor integrals apart from $D_{\mu\nu\rho\sigma}$ and $D_{\mu\nu\rho\sigma\tau}$ are finite.

We can reduce five-point functions to four-point functions as following equations due to the fact that q can be spanned by p_i [80] in four dimensions.

$$0 = \begin{vmatrix} 2q^2 & 2qp_1 & \dots & 2qp_4 \\ 2p_1q & 2p_1p_1 & \dots & 2p_1p_4 \\ \vdots & \vdots & \ddots & \vdots \\ 2p_4q & 2p_4p_1 & \dots & 2p_4p_4 \end{vmatrix} = \begin{vmatrix} 2D_0 + Y_{00} & 2qp_1 & \dots & 2qp_4 \\ D_1 - D_0 + Y_{10} - Y_{00} & 2p_1p_1 & \dots & 2p_1p_4 \\ \vdots & \vdots & \ddots & \vdots \\ D_4 - D_0 + Y_{40} - Y_{00} & 2p_4p_1 & \dots & 2p_4p_4 \end{vmatrix} \tag{3.52}$$

with

$$Y_{ij} = m_i^2 + m_j^2 - (p_i - p_j)^2, \qquad i, j = 0, \dots, 4. \tag{3.53}$$

Equation 3.52 implies

$$0 = \frac{1}{\mathrm{i}\pi^2} \int \mathrm{d}^4 q \, \frac{q_{\mu_1} \cdots q_{\mu_r}}{D_0 D_1 \cdots D_4} \frac{-\Lambda^2}{q^2 - \Lambda^2} \begin{vmatrix} 2D_0 + Y_{00} & 2qp_1 & \dots & 2qp_4 \\ D_1 - D_0 + Y_{10} - Y_{00} & 2p_1p_1 & \dots & 2p_1p_4 \\ \vdots & \vdots & \ddots & \vdots \\ D_4 - D_0 + Y_{40} - Y_{00} & 2p_4p_1 & \dots & 2p_4p_4 \end{vmatrix}, \tag{3.54}$$

where r is the number of integration momenta in the numerator. By expanding the determinant, ultraviolet divergences that happen in intermediate steps are regularized with $\Lambda \to \infty$, which utilize the four-dimensionality of space-time. For all considered five-point integrals, $r \leq 4$, this approach is valid. The Laplace expansion along the first column gives

$$
\begin{aligned}
0 \;=\; & \Big[2D^{(\Lambda)}_{\mu_1\ldots\mu_r}(0) + Y_{00}E^{(\Lambda)}_{\mu_1\ldots\mu_r}\Big]
\begin{vmatrix}
2p_1p_1 & \ldots & 2p_1p_4 \\
\vdots & \ddots & \vdots \\
2p_4p_1 & \ldots & 2p_4p_4
\end{vmatrix} \\
& + \sum_{i=1}^{4}(-1)^i\Big\{D^{(\Lambda)}_{\alpha\mu_1\ldots\mu_r}(i) - D^{(\Lambda)}_{\alpha\mu_1\ldots\mu_r}(0) + (Y_{i0}-Y_{00})E^{(\Lambda)}_{\alpha\mu_1\ldots\mu_r}\Big\} \\
& \times
\begin{vmatrix}
2p_1^\alpha & \ldots & 2p_4^\alpha \\
2p_1p_1 & \ldots & 2p_1p_4 \\
\vdots & \ddots & \vdots \\
2p_{i-1}p_1 & \ldots & 2p_{i-1}p_4 \\
2p_{i+1}p_1 & \ldots & 2p_{i+1}p_4 \\
\vdots & \ddots & \vdots \\
2p_4p_1 & \ldots & 2p_4p_4
\end{vmatrix},
\end{aligned}
\tag{3.55}
$$

where $D^{(\Lambda)}_{\mu_1\ldots\mu_r}(i)$ is the four-point integral that comes from $E^{(\Lambda)}_{\mu_1\ldots\mu_r}$ by omitting the ith propagator N_i^{-1}. The superscript (Λ) indicates the regularization as introduced in (Equation 3.54). For all E integrals, we can omit omit the superscript (Λ) directly by taking the limit $\Lambda \to \infty$

since all five-point functions appeared are UV finite due to the fact that rank ≤ 5. Similarly, the UV-divergent four-point functions can be split as follows,

$$\lim_{x\to\infty} D^{(\Lambda)}_{\mu_1\ldots\mu_r} = D^{(\text{fin})}_{\mu_1\ldots\mu_r} + \Delta_{\mu_1\ldots\mu_r}, \tag{3.56}$$

where $D^{(\text{fin})}_{\mu_1\ldots\mu_r}$ denotes the UV-finite part in D dimensions defined in (Equation 3.51). As in the $\overline{\text{MS}}$ scheme, the UV divergence is subtracted from $D_{\mu_1\ldots\mu_r}$.

By plugging (Equation 3.56) into (Equation 3.55) and taking Λ asymptotically large, we have

$$
\begin{aligned}
0 \;=\; & \Big[2D^{(\mathrm{fin})}_{\mu_1\ldots\mu_r}(0) + 2\Delta_{\mu_1\ldots\mu_r}(0) + Y_{00}E_{\mu_1\ldots\mu_r}\Big]
\begin{vmatrix} 2p_1p_1 & \ldots & 2p_1p_4 \\ \vdots & \ddots & \vdots \\ 2p_4p_1 & \ldots & 2p_4p_4 \end{vmatrix} \\
& + \sum_{i=1}^{4}(-1)^i\Big\{D^{(\mathrm{fin})}_{\alpha\mu_1\ldots\mu_r}(i) - \Big[D^{(\mathrm{fin})}_{\alpha\mu_1\ldots\mu_r}(0) + p_{1\alpha}D^{(\mathrm{fin})}_{\mu_1\ldots\mu_r}(0)\Big] + p_{1\alpha}D^{(\mathrm{fin})}_{\mu_1\ldots\mu_r}(0) \\
& + \Delta_{\alpha\mu_1\ldots\mu_r}(i) - \Delta_{\alpha\mu_1\ldots\mu_r}(0) + (Y_{i0} - Y_{00})E_{\alpha\mu_1\ldots\mu_r}\Big\}
\begin{vmatrix} 2p_1^\alpha & \ldots & 2p_4^\alpha \\ 2p_1p_1 & \ldots & 2p_1p_4 \\ \vdots & \ddots & \vdots \\ 2p_{i-1}p_1 & \ldots & 2p_{i-1}p_4 \\ 2p_{i+1}p_1 & \ldots & 2p_{i+1}p_4 \\ \vdots & \ddots & \vdots \\ 2p_4p_1 & \ldots & 2p_4p_4 \end{vmatrix}
\end{aligned} \tag{3.57}
$$

Notice that we can simplify the contributions to four-point functions involving $p_{j\alpha}$ as follows. The extra terms involving $\Delta_{\mu_1\ldots\mu_r}$ contribute for $r = 4$, but are dropped out in the final result for $r = 3$, and are absent for $r \leq 2$ which does not contain UV-divergent integrals.

The Lorentz-covariant decompositions has the following forms

$$
\begin{aligned}
D^{(\mathrm{fin})}_{\alpha\mu_1\ldots\mu_r}(i) &= [D^{(\mathrm{fin})}_{\alpha\mu_1\ldots\mu_r}(i)]^{(p)} + [D^{(\mathrm{fin})}_{\alpha\mu_1\ldots\mu_r}(i)]^{(g)}, \qquad i = 0,\ldots,4, \\
[D^{(\mathrm{fin})}_{\alpha\mu_1\ldots\mu_r}(i)]^{(p)} &= \sum_{\substack{j=1 \\ j\neq i}}^{4} p_{j\alpha} X_{j,\mu_1\ldots\mu_r}(i), \\
[D^{(\mathrm{fin})}_{\alpha\mu_1\ldots\mu_r}(i)]^{(g)} &= \sum_{j=1}^{r} g_{\alpha\mu_j} Y_{j,\mu_1\ldots\mu_{j-1}\mu_{j+1}\ldots\mu_r}(i), \\
[D^{(\mathrm{fin})}_{\alpha\mu_1\ldots\mu_r}(0) + p_{1\alpha} D^{(\mathrm{fin})}_{\mu_1\ldots\mu_r}(0)]^{(p)} &= \sum_{j=2}^{4} (p_j - p_1)_\alpha Z_{\mu_1\ldots\mu_r}.
\end{aligned}
\tag{3.58}
$$

The superscript "(p)" denotes operation isolating any tensor structure which have its first Lorentz index on a vector momentum. The remaining are the tensor structures with a superscript "(g)" since they have their first Lorentz index on the metric tensor. By performing a shift $q \to q - p_1$ in the integral, we can derive the last decomposition in (Equation 3.58). From (Equation 3.58), we can see that the terms in (Equation 3.57) involving $[D^{(\mathrm{fin})}_{\alpha\mu_1\ldots\mu_r}(i)]^{(p)}$ are removed when multiplied with the vanishing determinants. Similarly, we can drop out the terms proportional to $[D^{(\mathrm{fin})}_{\alpha\mu_1\ldots\mu_r}(0) + p_{1\alpha} D^{(\mathrm{fin})}_{\mu_1\ldots\mu_r}(0)]^{(p)}$ after i aresummed up. After that, the term $p_{1\alpha} D^{(\mathrm{fin})}_{\mu_1\ldots\mu_r}(0)$ remains only when $i = 1$, where we can combine this term with the first term in (Equation 3.57). We can rewrite the equation

$$\left[\frac{(2\pi\mu)^{4-D}}{\mathrm{i}\pi^2}\int \mathrm{d}^D q\,\frac{q_{\mu_1}\cdots q_{\mu_r}}{D_0 D_1\cdots D_4}\,\middle|\begin{array}{cccc} D_0+Y_{00} & 2qp_1 & \dots & 2qp_4 \\ Y_{10}-Y_{00} & 2p_1p_1 & \dots & 2p_1p_4 \\ \vdots & \vdots & \ddots & \vdots \\ Y_{40}-Y_{00} & 2p_4p_1 & \dots & 2p_4p_4 \end{array}\right]^{(\mathrm{fin})} = V_{\mu_1\dots\mu_r}+U_{\mu_1\dots\mu_r}. \tag{3.59}$$

Here we introduced

$$V_{\mu_1\dots\mu_r} = -\begin{vmatrix} 0 & 2p_1^\alpha & \dots & 2p_4^\alpha \\ \mathcal{D}_{\alpha\mu_1\dots\mu_r}(1) & 2p_1p_1 & \dots & 2p_1p_4 \\ \vdots & \vdots & \ddots & \vdots \\ \mathcal{D}_{\alpha\mu_1\dots\mu_r}(4) & 2p_4p_1 & \dots & 2p_4p_4 \end{vmatrix} = \sum_{i,j=1}^{4}(-1)^{i+j}\,\det(\hat{Z}_{ij}^{(4)})\,2p_j^\alpha\mathcal{D}_{\alpha\mu_1\dots\mu_r}(i) \tag{3.60}$$

with

$$\mathcal{D}_{\alpha\mu_1\dots\mu_r}(i) = [D^{(\mathrm{fin})}_{\alpha\mu_1\dots\mu_r}(i) - D^{(\mathrm{fin})}_{\alpha\mu_1\dots\mu_r}(0)]^{(g)}, \qquad i=1,\dots,4 \tag{3.61}$$

All terms containing $[D]^{(g)}$ are collected by Equation 3.61. For the scalar five-point integral reduction, the extra term V is vanished because of the term $D_\alpha = [D_\alpha]^{(p)}$. The four-dimensional Gram matrix gives the three-dimensional matrices, $\hat{Z}_{ij}^{(4)}$ by dropping out both the ith row and jth column.

$$Z^{(4)} = \begin{pmatrix} 2p_1p_1 & \dots & 2p_1p_4 \\ \vdots & \ddots & \vdots \\ 2p_4p_1 & \dots & 2p_4p_4 \end{pmatrix} \tag{3.62}$$

The UV divergences gives the term $U_{\mu_1\dots\mu_r}$, which has the following form

$$U_{\mu_1\dots\mu_r} = -2\Delta_{\mu_1\dots\mu_r}(0)\det(Z^{(4)}) + \sum_{i,j=1}^{4}(-1)^{i+j}\ \det(\hat{Z}^{(4)}_{ij})\,2p_j^{\alpha}[\Delta_{\alpha\mu_1\dots\mu_r}(i) - \Delta_{\alpha\mu_1\dots\mu_r}(0)]. \tag{3.63}$$

The detailed derivation of $U_{\mu_1\dots\mu_r}$ are given in [82] which yield

$$U_{\mu_1\dots\mu_r} = \begin{cases} -\frac{\det(Z^{(4)})}{48}(g_{\mu_1\mu_2}g_{\mu_3\mu_4} + g_{\mu_1\mu_3}g_{\mu_4\mu_2} + g_{\mu_1\mu_4}g_{\mu_2\mu_3}) & \text{for } r = 4, \\ 0 & \text{for } r \leq 3. \end{cases}$$

Terms for $r \geq 5$ are not included here. By using the following relations

$$2qp_j = D_j - D_0 + Y_{0j} - Y_{00}, \qquad 2p_ip_j = Y_{ij} - Y_{i0} - Y_{0j} + Y_{00}, \tag{3.64}$$

, and adding the first column of the determinant in (Equation 3.59) to the remaining columns, we can expand the determinant by one row and one column, and have $V_{\mu_1\ldots\mu_r} + U_{\mu_1\ldots\mu_r}$ equals to

$$\begin{vmatrix} 1 & Y_{00} & \ldots & Y_{04} \\ 0 & D^{(\mathrm{fin})}_{\mu_1\ldots\mu_r}(0) + Y_{00}E_{\mu_1\ldots\mu_r} & \ldots & D^{(\mathrm{fin})}_{\mu_1\ldots\mu_r}(4) + Y_{04}E_{\mu_1\ldots\mu_r} \\ 0 & Y_{10} - Y_{00} & \ldots & Y_{14} - Y_{04} \\ \vdots & \vdots & \ddots & \vdots \\ 0 & Y_{40} - Y_{00} & \ldots & Y_{44} - Y_{04} \end{vmatrix} . \tag{3.65}$$

The determinant in above equation can be rewritten as

$$\begin{vmatrix} E_{\mu_1\ldots\mu_r} & -D^{(\mathrm{fin})}_{\mu_1\ldots\mu_r}(0) & \ldots & -D^{(\mathrm{fin})}_{\mu_1\ldots\mu_r}(4) \\ 1 & Y_{00} & \ldots & Y_{04} \\ 1 & Y_{10} & \ldots & Y_{14} \\ \vdots & \vdots & \ddots & \vdots \\ 1 & Y_{40} & \ldots & Y_{44} \end{vmatrix} . \tag{3.66}$$

Therefore, the tensor five-point function, $E_{\mu_1\ldots\mu_r}$, can be reduced to five tensor four-point functions

$$\begin{aligned} E_{\mu_1\ldots\mu_r} &= -\sum_{i=0}^{4} \frac{\det(Y_i)}{\det(Y)} D^{(\mathrm{fin})}_{\mu_1\ldots\mu_r}(i) + \sum_{i,j=1}^{4} (-1)^{i+j} \frac{\det(\hat{Z}^{(4)}_{ij})}{\det(Y)} 2p_j^{\alpha} \mathcal{D}_{\alpha\mu_1\ldots\mu_r}(i) \\ &\quad + \frac{1}{\det(Y)} U_{\mu_1\ldots\mu_r}. \end{aligned} \tag{3.67}$$

Here Y is a short hand of the 5-dimensional Cayley matrix, Y_{ij}, $i = 0, \ldots 4$. Y_i is obtained by setting $Y_{ij} = 1$ for $j = 0, \ldots 4$.

3.4.2 The coefficients of five-point tensor integrals

The tensor decompositions can be written in a compact way with the notations, introduced in [18],

$$T^{[\mu_1\ldots\mu_r]} = T^{\mu_1\ldots\mu_r} + T^{\mu_2\ldots\mu_r\mu_1} + \ldots + T^{\mu_r\mu_1\ldots\mu_{r-1}}, \tag{3.68}$$

where the square brackets with Lorentz indices within denote the sum of all cyclic permutations of tensors. For instance, $g_{[\mu\nu}g_{\rho]\sigma} = g_{\mu\nu}g_{\rho\sigma} + g_{\nu\rho}g_{\mu\sigma} + g_{\rho\mu}g_{\nu\sigma}$.

We can also use this notation recursively, for example,

$$T^{[\alpha[\beta\gamma]]} = T^{[\alpha\beta\gamma]} + T^{[\alpha\gamma\beta]} \tag{3.69}$$

$$= T^{\alpha\beta\gamma} + T^{\beta\gamma\alpha} + T^{\gamma\alpha\beta} + T^{\alpha\gamma\beta} + T^{\gamma\beta\alpha} + T^{\beta\alpha\gamma}. \tag{3.70}$$

The tensor integrals after canceling the denominator D_0 are not in the standard form, but we can express these tensor integrals as combinations of standard integrals by performing the shift $q \to q - p_1$. Therefore we have the forms for the four-point integrals

$$\begin{aligned} \tilde{D}\_(0) &= \frac{(2\pi\mu)^{(4-D)}}{\mathrm{i}\pi^2} \int \mathrm{d}^D q \, \frac{\text{product of q's}}{\tilde{D}_1 \tilde{D}_2 \tilde{D}_3 \tilde{D}_4}, \\ \tilde{D}_i &= (q + p_i - p_1)^2 - m_i^2 + \mathrm{i}\epsilon, \qquad i = 1, \ldots, 4, \end{aligned} \tag{3.71}$$

where the underscore denotes all possible Lorentz indices $(0, \mu, \mu\nu, \mu\nu\rho, \mu\nu\rho\sigma, \mu\nu\rho\sigma\tau)$ with possible product of q's $(1, q_\mu, q_\mu q_\nu, q_\mu q_\nu q_\rho, q_\mu q_\nu q_\rho q_\sigma, q_\mu q_\nu q_\rho q_\sigma q_\tau)$. The tilde on D_0, D_{00} and D_{0000} can be omitted since these functions are invariant under this shift. The following shorthand for shifted indices are introduced in the decomposition of $D\_(i)$ with $i = 1, \ldots, 4$

$$j_i = \begin{cases} j & \text{for} \quad i > j, \\ j - 1 & \text{for} \quad i < j. \end{cases} \tag{3.72}$$

Eq (Equation 3.67) now reads

$$E_{\mu_1 \ldots \mu_r} = -\sum_{i=0}^{4} \eta_i D^{(\mathrm{fin})}_{\mu_1 \ldots \mu_r}(i) + 2 \sum_{i,j=1}^{4} \zeta_{ij} \, p_j^\alpha \, \mathcal{D}_{\alpha \mu_1 \ldots \mu_r}(i) + \frac{1}{\det(Y)} U_{\mu_1 \ldots \mu_r}, \tag{3.73}$$

where the following shorthand notations are used to simplify the result

$$\bar{\delta}_{ij} = 1 - \delta_{ij} \quad , \tag{3.74}$$

$$\sum_i \bar{\delta}_{ij}(\dots) = \sum_{i \neq j}(\dots) \quad , \tag{3.75}$$

$$\eta_i = \frac{\det(Y_i)}{\det(Y)}, \quad i = 0, \dots, 4, \qquad \zeta_{ij} = (-1)^{i+j} \frac{\det(\hat{Z}_{ij}^{(4)})}{\det(Y)} = \zeta_{ji}, \quad i, j = 1, \dots, 4. \tag{3.76}$$

The covariant decompositions are list as follows

Rank zero tensor integral / Scalar integral

$$E_0 = -\sum_{i=0}^{4} \eta_i D_0(i), \tag{3.77}$$

which is found in Refs. [80, 86, 90, 91].

Rank one tensor integrals / Vector integral

$$
\begin{aligned}
E^\mu &= \sum_{j=1}^{4} p_j^\mu E_j, \\
D^\mu(i) &= \sum_{\substack{j=1 \\ j\neq i}}^{4} p_j^\mu D_{j_i}(i), \qquad i = 1,\ldots,4, \\
D^\mu(0) &= -p_1^\mu D_0(0) + \tilde{D}^\mu(0) = -p_1^\mu D_0(0) + \sum_{j=2}^{4} (p_j - p_1)^\mu \tilde{D}_{j-1}(0), \\
\mathcal{D}^{\alpha\mu}(i) &= g^{\alpha\mu}[-D_{00}(0) + D_{00}(i)].
\end{aligned} \tag{3.78}
$$

We can insert these into (Equation 3.73) for the vector integral to get

$$
E_j = -\sum_{i=1}^{4} \eta_i D_{j_i}(i)\bar{\delta}_{ji} - \eta_0 D_j(0) + 2\sum_{i=1}^{4} \zeta_{ji}[D_{00}(i) - D_{00}(0)], \qquad j = 1,\ldots,4, \tag{3.79}
$$

with

$$
D_1(0) = -D_0(0) - \sum_{j=1}^{3} \tilde{D}_j(0), \tag{3.80}
$$

where $D_j(0) = \tilde{D}_{j-1}(0),\ j = 2,3,4.$

Rank two tensor integrals

$$
\begin{aligned}
E^{\mu\nu} &= \sum_{j,k=1}^{4} p_j^\mu p_k^\nu E_{jk} + g^{\mu\nu} E_{00}, \\
D^{\mu\nu}(i) &= \sum_{\substack{j,k=1 \\ j,k\neq i}}^{4} p_j^\mu p_k^\nu D_{j_i k_i}(i) + g^{\mu\nu} D_{00}(i), \qquad i = 1, \ldots, 4, \\
D^{\mu\nu}(0) &= -p_1^{[\mu} \tilde{D}^{\nu]}(0) + p_1^\mu p_1^\nu D_0(0) + \tilde{D}^{\mu\nu}(0) \\
&= g^{\mu\nu} D_{00}(0) + p_1^\mu p_1^\nu D_0(0) + \sum_{j,k=2}^{4} (p_j - p_1)^\mu (p_k - p_1)^\nu \tilde{D}_{j-1,k-1}(0) \\
&\quad - \sum_{j=2}^{4} p_1^{[\mu} (p_j - p_1)^{\nu]} \tilde{D}_{j-1}(0), \\
\mathcal{D}^{\alpha\mu\nu}(i) &= \left[-D^{\alpha\mu\nu}(0) + D^{\alpha\mu\nu}(i) \right]^{(g)} \\
&= \left[-\tilde{D}^{\alpha\mu\nu}(0) + \tilde{D}^{\alpha[\nu}(0) p_1^{\mu]} + D^{\alpha\mu\nu}(i) \right]^{(g)} \\
&= \sum_{\substack{j=1 \\ j\neq i}}^{4} g^{\alpha[\mu} p_j^{\nu]} D_{00 j_i}(i) - \sum_{j=2}^{4} g^{\alpha[\mu} (p_j - p_1)^{\nu]} \tilde{D}_{00,j-1}(0) + p_1^{[\mu} g^{\nu]\alpha} D_{00}(0). \quad (3.81)
\end{aligned}
$$

Notice that the E_{00} is redundant since we can use four linearly independent vectors, p_k, to express $g^{\mu\nu}$ up to $\mathcal{O}(D-4)$,

$$
g^{\mu\nu} = \sum_{j,k=1}^{4} 2 p_j^\mu p_k^\nu (Z^{(4)})^{-1}_{jk} + \mathcal{O}(D-4). \quad (3.82)
$$

Therefore, we can define the coefficient E_{00} to avoid $\det(Z^{(4)})$.

From Equation 3.73, we have

$$
\begin{aligned}
E_{00} &= -\sum_{i=1}^{4} \eta_i D_{00}(i) - \eta_0 D_{00}(0), \\
E_{jk} &= 2\left\{ \sum_{i=1}^{4} \zeta_{ji}[-D_{00k}(0) + D_{00k_i}(i)\bar{\delta}_{ki}] + (k \leftrightarrow j) \right\} \\
&\quad - \eta_0 D_{jk}(0) - \sum_{i=1}^{4} \eta_i D_{j_i k_i}(i)\bar{\delta}_{ji}\bar{\delta}_{ki}, \qquad j,k = 1,\ldots,4,
\end{aligned} \tag{3.83}
$$

with

$$
\begin{aligned}
D_{jk}(0) &= \tilde{D}_{j-1,k-1}(0), \\
D_{j1}(0) &= -\tilde{D}_{j-1}(0) - \sum_{k=1}^{3} \tilde{D}_{j-1,k}(0), \\
D_{11}(0) &= D_0(0) + \sum_{j,k=1}^{3} \tilde{D}_{jk}(0) + 2\sum_{j=1}^{3} \tilde{D}_j(0), \\
D_{001}(0) &= -D_{00}(0) - \sum_{j=1}^{3} \tilde{D}_{00j}(0), \\
D_{00j}(0) &= \tilde{D}_{00,j-1}(0), \qquad j,k = 2,3,4.
\end{aligned} \tag{3.84}
$$

Rank three tensor integrals

$$
\begin{aligned}
E^{\mu\nu\rho} &= \sum_{j,k,l=1}^{4} p_j^\mu p_k^\nu p_l^\rho E_{jkl} + \sum_{j=1}^{4} g^{[\mu\nu} p_j^{\rho]} E_{00j}, \\
D^{\mu\nu\rho}(i) &= \sum_{\substack{j,k,l=1 \\ j,k,l\neq i}}^{4} p_j^\mu p_k^\nu p_l^\rho D_{j_i k_i l_i}(i) + \sum_{\substack{j=1 \\ j\neq i}}^{4} g^{[\mu\nu} p_j^{\rho]} \tilde{D}_{00j_i}(i), \qquad i = 1,\ldots,4, \\
D^{\mu\nu\rho}(0) &= \tilde{D}^{\mu\nu\rho}(0) - p_1^{[\mu}\tilde{D}^{\nu\rho]}(0) + p_1^{[\mu}p_1^\nu \tilde{D}^{\rho]}(0) - p_1^\mu p_1^\nu p_1^\rho D_0(0) \\
&= -\sum_{j=2}^{4} g^{[\mu\nu}(p_1-p_j)^{\rho]}\tilde{D}_{00,j-1}(0) \\
&\quad - p_1^{[\mu}\sum_{j,k=2}^{4}(p_1-p_j)^\nu(p_1-p_k)^{\rho]}\tilde{D}_{j-1,k-1}(0) - p_1^{[\mu}g^{\nu\rho]}D_{00}(0) \\
&\quad - p_1^{[\mu}p_1^\nu\sum_{j=2}^{4}(p_1-p_j)^{\rho]}\tilde{D}_{j-1}(0) - p_1^\mu p_1^\nu p_1^\rho D_0(0) \\
&\quad - \sum_{j,k,l=2}^{4}(p_1-p_j)^\mu(p_1-p_k)^\nu(p_1-p_l)^\rho\tilde{D}_{j-1,k-1,l-1}(0), \\
\mathcal{D}^{\alpha\mu\nu\rho}(i) &= \left[-D^{\alpha\mu\nu\rho,(\mathrm{fin})}(0) + D^{\alpha\mu\nu\rho,(\mathrm{fin})}(i)\right]^{(g)} \\
&= \left[-\tilde{D}^{\alpha\mu\nu\rho,(\mathrm{fin})}(0) + D^{\alpha\mu\nu\rho,(\mathrm{fin})}(i) + \tilde{D}^{\alpha[\nu\rho}(0)p_1^{\mu]} - \tilde{D}^{\alpha[\rho}(0)p_1^\mu p_1^{\nu]}\right]^{(g)} \\
&= \sum_{\substack{j,k=1 \\ j,k\neq i}}^{4} g^{\alpha[\mu}p_j^\nu p_k^{\rho]}D_{00j_ik_i}(i) + g^{\alpha[\mu}g^{\nu\rho]}[D^{(\mathrm{fin})}_{0000}(i) - D^{(\mathrm{fin})}_{0000}(0)] \\
&\quad - \sum_{j,k=2}^{4} g^{\alpha[\mu}(p_1-p_j)^\nu(p_1-p_k)^{\rho]}\tilde{D}_{00,j-1,k-1}(0) \\
&\quad - p_1^{[\mu}\sum_{j=2}^{4}(p_1-p_j)^{[\nu}g^{\rho]]\alpha}\tilde{D}_{00,j-1}(0) - g^{\alpha[\mu}p_1^\nu p_1^{\rho]}D_{00}(0).
\end{aligned}
\tag{3.85}
$$

Again the redundancy of the coefficients E_{00j} are applied. We then have

$$
\begin{aligned}
E_{00j} &= -\sum_{i=1}^{4} \eta_i D_{00j_i}(i)\bar{\delta}_{ji} - \eta_0 D_{00j}(0) + 2\sum_{i=1}^{4} \zeta_{ji}[D^{(\mathrm{fin})}_{0000}(i) - D^{(\mathrm{fin})}_{0000}(0)], \\
E_{jkl} &= \left\{ 2\sum_{i=1}^{4} \zeta_{ji}[-D_{00kl}(0) + D_{00k_il_i}(i)\bar{\delta}_{ki}\bar{\delta}_{li}] + (k \leftrightarrow j) + (l \leftrightarrow j) \right\} \\
&\quad - \eta_0 D_{jkl}(0) - \sum_{i=1}^{4} \eta_i D_{j_ik_il_i}(i)\bar{\delta}_{ji}\bar{\delta}_{ki}\bar{\delta}_{li} \qquad j,k,l = 1,\ldots,4, \qquad (3.86)
\end{aligned}
$$

with

$$
\begin{aligned}
D_{j11}(0) &= \tilde{D}_{j-1}(0) + \sum_{k,l=1}^{3} \tilde{D}_{j-1,kl}(0) + 2\sum_{k=1}^{3} \tilde{D}_{j-1,k}(0), \\
D_{jk1}(0) &= -\tilde{D}_{j-1,k-1}(0) - \sum_{l=1}^{3} \tilde{D}_{j-1,k-1,l}(0), \\
D_{jkl}(0) &= \tilde{D}_{j-1,k-1,l-1}(0), \\
D_{111}(0) &= -\sum_{j,k,l=1}^{3} \tilde{D}_{jkl}(0) - 3\sum_{j,k=1}^{3} \tilde{D}_{jk}(0) - 3\sum_{j=1}^{3} \tilde{D}_{j}(0) - D_0(0), \\
D_{0011}(0) &= \sum_{j,k=1}^{3} \tilde{D}_{00jk}(0) + 2\sum_{j=1}^{3} \tilde{D}_{00j}(0) + D_{00}(0), \\
D_{00jk}(0) &= \tilde{D}_{00,j-1,k-1}(0), \\
D_{00j1}(0) &= -\sum_{k=1}^{3} \tilde{D}_{00,j-1,k}(0) - \tilde{D}_{00,j-1}(0). \qquad (3.87)
\end{aligned}
$$

Rank four tensor integrals

$$
\begin{aligned}
E^{\mu\nu\rho\sigma} &= \sum_{j,k,l,m=1}^{4} p_j^\mu p_k^\nu p_l^\rho p_m^\sigma E_{jklm} + \sum_{j,k=1}^{4} (g^{[\mu\nu} p_j^{\rho]} p_k^\sigma + g^{\sigma[\mu} p_j^\nu p_k^{\rho]}) E_{00jk} + g^{[\mu\nu} g^{\rho]\sigma} E_{0000}, \\
D^{\mu\nu\rho\sigma,(\mathrm{fin})}(i) &= \sum_{\substack{j,k,l,m=1 \\ j,k,l,m\neq i}}^{4} p_j^\mu p_k^\nu p_l^\rho p_m^\sigma D_{j_i k_i l_i m_i}(i) + \sum_{\substack{j,k=1 \\ j,k\neq i}}^{4} (g^{[\mu\nu} p_j^{\rho]} p_k^\sigma + g^{\sigma[\mu} p_j^\nu p_k^{\rho]}) D_{00 j_i k_i}(i) \\
&\quad + g^{[\mu\nu} g^{\rho]\sigma} D_{0000}^{(\mathrm{fin})}(i), \qquad i = 1, \ldots, 4, \\
D^{\mu\nu\rho\sigma,(\mathrm{fin})}(0) &= p_1^\mu p_1^\nu p_1^\rho p_1^\sigma D_0(0) - p_1^{[\mu} p_1^\nu p_1^\rho \tilde{D}^{\sigma]}(0) + p_1^\sigma p_1^{[\mu} \tilde{D}^{\nu\rho]}(0) + p_1^{[\mu} p_1^\nu \tilde{D}^{\rho]\sigma}(0) \\
&\quad - p_1^{[\mu} \tilde{D}^{\nu\rho\sigma]}(0) + \tilde{D}^{\mu\nu\rho\sigma,(\mathrm{fin})}(0) \\
&= \sum_{j,k,l,m=2}^{4} (p_1 - p_j)^\mu (p_1 - p_k)^\nu (p_1 - p_l)^\rho (p_1 - p_m)^\sigma \tilde{D}_{j-1,k-1,l-1,m-1}(0) \\
&\quad + \sum_{j,k=2}^{4} [g^{[\mu\nu} (p_1 - p_j)^{\rho]} (p_1 - p_k)^\sigma + g^{\sigma[\mu} (p_1 - p_j)^\nu (p_1 - p_k)^{\rho]}] \tilde{D}_{00,j-1,k-1}(0) \\
&\quad + g^{[\mu\nu} g^{\rho]\sigma} D_{0000}^{(\mathrm{fin})}(0) + p_1^{[\mu} \sum_{j,k,l=2}^{4} (p_1 - p_j)^\nu (p_1 - p_k)^\rho (p_1 - p_l)^{\sigma]} \tilde{D}_{j-1,k-1,l-1}(0) \\
&\quad + p_1^{[\mu} \sum_{j=2}^{4} g^{[\nu\rho} (p_1 - p_j)^{\sigma]]} \tilde{D}_{00,j-1}(0) \\
&\quad + \sum_{j,k=2}^{4} [p_1^{[\mu} p_1^\nu (p_1 - p_j)^{\rho]} (p_1 - p_k)^\sigma + p_1^\sigma p_1^{[\mu} (p_1 - p_j)^\nu (p_1 - p_k)^{\rho]}] \tilde{D}_{j-1,k-1}(0) \\
&\quad + (p_1^{[\mu} p_1^\nu g^{\rho]\sigma} + p_1^\sigma p_1^{[\mu} g^{\nu\rho]}) D_{00}(0) \\
&\quad - p_1^{[\mu} p_1^\nu p_1^\rho \sum_{j=2}^{4} (p_j - p_1)^{\sigma]} \tilde{D}_{j-1}(0) + p_1^\mu p_1^\nu p_1^\rho p_1^\sigma D_0(0),
\end{aligned}
\tag{3.88}
$$

$$
\begin{aligned}
\mathcal{D}^{\alpha\mu\nu\rho\sigma}(i) &= \Big[-D^{\alpha\mu\nu\rho\sigma,(\mathrm{fin})}(0)+D^{\alpha\mu\nu\rho\sigma,(\mathrm{fin})}(i)\Big]^{(g)} \\
&= \Big[D^{\alpha\mu\nu\rho\sigma,(\mathrm{fin})}(i)-\tilde{D}^{\alpha\sigma[\rho}(0)p_1^{\mu}p_1^{\nu]}-\tilde{D}^{\alpha[\nu\rho}(0)p_1^{\mu]}p_1^{\sigma} \\
&\quad +\tilde{D}^{\alpha[\sigma}(0)p_1^{\mu}p_1^{\nu}p_1^{\rho]}+\tilde{D}^{\alpha[\nu\rho\sigma,(\mathrm{fin})}(0)p_1^{\mu]}-\tilde{D}^{\alpha\mu\nu\rho\sigma,(\mathrm{fin})}(0)\Big]^{(g)} \\
&= \sum_{\substack{j,k,l=1\\ j,k,l\neq i}}^{4} g^{\alpha[\mu}p_j^{\nu}p_k^{\rho}p_l^{\sigma]}D_{00j_ik_il_i}(i)+\sum_{\substack{j=1\\ j\neq i}}^{4} g^{\alpha[\mu}g^{[\nu\rho}p_j^{\sigma]]}D^{(\mathrm{fin})}_{0000j_i}(i) \\
&\quad +\sum_{j,k,l=2}^{4} g^{\alpha[\mu}(p_1-p_j)^{\nu}(p_1-p_k)^{\rho}(p_1-p_l)^{\sigma]}\tilde{D}_{00,j-1,k-1,l-1}(0) \\
&\quad +\sum_{j=2}^{4} g^{\alpha[\mu}g^{[\nu\rho}(p_1-p_j)^{\sigma]]}\tilde{D}^{(\mathrm{fin})}_{0000,j-1}(0) \\
&\quad +p_1^{[\mu}g^{[\nu\rho}g^{\sigma]]\alpha}D^{(\mathrm{fin})}_{0000}(0)+\sum_{j,k=2}^{4} p_1^{[\mu}(p_1-p_j)^{[\nu}(p_1-p_k)^{\rho}g^{\sigma]]\alpha}\tilde{D}_{00,j-1,k-1}(0) \\
&\quad +\sum_{j=2}^{4}\Big[p_1^{[\mu}p_1^{\nu}(p_1-p_j)^{\rho]}g^{\sigma\alpha}+p_1^{[\mu}p_1^{\nu}g^{\rho]\alpha}(p_1-p_j)^{\sigma} \\
&\qquad +p_1^{\sigma}p_1^{[\mu}(p_1-p_j)^{[\nu}g^{\rho]]\alpha}\Big]\tilde{D}_{00,j-1}(0)+p_1^{[\mu}p_1^{\nu}p_1^{\rho}g^{\sigma]\alpha}D_{00}(0). \qquad (3.89)
\end{aligned}
$$

With the freedom of choosing the coefficients E_{00jk} and E_{0000}, we have

$$
\begin{aligned}
E_{0000} &= -\eta_0 D^{(\mathrm{fin})}_{0000}(0) - \sum_{i=1}^{4} \eta_i D^{(\mathrm{fin})}_{0000}(i) - \frac{1}{48}\frac{\det(Z^{(4)})}{\det(Y)}, \\
E_{00jk} &= -\eta_0 D_{00jk}(0) - \sum_{i=1}^{4} \eta_i D_{00j_ik_i}(i)\bar{\delta}_{ji}\bar{\delta}_{ki} \\
&\quad + \left\{ 2\sum_{i=1}^{4} \zeta_{ji}[-D^{(\mathrm{fin})}_{0000k}(0) + D^{(\mathrm{fin})}_{0000k_i}(i)\bar{\delta}_{ki}] + (j \leftrightarrow k) \right\}, \\
E_{jklm} &= -\eta_0 D_{jklm}(0) - \sum_{i=1}^{4} \eta_i D_{j_ik_il_im_i}(i)\bar{\delta}_{ji}\bar{\delta}_{ki}\bar{\delta}_{li}\bar{\delta}_{mi} \\
&\quad + \Bigg\{ 2\sum_{i=1}^{4} \zeta_{ji}[-D_{00klm}(0) + D_{00k_il_im_i}(i)\bar{\delta}_{ki}\bar{\delta}_{li}\bar{\delta}_{mi}] \\
&\qquad + (k \leftrightarrow j) + (l \leftrightarrow j) + (m \leftrightarrow j) \Bigg\}, \qquad j,k,l,m = 1,\ldots,4, \qquad (3.90)
\end{aligned}
$$

with

$$
\begin{aligned}
D_{jklm}(0) &= \tilde{D}_{j-1,k-1,l-1,m-1}(0), \\
D_{jkl1}(0) &= -\tilde{D}_{j-1,k-1,l-1}(0) - \sum_{m=1}^{3} \tilde{D}_{j-1,k-1,l-1,m}(0), \\
D_{jk11}(0) &= \tilde{D}_{j-1,k-1}(0) + \sum_{l,m=1}^{3} \tilde{D}_{j-1,k-1,lm}(0) + 2\sum_{l=1}^{3} \tilde{D}_{j-1,k-1,l}(0), \\
D_{j111}(0) &= -\sum_{k,l,m=1}^{3} \tilde{D}_{j-1,klm}(0) - 3\sum_{k,l=1}^{3} \tilde{D}_{j-1,kl}(0) - 3\sum_{k=1}^{3} \tilde{D}_{j-1,k}(0) - \tilde{D}_{j-1}(0), \\
D_{1111}(0) &= \sum_{j,k,l,m=1}^{3} \tilde{D}_{jklm}(0) + 4\sum_{j,k,l=1}^{3} \tilde{D}_{jkl}(0) + 6\sum_{j,k=1}^{3} \tilde{D}_{jk}(0) + 4\sum_{j=1}^{3} \tilde{D}_{j}(0) + D_0(0), \\
D_{00jkl}(0) &= \tilde{D}_{00,j-1,k-1,l-1}(0), \\
D_{00jk1}(0) &= -\sum_{l=1}^{3} \tilde{D}_{00,j-1,k-1,l}(0) - \tilde{D}_{00,j-1,k-1}(0), \\
D_{00j11}(0) &= \sum_{k,l=1}^{3} \tilde{D}_{00,j-1,kl}(0) + 2\sum_{k=1}^{3} \tilde{D}_{00,j-1,k}(0) + \tilde{D}_{00,j-1}(0), \\
D^{(\mathrm{fin})}_{0000j}(0) &= \tilde{D}^{(\mathrm{fin})}_{0000,j-1}(0), \\
D^{(\mathrm{fin})}_{00001}(0) &= -\sum_{j=1}^{3} \tilde{D}^{(\mathrm{fin})}_{0000j}(0) - D^{(\mathrm{fin})}_{0000}(0), \\
D_{00111}(0) &= -\sum_{j,k,l=1}^{3} \tilde{D}_{00jkl}(0) - 3\sum_{j,k=1}^{3} \tilde{D}_{00jk}(0) - 3\sum_{j=1}^{3} \tilde{D}_{00j}(0) - D_{00}(0),
\end{aligned}
\tag{3.91}
$$

where $j, k, l, m = 2, 3, 4$.

3.4.3 The N-point functions with zero Gram determinant

For vanishing Gram determinant, $|X_{N-1}|$, the following relation holds if the Lorentz decomposition of the appearing tensor integrals contains only momenta and no metric tensors, which is the case for $N \geq 6$ or $r = 0$ (scalar integrals)

$$\frac{(2\pi\mu)^{4-D}}{i\pi^2}\int d^Dq \frac{q_{\mu_1}\cdots q_{\mu_r}}{D_0 D_1 \cdots D_{N-1}} \begin{vmatrix} D_0 + Y_{00} & 2qp_1 & \dots & 2qp_{N-1} \\ Y_{10} - Y_{00} & 2p_1^2 & \dots & 2p_1p_{N-1} \\ \vdots & \vdots & \ddots & \vdots \\ Y_{N-10} - Y_{00} & 2p_{N-1}p_1 & \dots & 2p_{N-1}^2 \end{vmatrix} = 0. \tag{3.92}$$

Performing the same manipulations of the determinant as in Equation 3.92 to Equation 3.77 above this results in

$$\begin{vmatrix} T^N_{\mu_1\dots\mu_r} & -T^{N-1}_{\mu_1\dots\mu_r}(0) & -T^{N-1}_{\mu_1\dots\mu_r}(1) & \dots & -T^{N-1}_{\mu_1\dots\mu_r}(N-1) \\ 1 & Y_{00} & Y_{01} & \dots & Y_{0N-1} \\ 1 & Y_{10} & Y_{11} & \dots & Y_{1N-1} \\ \vdots & \vdots & \vdots & \ddots & \vdots \\ 1 & Y_{N-10} & Y_{N-11} & \dots & Y_{N-1N-1} \end{vmatrix} = 0, \tag{3.93}$$

valid for $|X_{N-1}| = 0$ and $r = 0$ or $N \geq 5$. Notice that the momenta are not shifted for the tensor integral $T^N_{\mu_1 \ldots \mu_r}(0)$ in Equation 3.93. If the determinant of the matrix Y_{ij} is nonvanishing, $T^N_{\mu_1 \ldots \mu_r}$ in terms of $T^{N-1}_{\mu_1 \ldots \mu_r}(i)$, $i = 0, \ldots, N-1$ is determined by Equation 3.93. It is clear that T^{N-1} does not contain the leading Landau singularity of T^N, which leads to the vanishing of this determinant Therefore, we have to calculate T^N directly [88] for this case. For $N \leq 4$, Equation 3.93 is valid only at the edge of phase space which consist of some collinear momenta p_i that lead to a vanishing Gram determinant. For $r = 0$ and $N = 5$, Equation 3.93 coincides with Equation 3.77. For $N > 6$, arbitrary six denominator factors can be chosen to give further reductions. Because in these special situations, we can reduce all integrals to tensor integrals with smaller N and obtain simpler results compared to the general case [92, 93]. Note that the reduction could generate tensor integrals with $r > N$ since r is not simultaneously reduced.

3.5 UV-divergent parts

Isolating the UV-divergent parts from the tensor integrals is useful in practical calculation. We therefore list common divergent one-loop tensor integrals below

$$
\begin{aligned}
A_0(m) &= \tfrac{m^2}{\epsilon}, \\
B_0(p_{10}, m_0, m_1) &= \tfrac{1}{\epsilon}, \\
B_1(p_{10}, m_0, m_1) &= \tfrac{-1}{2\epsilon}, \\
B_{00}(p_{10}, m_0, m_1) &= \tfrac{-1}{12\epsilon}(p_{10}^2 - 3m_0^2 - 3m_1^2), \\
B_{11}(p_{10}, m_0, m_1) &= \tfrac{1}{3\epsilon}, \\
C_{00}(p_{10}, p_{20}, m_0, m_1, m_2) &= \tfrac{1}{4\epsilon}, \\
C_{00i}(p_{10}, p_{20}, m_0, m_1, m_2) &= \tfrac{-1}{12\epsilon}, \\
D_{0000}(p_{10}, p_{20}, p_{30}, m_0, m_1, m_2, m_3) &= \tfrac{1}{24\epsilon}.
\end{aligned}
\tag{3.94}
$$

All other scalar coefficients defined in Equation 3.10 and Equation 3.11 are UV-finite.

3.6 The OPP method

Besides the analytical reduction of tensor integrals, which have been discussed in Section 3.2, a new development called OPP method for calculating loop integrals has been introduced. In this new method, the computation of tensor integrals is replaced by numerically finding the coefficients of the corresponding scalar n-point functions since Boxes, Triangles, Bubbles, and Tadpoles one-loop integrals form the basis of one-loop amplitudes. For arbitrary one-loop amplitude, we can write down the following equations

$$\mathcal{M} = \sum_i d_i \text{ Box}_i + \sum_i c_i \text{ Triangle}_i + \sum_i b_i \text{ Bubble}_i + \sum_i a_i \text{ Tadpole}_i + \text{R}\,, \tag{3.95}$$

where d_i, c_i, b_i and a_i are the coefficients to be determined.

3.6.1 Introduction

The OPP [94] reduction method is developed for the numerical computation of (sub-)amplitudes with one-loop N-point functions.

$$\bar{\mathcal{M}}(\bar{q}) = \frac{\bar{N}(\bar{q})}{\bar{D}_0 \bar{D}_1 \cdots \bar{D}_{m-1}}\,, \quad \bar{D}_i = (\bar{q} + p_i)^2 - m_i^2\,, \quad p_0 \neq 0\,. \tag{3.96}$$

Here, dimensional regularization is imposed on Equation 3.96, and symbols with a bar indicate n-dimensional objects with $n = 4 + \epsilon$. We have $\bar{q}^2 = \tilde{q}^2 + q^2$, where $\tilde{q}$ is ϵ-dimensional vector and $\tilde{q} \cdot q = 0$. Similarly, we can split the numerator function $\bar{N}(\bar{q})$ into two parts

$$\bar{N}(\bar{q}) = N(q) + \tilde{N}(q, \tilde{q}, \epsilon)\,. \tag{3.97}$$

$N(q)$ is 4-dimensional while the ϵ-dimensional term $\tilde{N}(q, \tilde{q}, \epsilon)$ leads to the R_2 rational terms which will be discussed in Section 3.6.3

The $N(q)$ can be written in terms of $D_i = (q + p_i)^2 - m_i^2$, the 4-dimensional denominators, as

$$
\begin{aligned}
N(q) &= \sum_{i_0<i_1<i_2<i_3}^{m-1} \Big[d(i_0 i_1 i_2 i_3) + \tilde{d}(q; i_0 i_1 i_2 i_3) \Big] \prod_{i \neq i_0, i_1, i_2, i_3}^{m-1} D_i \\
&+ \sum_{i_0<i_1<i_2}^{m-1} [c(i_0 i_1 i_2) + \tilde{c}(q; i_0 i_1 i_2)] \prod_{i \neq i_0, i_1, i_2}^{m-1} D_i \\
&+ \sum_{i_0<i_1}^{m-1} \Big[b(i_0 i_1) + \tilde{b}(q; i_0 i_1) \Big] \prod_{i \neq i_0, i_1}^{m-1} D_i \\
&+ \sum_{i_0}^{m-1} [a(i_0) + \tilde{a}(q; i_0)] \prod_{i \neq i_0}^{m-1} D_i \\
&+ \tilde{P}(q) \prod_{i}^{m-1} D_i \,. \qquad (3.98)
\end{aligned}
$$

We can decompose scalar m-point functions with $m > 4$ into boxes which contribute at order $\mathcal{O}(\epsilon)$, therefore Equation 3.98 only has terms up to 4 poles. The contribution of the last term ,$\tilde{P}(q)$, has no poles, vanishes in practical calculations when $\lambda \to \infty$ since $N(\lambda q) \to \lambda^m$ for large *lambda*. We can further split the coefficients of the poles into two parts. The first part is independent of q (terms like a, b, c, d). The other part is q-dependant (the terms $\tilde{a}$, $\tilde{b}$, $\tilde{c}$, $\tilde{d}$), and they vanish after integration due to the Lorentz invariance. We can always perform such a separation, as shown in [94]. In addition, we can interpret the first part of coefficients as an ensemble of all possible one, two, three, four-point one-loop integrals' coefficients that contribute to the amplitude with this choice. The task of computing the one-loop amplitude can be simplified to finding the best fitting of coefficients d, c, b, a algebraically as long as Equation 3.98 is established. To fit the coefficients, we can evaluate $N(q)$ multiple times with different q and then solve for the linear equations. Notice that we can perform such an algorithm at

the amplitude level. Repetitive computations of Feynman diagrams are not needed if we can evaluate $N(q)$ numerically. Moreover, n-dimensional denominators $\bar{D}_i$ appear in Equation 3.96, that differ from their 4-dimensional counterparts by an amount $\tilde{q}^2$

$$\bar{D}_i - D_i = \tilde{q}^2 \tag{3.99}$$

The Rational Part is from the terms survive after the cancelling the 4-dimensional terms of the `OPP` expansion, Equation 3.98, and the n-dimensional denominators of Equation 3.96, which is the result of Equation 3.99. By inserting Equation 3.99 into Equation 3.98, we can decompose $N(q)$ into n-dimensional denominators to restore the exact cancellation. However, an extra term, $f(q, \tilde{q})$, will be added for such decomposition. The R_1 rational terms are defined as

$$\mathrm{R}_1 \equiv \frac{1}{(2\pi)^4} \int d^n\, \bar{q} \frac{f(\tilde{q}^2, q)}{\bar{D}_0 \bar{D}_1 \cdots \bar{D}_{m-1}} \,. \tag{3.100}$$

We can rewrite any denominator appearing in Equation 3.96 and explicitly obtain the function, $f(q, \tilde{q})$, as follows

$$\frac{1}{\bar{D}_i} = \frac{\bar{Z}_i}{D_i} \,, \quad \text{where} \quad \bar{Z}_i \equiv \left(1 - \frac{\tilde{q}^2}{\bar{D}_i}\right) \,. \tag{3.101}$$

This leads to

$$\bar{\mathcal{M}}(\bar{q}) = \frac{N(q)}{D_0 D_1 \cdots D_{m-1}} \bar{Z}_0 \bar{Z}_1 \cdots \bar{Z}_{m-1} + \mathcal{R}_2 \,, \tag{3.102}$$

where $\mathcal{R}_2$ is the integrand function came from the ϵ-dimensional term $\tilde{N}(\tilde{q}^2, q, \epsilon)$ in Equation 3.97 , which will be discussed in Equation 3.112. Then, by inserting Equation 3.98 in Equation 3.102, one obtains

$$\begin{aligned}
\bar{\mathcal{M}}(\bar{q}) &= \sum_{i_0<i_1<i_2<i_3}^{m-1} \frac{d(i_0 i_1 i_2 i_3) + \tilde{d}(q; i_0 i_1 i_2 i_3)}{\bar{D}_{i_0} \bar{D}_{i_1} \bar{D}_{i_2} \bar{D}_{i_3}} \prod_{i \neq i_0, i_1, i_2, i_3}^{m-1} \bar{Z}_i \\
&+ \sum_{i_0<i_1<i_2}^{m-1} \frac{c(i_0 i_1 i_2) + \tilde{c}(q; i_0 i_1 i_2)}{\bar{D}_{i_0} \bar{D}_{i_1} \bar{D}_{i_2}} \prod_{i \neq i_0, i_1, i_2}^{m-1} \bar{Z}_i \\
&+ \sum_{i_0<i_1}^{m-1} \frac{b(i_0 i_1) + \tilde{b}(q; i_0 i_1)}{\bar{D}_{i_0} \bar{D}_{i_1}} \prod_{i \neq i_0, i_1}^{m-1} \bar{Z}_i \\
&+ \sum_{i_0}^{m-1} \frac{a(i_0) + \tilde{a}(q; i_0)}{\bar{D}_{i_0}} \prod_{i \neq i_0}^{m-1} \bar{Z}_i \\
&+ \tilde{P}(q) \prod_{i}^{m-1} \bar{Z}_i + \mathcal{R}_2 \,.
\end{aligned} \tag{3.103}$$

The $\tilde{q}^2$ dependence from the various $\bar{Z}_i$ in Equation 3.103 gives rise to R_1 after integrating over $d^n \bar{q}$. This procedure is utilized in [95], where all required integrals are explicitly computed and classified.

However, the derivation of R_1 shown above has two disadvantages. One disadvantage is that the information of the spurious terms [1] is required. The other is that when calculating combined diagrams, new rational parts may arise due to terms that contain $\tilde{q}^2$ appear in the numerator when taking common denominators. Calculating these new rational part is equal to treating each diagram separately, which jeopardize the ability to deal with the amplitude for the OPP technique in 4-dimensional spacetime. Therefore, we need a different way to solve this problem without relying on spurious terms. In the next section, we will introduce this new method, which allows the combination of diagrams without fitting the coefficients a, b, c, d presented. This second method, which has already been successfully implemented in Fortran [96], is proved better for numerical implementation.

3.6.2 R_1 rational terms

We can compute the R_1 rational terms by rebuilding powers of $\tilde{q}^2$, i.e., finding the implicit mass dependence, in the coefficients b, c, d, where $\tilde{q}^2$ is reentered by shifting mass

$$m_i^2 \to m_i^2 - \tilde{q}^2 \,. \tag{3.104}$$

This procedure is formally equivalent to the applications of n-dimensional cuts in the generalized unitarity framework and is obtained by decomposing Equation 3.98 into n-dimensional denominators in Equation 3.99. By performing the decomposition, all coefficients of the OPP

[1] After multiplication with the $\bar{Z}_i$, they give nonvanishing contributions.

expansion start depending on $\tilde{q}^2$. Due to Lorentz invariance, the spurious terms vanish. The coefficients b, c, d give the following integrals [94]

$$\begin{aligned}
\int d^n\bar{q}\frac{\tilde{q}^2}{\bar{D}_i\bar{D}_j} &= -\frac{i\pi^2}{2}\left[m_i^2+m_j^2-\frac{(p_i-p_j)^2}{3}\right]+\mathcal{O}(\epsilon)\,,\\
\int d^n\bar{q}\frac{\tilde{q}^2}{\bar{D}_i\bar{D}_j\bar{D}_k} &= -\frac{i\pi^2}{2}+\mathcal{O}(\epsilon)\,,\\
\int d^n\bar{q}\frac{\tilde{q}^4}{\bar{D}_i\bar{D}_j\bar{D}_k\bar{D}_l} &= -\frac{i\pi^2}{6}+\mathcal{O}(\epsilon)\,.
\end{aligned} \tag{3.105}$$

We can prove the following relations

$$\begin{aligned}
b(ij;\tilde{q}^2) &= b(ij)+\tilde{q}^2 b^{(2)}(ij)\,,\\
c(ijk;\tilde{q}^2) &= c(ijk)+\tilde{q}^2 c^{(2)}(ijk)\,.
\end{aligned} \tag{3.106}$$

Moreover, by applying Equation 3.104, we can define the first line of Equation 3.98 as

$$\mathcal{D}^{(m)}(q,\tilde{q}^2)\equiv\sum_{i_0<i_1<i_2<i_3}^{m-1}\Big[d(i_0i_1i_2i_3;\tilde{q}^2)+\tilde{d}(q;i_0i_1i_2i_3;\tilde{q}^2)\Big]\prod_{i\neq i_0,i_1,i_2,i_3}^{m-1}\bar{D}_i\,, \tag{3.107}$$

and

$$\mathcal{D}^{(m)}(q,\tilde{q}^2)=\sum_{j=2}^{m}\tilde{q}^{(2j-4)}d^{(2j-4)}(q)\,, \tag{3.108}$$

where the last coefficient is q independent. We therefore have

$$d^{(2m-4)}(q) = d^{(2m-4)} \,. \tag{3.109}$$

Practically, as long as we have determined the 4-dimensional coefficients, we can simply use different values of $\tilde{q}^2$ to find new $d^{(2m-4)}$, $c^{(2)}(ijk)$ and $b^{(2)}(ij)$, the coefficients of the three extra scalar integrals shown in Equation 3.105. We have

$$\begin{aligned} \mathrm{R}_1 &= -\frac{i}{96\pi^2} d^{(2m-4)} - \frac{i}{32\pi^2} \sum_{i_0<i_1<i_2}^{m-1} c^{(2)}(i_0 i_1 i_2) \\ &- \frac{i}{32\pi^2} \sum_{i_0<i_1}^{m-1} b^{(2)}(i_0 i_1) \left(m_{i_0}^2 + m_{i_1}^2 - \frac{(p_{i_0} - p_{i_1})^2}{3} \right) . \end{aligned} \tag{3.110}$$

The other way of evaluating $d^{(2m-4)}$, also implemented in the code of [96], is

$$d^{(2m-4)} = \lim_{\tilde{q}^2 \to \infty} \frac{\mathcal{D}^{(m)}(q, \tilde{q}^2)}{\tilde{q}^{(2m-4)}} \,. \tag{3.111}$$

3.6.3 The origin of R_2

$\tilde{N}(\tilde{q}, q, \epsilon)$ in Equation 3.97 leads to the R_2 rational terms, which can be defined as

$$\mathrm{R}_2 \equiv \frac{1}{(2\pi)^4} \int d^n \, \bar{q} \frac{\tilde{N}(\tilde{q}^2, q, \epsilon)}{\bar{D}_0 \bar{D}_1 \cdots \bar{D}_{m-1}} \equiv \frac{1}{(2\pi)^4} \int d^n \, \bar{q} \, \mathcal{R}_2 \,. \tag{3.112}$$

The separation in Equation 3.97 need to be studied further to obtain $\tilde{N}(\tilde{q}, q, \epsilon)$ explicitly. From the integrand, $\bar{\mathcal{M}}(\bar{q})$, which is obtained by splitting the n-dimensional metric tensor $\bar{g}^{\bar{\mu}\bar{\nu}}$, γ matrices $\bar{\gamma}_{\bar{\mu}}$, integration momentum $\bar{q}$, and the numerator function as follows

$$\begin{aligned} \bar{g}^{\bar{\mu}\bar{\nu}} &= g^{\mu\nu} + \tilde{g}^{\tilde{\mu}\tilde{\nu}}\,, \\ \bar{q} &= q + \tilde{q}\,, \\ \bar{\gamma}_{\bar{\mu}} &= \gamma_\mu + \tilde{\gamma}_{\tilde{\mu}}\,. \end{aligned} \tag{3.113}$$

We stress that the 4-dimensional part is selected automatically when the external 4-dimensional vector v_μ is contracted with the n-dimensional index. For example

$$\bar{\not{p}} = \not{p} \quad \text{and} \quad v \cdot \bar{q} = v \cdot q\,. \tag{3.114}$$

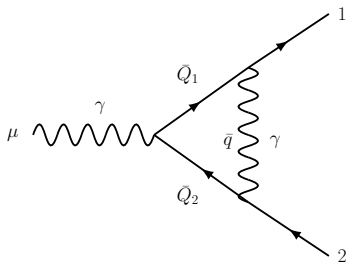

Figure 2. *One-loop QED electron vertex diagram in n dimensions.*

With all ϵ-dimensional terms included by using γ-algebra [1], the numerator reads

$$\begin{aligned}
\bar{N}(\bar{q}) &\equiv e^3 \left\{ \bar{\gamma}_{\bar{\beta}} \left(\bar{\not{Q}}_1 + m_e \right) \gamma_\mu \left(\bar{\not{Q}}_2 + m_e \right) \bar{\gamma}^{\bar{\beta}} \right\} \\
&= e^3 \left\{ \gamma_\beta (\not{Q}_1 + m_e) \gamma_\mu (\not{Q}_2 + m_e) \gamma^\beta \right. \\
&- \left. \epsilon \, (\not{Q}_1 - m_e) \gamma_\mu (\not{Q}_2 - m_e) + \epsilon \tilde{q}^2 \, \gamma_\mu - \tilde{q}^2 \, \gamma_\beta \gamma_\mu \gamma^\beta \right\} , \qquad (3.115)
\end{aligned}$$

The first term on RHS of Equation 3.115 corresponds to $N(q)$, while $\tilde{N}(q, \tilde{q}, \epsilon)$ is the sum of the other three terms. Inserting $\tilde{N}(q, \tilde{q}, \epsilon)$ to Equation 3.112 and using the the following relations

$$\begin{aligned}
\int d^n \bar{q} \frac{\tilde{q}^2}{\bar{D}_0 \bar{D}_1 \bar{D}_2} &= -\frac{i\pi^2}{2} + \mathcal{O}(\epsilon) , \\
\int d^n \bar{q} \frac{q_\mu q_\nu}{\bar{D}_0 \bar{D}_1 \bar{D}_2} &= -\frac{i\pi^2}{2\epsilon} g_{\mu\nu} + \mathcal{O}(1) , \qquad (3.116)
\end{aligned}$$

gives

$$\mathrm{R}_2 = -\frac{ie^3}{8\pi^2} \gamma_\mu + \mathcal{O}(\epsilon) . \qquad (3.117)$$

In general, we can reduce the calculation of R_2 to a tree-level one. Therefore, the full $\mathrm{R} = \mathrm{R}_1 + \mathrm{R}_2$ can be determined and we can calculate any Feynman amplitude as long as

---

[1] The ϵ-dimensional γ matrices anti-commute with 4-dimensional γ matrices : $\{\tilde{\gamma}_\nu, \gamma_\mu\} = 0$.

corresponding R_2 terms are precalculated. In dimensional regularization, only the full rational term R composes a physical gauge-invariant quantity.

CHAPTER 4

DOUBLE HIGGS PRODUCTION

Scientists have finished the first step of probing of the mechanism giving rise to the spontaneous symmetry breaking and generating the masses of gauge bosons and fermions after the ATLAS and CMS Collaborations at the LHC [4, 5] discovered a boson-like particle with the mass around 125 GeV, and the properties consistent with the long-sought Standard Model Higgs boson [7, 8, 7, 10]. Now, an equally important task is to determine the properties of the bosonic particle precisely. It is crucial to confirm that this particle is indeed the Higgs boson we are seeking and, eventually, to discover the new physics effects. To verify the Standard Model prediction that the masses of fermions and gauge bosons are indeed proportional to its couplings to the Higgs boson, a precise determination of these couplings are required. Furthermore, the only method of reconstructing the scalar potential, H, and then the Higgs doublet field Φ, which leads to spontaneous electroweak symmetry breaking, is through measuring the Higgs self-interactions.

$$V_H = -\mu^2 \Phi^\dagger \Phi + \frac{1}{2}\lambda(\Phi^\dagger \Phi)^2 \; ; \lambda = \frac{m_H^2}{v^2} \textbf{ and } \mu^2 = \frac{1}{2} m_H^2 \, , \tag{4.1}$$

where H is the physical Higgs field and $v \approx 246$ GeV is the vacuum expectation value (vev). By expanding the Higgs field around its vev, the Higgs self-interactions, including the corresponding permutations, are

$$g_{H^3} = 3\frac{m_H^2}{v}, \qquad g_{H^4} = 3\frac{m_H^2}{v^2}\,, \tag{4.2}$$

where g_{H^3} and g_{H^4} represent the trilinear and quartic Higgs self-coupling, respectively. The trilinear Higgs self-coupling can only be directly accessed through Higgs-pair production [97, 98, 99, 100, 101, 102]. Thus, we need to consider the process that the singly produced off-shell Higgs boson splits into two on-shell Higgs bosons.

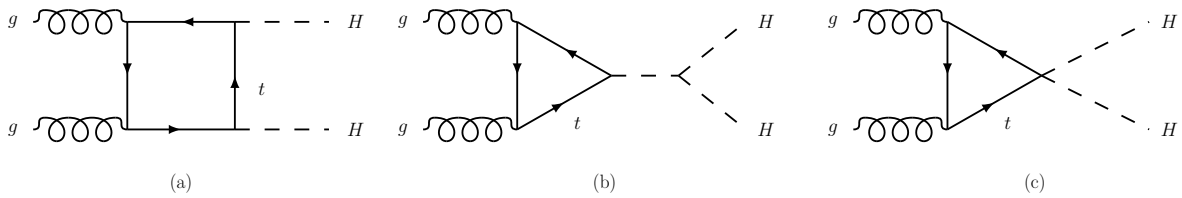

Figure 3. *Feynman diagrams for loop-induced Higgs pair production through gluon fusion. Diagrams* (a), *b* are SM diagrams, where *(c)* is BSM diagram with anomalous $HHtt$ coupling.

4.1 Leading-order Cross-section

SM contributions to calculations of Higgs pair production have been made a while back in [29, 31]. Also, the extra contribution from the anomalous $HHtt$ coupling has been studied in [59, 60]. At the leading-order, the production of the Higgs pair through gluon fusion is shown

in Figure 3, including each permutation of the external lines. The box diagram has no Higgs self-coupling, and the triangle diagram involves the Higgs trilinear coupling via an s-channel Higgs exchange. The matrix element of $g(p_1)g(p_2) \to H(p_3)H(p_4)$ at LO can be written as

$$\begin{aligned}
\mathcal{M}(g^a g^b \to HH) &= -i\,\frac{G_F \alpha_s(\mu_R) m_{HH}^2}{2\sqrt{2}\pi}\mathcal{A}^{\mu\nu}\epsilon_{1\mu}\epsilon_{2\nu}\delta_{ab} \\
\text{with} \qquad \mathcal{A}^{\mu\nu} &= F_1 T_1^{\mu\nu} + F_2 T_2^{\mu\nu}\,, \\
F_1 &= \left(g_{H^3}\frac{1}{\hat{s}-m_H^2}\; g_{Htt} + g_{HHtt}\right)\frac{v^2}{m_t}F_\triangle + g_{Htt}^2\frac{v^2}{m_t^2}F_\square\,, \\
F_2 &= g_{Htt}^2\frac{v^2}{m_t^2}G_\square\,,
\end{aligned} \tag{4.3}$$

where m_{HH} is the invariant mass of the Higgs pair, a, b are the color indices of the initial gluons, G_F is the Fermi constant, and $\alpha_s(\mu_R)$ is the strong coupling evaluated at the renormalization scale μ_R.

The couplings g_{H^3}, g_{Htt} and g_{HHtt} are the trilinear Higgs coupling, the top-Higgs coupling, and the anomalous nonlinear $HHtt$ coupling, respectively. The Lagrangian that involves these couplings reads

$$\frac{1}{3!}g_{H^3}\,H^3 + g_{Htt}\,H\bar{t}t + \frac{1}{2!}g_{HHtt}\,H^2\bar{t}t\;. \tag{4.4}$$

Therefore in the SM we have

$$g_{H^3}^{(SM)} = \frac{3m_H^2}{v}\;, \qquad g_{Htt}^{(SM)} = \frac{m_t}{v}\;, \qquad g_{HHtt}^{(SM)} = 0\;, \tag{4.5}$$

where $v = 246$ GeV is vacuum expectation value of the Higgs field.

The contributions of the two tensor structures, $T_1^{\mu\nu}$, correspond to the total angular-momentum states with $S_z = 0$ while $T_2^{\mu\nu}$ corresponds to $S_z = 2$,

$$\begin{aligned} T_1^{\mu\nu} &= g^{\mu\nu} - \frac{p_1^\nu p_2^\mu}{(p_1 \cdot p_2)}\,, \\ T_2^{\mu\nu} &= g^{\mu\nu} + \frac{M_H^2 p_1^\nu p_2^\mu}{p_T^2 (p_1 \cdot p_2)} - 2\frac{(p_2 \cdot p_3) p_1^\nu p_3^\mu}{p_T^2 (p_1 \cdot p_2)} - 2\frac{(p_1 \cdot p_3) p_3^\nu p_2^\mu}{p_T^2 (p_1 \cdot p_2)} + 2\frac{p_3^\nu p_3^\mu}{p_T^2} \\ \text{with} \quad p_T^2 &= 2\frac{(p_1 \cdot p_3)(p_2 \cdot p_3)}{(p_1 \cdot p_2)} - M_H^2\,, \end{aligned} \tag{4.6}$$

where p_T is the transverse momentum of each Higgs boson in the final-state.

Here we follow the notations used in [31], the form factors for $gg \to HH$ are

$$
\begin{aligned}
F_{\triangle} &= \frac{2}{S}[2+(4-S)m_t^2 C_{12}] \\
F_{\square} &= \frac{1}{S^2}\big\{4\,S+8S\,m_t^2\,C_{12}-2S\,mt^4\,(S-8+2R_{H/t}^2)(D_{123}+D_{213}+D_{132}) \\
&\quad +(2R_{H/t}^2-8)m_t^2[\bar{T}(C_{13}+C_{24})+\bar{U}(C_{23}+C_{14}) \\
&\quad -(TU-R_{H/t}^4)m_t^2 D_{132}]\big\} \\
G_{\square} &= \frac{1}{S(TU-R_{H/t}^2)}\big\{(T^2-8T+R_{H/t}^2)m_t^2(C_{12}+\bar{T}(C_{13}+C_{24})-STm_t^2 D_{213}) \\
&\quad +m_t^2(U^2-8U+R_{H/t}^2)(SC_{12}+\bar{U}(C_{23}+C_{14})-SUm_t^2 D_{123}) \\
&\quad -m_t^2(T^2+U^2-2R_{H/t}^2)(T+U-8)C_{cd} \\
&\quad -2m_t^2(TU-R_{H/t}^2)(D_{123}+D_{213}+D_{132})\big\},
\end{aligned}
$$

where

$$
\hat{s}=(p_1+p_2)^2, \qquad \hat{t}=(p_3-p_1)^2, \qquad \hat{u}=(p_3-p_2)^2
$$

$$
S=\hat{s}/m_t^2, \qquad T=\hat{t}/m_t^2, \qquad U=\hat{u}/m_t^2
$$

$$
R_{H/t}=m_H^2/m_t^2, \qquad \bar{T}=T-R_{H/t}, \qquad \bar{U}=U-R_{H/t}, \qquad ,
$$

and the scalar integrals:

$$C_{ij} = \int \frac{d^4q}{i\pi^2} \frac{1}{(q^2 - m_Q^2)\left[(q+p_i)^2 - m_Q^2\right]\left[(q+p_i+p_j)^2 - m_Q^2\right]}$$

$$D_{ijk} = \int \frac{d^4q}{i\pi^2} \frac{1}{(q^2 - m_Q^2)\left[(q+p_i)^2 - m_Q^2\right]\left[(q+p_i+p_j)^2 - m_Q^2\right]\left[(q+p_i+p_j+p_k)^2 - m_Q^2\right]}$$

Notice that the loop function of the single Higgs production from the gluon fusion appears again in both Figure 3(b) and Figure 3(c). Only the SM top quark loops are considered in this work due to the smallness of Higgs couplings to other quarks.

For the three diagrams in Figure 3, we can therefore express the partonic differential cross-section as

$$\frac{d\hat{\sigma}(gg \to HH)}{d\hat{t}} = \frac{G_F^2 \alpha_s^2}{512(2\pi)^3} \times \left[\left| \left(g_{H^3} \frac{1}{\hat{s} - m_H^2}\ g_{Htt} + g_{HHtt} \right) \frac{v^2}{m_t} F_\triangle + g_{Htt}^2 \frac{v^2}{m_t^2} F_\square \right|^2 + \left| g_{Htt}^2 \frac{v^2}{m_t^2} G_\square \right|^2 \right] \ . \quad (4.7)$$

In the SM (Equation 4.7) reduces to

$$\frac{G_F^2 \alpha_s^2}{512(2\pi)^3} \left[\left| \frac{3m_H^2}{\hat{s} - m_H^2} F_\triangle + F_\square \right|^2 + |G_\square|^2 \right] \ . \quad (4.8)$$

We can parameterize (Equation 4.7) with three dimensionless coefficients

$$\frac{d\hat{\sigma}(gg \to HH)}{d\hat{t}} = \frac{G_F^2 \alpha_s^2}{512(2\pi)^3} \left[\left| \left(c_{3H} \frac{3m_H^2}{\hat{s} - m_H^2} + c_{HHtt} \right) F_\triangle + c_{Htt} F_\square \right|^2 + |c_{Htt} G_\square|^2 \right] \quad (4.9)$$

In SM, these coefficients reads

$$c_{3H}^{(SM)} = 1 \ , \qquad c_{Htt}^{(SM)} = 1 \ , \qquad c_{HHtt}^{(SM)} = 0 \ . \tag{4.10}$$

The definition of these coefficients are[1]

$$c_{3H} = g_{H^3}\, g_{Htt}\, \frac{v^2}{3m_H^2 m_t} \ , \qquad c_{HHtt} = g_{HHtt}\, \frac{v^2}{m_t} \ , \qquad c_{Htt} = \left(g_{Htt}\, \frac{v}{m_t} \right)^2 \ . \tag{4.11}$$

Only gauge-invariant operators of dimension-6 or higher lead to new physics effects of low-energy Higgs observables in the effective theory framework. We expect the importance of operators with mass dimensions greater than four to become less for lower energy scale. For dimension-6 operators, we have

$$\delta c_{3H,Htt,HHtt} \sim \mathcal{O}\left(\frac{v^2}{\Lambda_{np}^2} \right) \ , \tag{4.12}$$

where $v = 246$ GeV, and Λ_{np} denotes the generic scale of new physics. A bottom-up approach is adopted in this work while c_{3H}, c_{Htt}, and c_{HHtt} are allowed to vary, without the constraints of the power counting in Equation 4.12.

Equation 4.9 is a quite general expression and includes new physics effects from various models. Provided that there are fermions with new color while coupled to the Higgs strongly. In that case, we can include the contributions from these new colors to $gg \to HH$ by applying the

---

[1]Comparing the notations in [103] to our result, we have $c_{3H} = c_{\triangle}$, $c_{Htt} = c_{\square}$, and $c_{HHtt} = c_{nl}$.

mass eigenvalues in the loop functions and calculating the Higgs couplings from the eigenbasis of masses. It is known that the $m_t \to \infty$ limit gives good approximations in $F_\triangle$ but works terribly in $F_\square$ and $G_\square$ [104, 105]. It is known that the $m_t \to \infty$ limit gives good approximations in $F_\triangle$ but works terribly in $F_\square$ and $G_\square$ [104, 105]. Roughly speaking, this is because the partonic CM energy, is the Higgs pair invariant mass, $\hat{s}$, and is always above $4m_h^2$, the kinematic threshold, while the relation $\hat{s} \ll 4m_t^2$ is required in the low-energy Higgs theorems [106]. Therefore, the complete mass dependence must be kept in the loop functions for scenarios with new colored particles, which have been studied thoroughly in [59, 105].

4.2 Corrections up to next-to-leading-order

Generically, the cross-section of double Higgs production up to next-to-leading-order can be expressed as [24]

$$\sigma_{NLO}(pp \to HH + X) \;=\; \sigma_{LO} + \Delta\sigma_{virt} + \Delta\sigma_{gg} + \Delta\sigma_{gq} + \Delta\sigma_{q\bar{q}}\,.$$

Here we define

$$\begin{aligned}
\sigma_{LO} &= \int_{\tau_0}^1 d\tau\, \frac{d\mathcal{L}^{gg}}{d\tau}\, \hat{\sigma}_{LO}(Q^2 = \tau s)\,, \\
\Delta\sigma_{virt} &= \frac{\alpha_s(\mu_R)}{\pi} \int_{\tau_0}^1 d\tau\, \frac{d\mathcal{L}^{gg}}{d\tau}\, \hat{\sigma}_{virt}(Q^2 = \tau s)\,, \\
\Delta\sigma_{ij} &= \frac{\alpha_s(\mu_R)}{\pi} \int_{\tau_0}^1 d\tau\, \frac{d\mathcal{L}^{ij}}{d\tau} \int_{\tau_0/\tau}^1 \frac{dz}{z}\, \hat{\sigma}_{ij}(Q^2 = z\tau s) \qquad (ij = gg, gq, q\bar{q})\,,
\end{aligned} \tag{4.13}$$

where $\hat{\sigma}_{LO/virt/ij}(Q^2)$ denote the partonic cross-sections. The parton-parton luminosities are denoted by $d\mathcal{L}^{ij}/d\tau$ $(i,j = g,q,\bar{q})$. which is defined as

$$\begin{aligned}
\frac{d\mathcal{L}^{gg}}{d\tau} &= \int_\tau^1 \frac{dx}{x}\Big[g(x,\mu_F)g\left(\frac{\tau}{x},\mu_F\right)\Big], \\
\frac{d\mathcal{L}^{gq}}{d\tau} &= \sum_{q,\bar{q}}\int_\tau^1 \frac{dx}{x}\Big[g(x,\mu_F)q\left(\frac{\tau}{x},\mu_F\right)+q(x,\mu_F)g\left(\frac{\tau}{x},\mu_F\right)\Big], \\
\frac{d\mathcal{L}^{q\bar{q}}}{d\tau} &= \sum_{q}\int_\tau^1 \frac{dx}{x}\Big[q(x,\mu_F)\bar{q}\left(\frac{\tau}{x},\mu_F\right)+\bar{q}(x,\mu_F)q\left(\frac{\tau}{x},\mu_F\right)\Big],
\end{aligned} \tag{4.14}$$

where $q(x,\mu_F)$ and $g(x,\mu_F)$ are the quark and gluon densities at the factorization scale μ_F. Typical virtual corrections shown in Figure 4 involves two-loop diagrams, which reduce the overall cross-section by about 11% [107], is not supported by `MG5_aMC@NLO`. Therefore we skip the virtual corrections in our calculations and use the equation below to reclaim full NLO results

$$\sigma^{NLO} \approx \sigma^{NLO}_{w/o\ virt} \times \sigma^{LO}_{FT}/\sigma^{LO}_{HEFT}, \tag{4.15}$$

where σ^{LO}_{FT} is leading-order full theory calculation with virtual corrections and σ^{LO}_{HEFT} is leading-order cross-section approximation based on the Higgs-gluon effective field theory without virtual corrections.

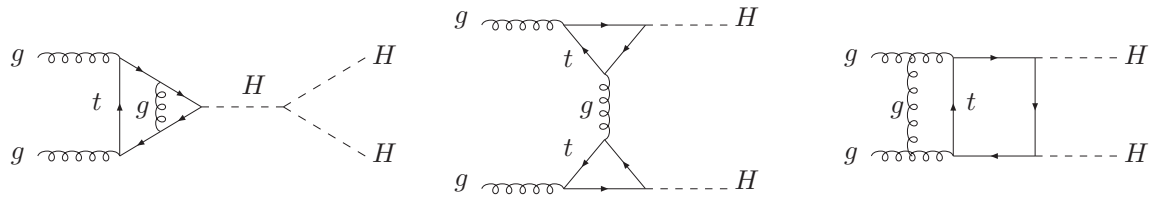

Figure 4. *Examples of typical virtual diagrams contributing to Higgs-pair production at NLO.*

4.2.1 $g\ g \to H\ H\ g$

Figure 5 to Figure 7 show the generic diagrams for $gg \to HHg$ channel. For diagrams shown in Figure 5, Figure 6 (a), and Figure 6 (b), the matrix elements can be easily obtained by replacing one on-shell gluon, ϵ_ν, with a gluon propagator and attaching the other end to a tri-gluon vertex in Equation 4.4. The generic amplitude for these contributions can be written as

$$\begin{aligned}\mathcal{M}(g_1^{c_1} g_2^{c_2} \to HHg_3^{c_3}) &= -\frac{G_F \alpha_s(\mu_R) Q^2}{2\sqrt{2}\pi} \sum_{i,j,k} f^{c_i,c_j,c_k} \mathcal{A}^{\rho\alpha} \epsilon_{i\mu} \epsilon_{j\nu} \epsilon_{k\alpha} \frac{4\pi\alpha_s}{(p_i+p_j)^2} \\ &\quad \times [g_{\mu\nu}(p_i - p_j)^\rho + g_{\nu\rho}(2p_j + p_i)^\mu - g_{\rho\mu}(2p_i + p_j)^\mu], \quad (4.16)\end{aligned}$$

where gluons are labeled by $i, j, k \in 1, 2, 3$, c_i, p_i denotes the color index and the momentum of gluon labeled by i respectively and $\mathcal{A}^{\rho\alpha}$ is defined in Equation 4.4.

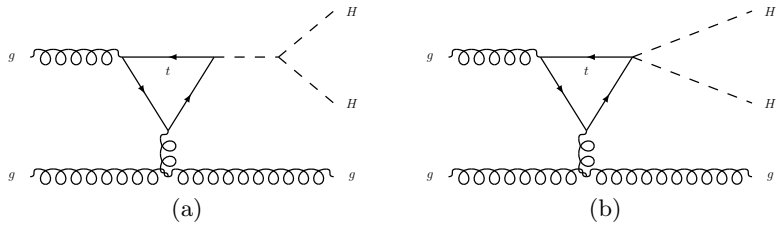

Figure 5. *Generic triangle diagrams for the partonic $gg \to HHg$ channel at NLO in QCD. Diagram* (a) *is SM diagrams, where* (b) *is BSM diagram with anomalous $HHtt$ coupling. Each gluon can be one of the two incoming gluons or the outgoing gluon.*

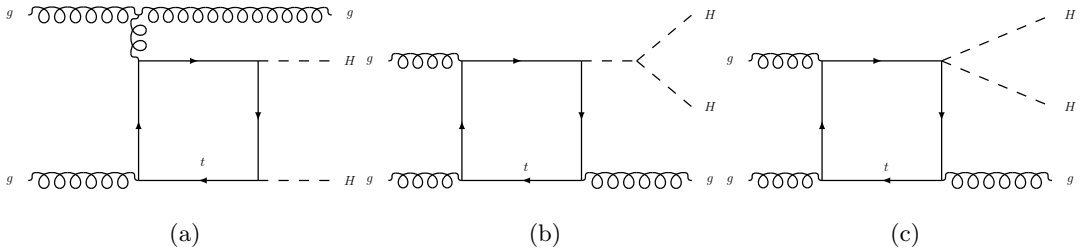

Figure 6. *Generic box diagrams for the partonic $gg \to HHg$ channel at NLO in QCD. Diagrams* (a) *and* (b) *are SM diagrams, where* (c) *is BSM diagram with anomalous $HHtt$ coupling. Each gluon can be one of the two incoming gluons or the outgoing gluon.*

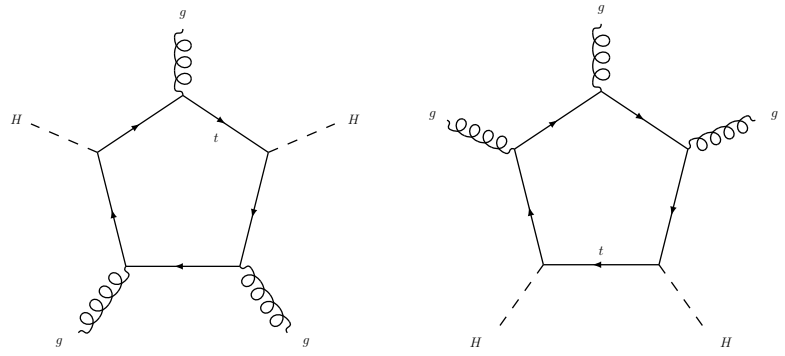

(a) (b)

Figure 7. *Generic SM one-loop pentagon diagrams for the partonic $gg \to HHg$ channel at NLO in QCD. Each gluon can be one of the two incoming gluons or the outgoing gluon.*

4.2.2 $q\ g \to H\ H\ q$ and $q\ \bar{q} \to H\ H\ g$

Although the contributions from $qg \to HHq$ and $q\bar{q} \to HHg$ are very different, as we will see in the next section, they share the same diagrams. Therefore, we only need to compute the matrix elements for $qg \to HHq$ which can be easily converted to corresponding matrix elements for $qg \to HHq$. For contributions shown in Figure 8, similar to the process $gg \to HHg$, the matrix elements can be easily obtained by replacing the only incoming gluon, ϵ_ν, with a gluon propagator and attaching the other end to two fermions in Equation 4.4. The amplitude for contributions shown in Figure 8 can be written as

$$\mathcal{M}(q(p_1)g(p_2) \to q(p_3)HH) = -\frac{G_F \alpha_s(\mu_R) Q^2}{2\sqrt{2}\pi} \mathcal{A}^{\mu\nu} \epsilon_\mu \bar{v}(p_3) \gamma_\nu u(p_1) \frac{\sqrt{4\pi\alpha_s}}{(p_3 - p_1)^3}, \quad (4.17)$$

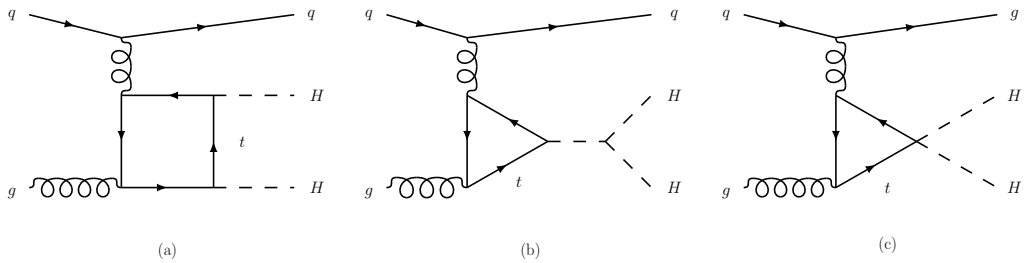

Figure 8. *Dominant one-loop box and triangle diagrams for the partonic channels* $qg \to HHq$.

Other than the common one-loop diagrams shown in Figure 8. We also calculate the contributions from diagrams with only one strong coupling, which has not been studied before. We denote contributions from loop diagrams with more than one strong couplings as QCD_2 contribution and contributions from diagrams with only one strong coupling as QCD_1 contribution. As we will see in the next chapter, QCD_1 contribution is smaller compare to QCD_2 contribution due to the suppression from the weak coupling. For the production processes, $qg \to HHq$, tree-level diagrams are generally too small due to the smallness of the qqH coupling. Therefore, tree diagrams are usually dropped, and only the loop diagrams are considered. However, it turns out that we still have to consider tree diagram for $b(c)g \to b(c)HH$ shown in Figure 9 since the contributions from loop diagrams are small and the bbH or ccH couplings are just large enough to make these tree diagrams contribute at similar order to loop-induced QCD_1 contributions.

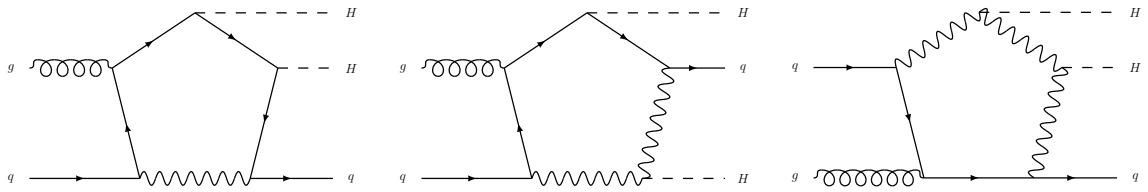

Figure 10. *Generic pentagon diagrams with different numbers of quarks and gauge bosons in the loop.*

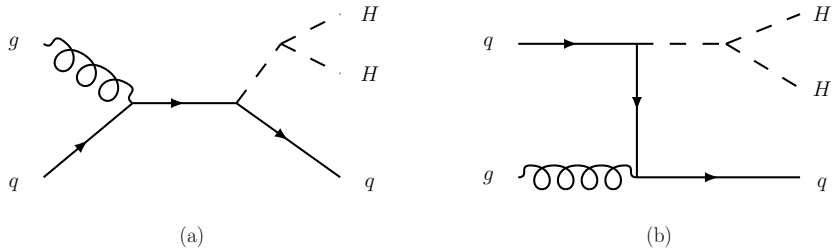

Figure 9. *Tree diagrams for* $b(c)g \to b(c)HH$.

Again all diagrams to one loop level for $qg \to HHq$ can be categorized into the pentagon, box, and triangle diagrams. The pentagon, box, triangle diagrams are shown in Figure 10 to Figure 12 , where solid lines and the wavy represent fermions and vector bosons (W, Z) or corresponding Goldstone boson($G^{+/-}$, G_0), respectively.

For contributions from $gg \to HHg$ and $qg \to HHq$, we generate the full analytical one-loop matrix elements by using `FeynArts` [108] and `FormCalc` [109]. The tensor reduction performed by `FormCalc` is using the techniques developed in [89, 82, 83, 84], while the numerical results of

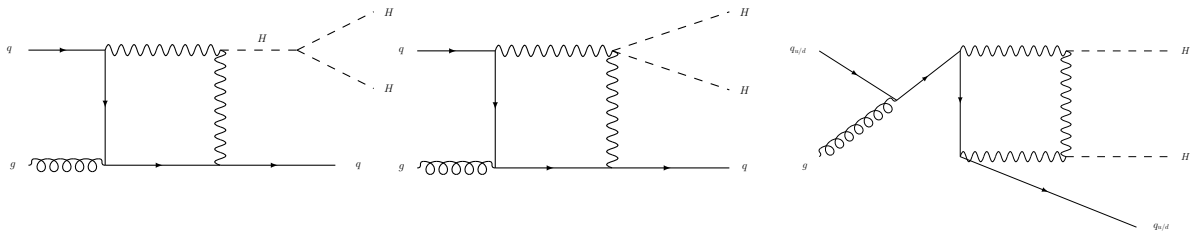

Figure 11. *Generic box diagrams with different numbers of quarks and gauge bosons in the loop.*

the scalar integrals [79] are evaluated with `LoopTools` [109]. As cross-check, the analytic matrix elements for pentagon diagrams with two quark propagators in the loop, box diagrams with one quark propagator, and triangle diagrams are also calculated by hand. The results of matrix elements compute by hand, and matrix elements generated with `FeynArts` and `FormCalc` are in agreement with the numerical results generated by `MG5_aMC@NLO` [110], which is the primary tool for the computations of cross-sections and the generation of hard events in this article.

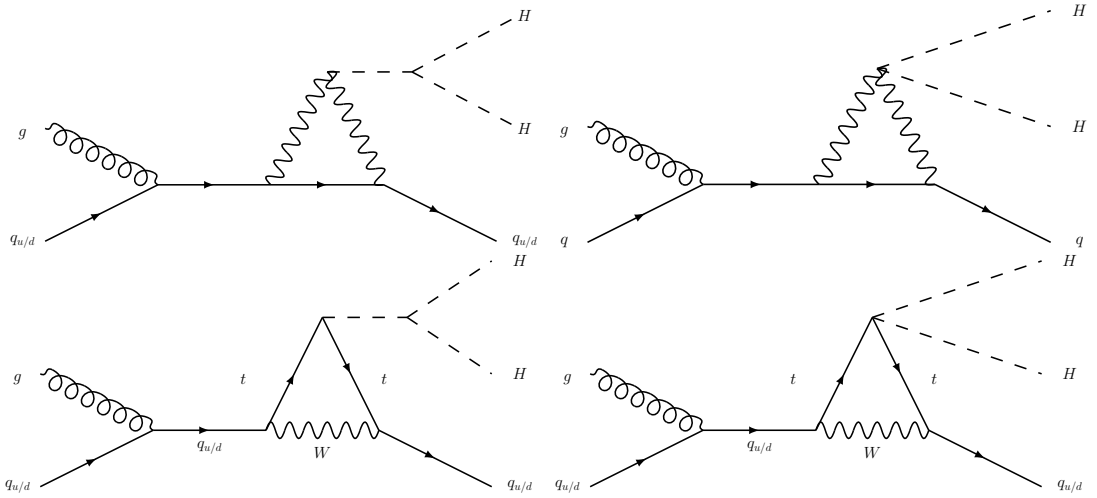

Figure 12. *Generic triangle diagrams with different numbers of quarks and gauge bosons in the loop.*

CHAPTER 5

NUMERICAL ANALYSIS

We use the same workflow introduced in Section 5.1.1, and adopt only `PDF4LHC15` [111] to generate partonic events. For hadron level analysis, we feed the unweighted partonic events file into Pythia 8 [112] to generate a large number of simulated collision events. To promptly analyze such a huge amount of simulated collision events, we adopt Delphes [113], which provides a fast multipurpose detector response simulation to reconstruct events into jets such as b jet and lepton jets, etc. All parameters are kept the same as what we use in Equation 5.3, and renormalization scale μ_R and factorization scale μ_F both equal to m_{HH}.

We analyzed the final results in detail for the total cross-section and the differential cross-section in the invariant mass of Higgs-pair.

5.1 Kinematic Distributions

For the double Higgs production with at most one extra jet, $pp \to HHj$, the SM expectation for this production cross-section is only 0.031 pb in the Large Hadron Collider with CM energy at 14 TeV. At the potential 100 TeV hadron collider, the expected SM cross-section increases significantly to 1.543 pb since the luminosity of gluon PDF at lower Bjorken scale, increases.

By convoluting the gluon and quark PDF's with the partonic cross-section in a hadron collider, we can obtain the differential cross-section in the lab frame

$$\frac{d^2\sigma(pp \to HH)}{dm_{HH}\, dp_T} = \int_\tau^1 \frac{dx}{x} g(x, \mu_F) g\left(\frac{\tau}{x}, \mu_F\right) \frac{2m_{HH}}{s} \frac{d\hat{\sigma}(gg \to HH)}{dp_T} \ , \tag{5.1}$$

where p_T is the transverse momentum of the Higgs boson, s is the CM energy of head-on hadrons, and $\tau = \hat{s}/s$, $m_{HH} = \sqrt{\hat{s}}$,

$$p_T^2 = \frac{\hat{u}\hat{t} - m_H^4}{\hat{s}} \ . \tag{5.2}$$

In this section, we firstly adopt `MG5_aMC@NLO` [110] with a custom UFO model [114] including the anomalous Higgs-top coupling, $HHtt$, and corresponding R_2 and UV counterterms to generate matrix elements. We then adopt two different PDF sets, `PDF4LHC15` [111] and MSTW 2008 LO 4F [115], to generate partonic events. In this work, we draw all plots by using the framework above with the following parameters

$$m_t = 173\text{GeV} \ , \quad m_H = 125\text{GeV}. \tag{5.3}$$

The input value $\alpha_s(M_Z)$ is determined by the PDF set used, where $\alpha_s(M_Z) = 0.118$ for `PDF4LHC15` and $\alpha_s(M_Z) = 0.13355$ for MSTW 2008 LO 4F. We set the factorization and renormalization scales to $\mu_F = \mu_R = m_{HH}$.

5.1.1 Leading-order Contribution

In Figure 13 we show the leading-order distributions of m_{HH} and p_T for the Standard Model $gg \to HH$ process in a proton-proton collider at CM energies of 14 and 100 TeV. We can see that the general shapes are insensitive to the CM energy of the pp collider for these kinematic distributions. The kinematic distributions peak at $m_{HH} \sim 420$ GeV for the invariant mass of the Higgs pair, and $p_T \sim 150$ GeV for the transverse momentum of the single Higgs boson. The numerical results obtained using MSTW 2008 LO 4F are identical to the results in [103].

The invariant mass of most events is remote above $2m_H$, the kinematic threshold of two outgoing Higgs bosons. Therefore, the low-energy Higgs theorem is invalid for $gg \to HH$, as mentioned at the end of Section 4.1. The contribution from c_{3H} rises significantly as $m_{HH} \sim 2m_H$ since the coefficient of the loop function $F_\triangle$ is

$$c_{3H} \frac{3m_H^2}{\hat{s} - m_H^2} + c_{HHtt} \,. \tag{5.4}$$

As a result, c_{HHtt} could become dominant over c_{3H} at large m_{HH}. Unfortunately, the total cross-section contribution from c_{3H} will be suppressed since most of the events have $m_{HH} \gg 2m_H$, which was concluded in [62]. Therefore, it will be very difficult to measure a truly model-independent Higgs trilinear coupling solely from the total cross-section of double Higgs

production. In Figure 14 and Table I we show the individual contribution from Triangle, Box and HHtt, defined in Equation 5.6, and compare them with the SM expectation.

$$\begin{aligned} \text{Triangle} &: c_{3H} = 1, c_{Htt} = 0, c_{HHtt} = 0 \\ \text{Box} &: c_{3H} = 0, c_{Htt} = 1, c_{HHtt} = 0 \\ \text{HHtt} &: c_{3H} = 0, c_{Htt} = 0, c_{HHtt} = 1 \end{aligned} \tag{5.5}$$

The total cross-section contribution from the SM diagrams is relatively small when $c_{3H} \sim c_{Htt}$ due to the nature of destructive interference between the triangle and box diagrams, which can be inferred from Figure 14. Consequently, the measurement of c_{3H} would be significantly impacted by turning on a small c_{HHtt}. Although there is a 30% difference in the total cross-section between two PDF sets, the general shapes of the kinematic distributions are not sensitive to the PDF set we use, and we will only show the results with `PDF4LHC15` from now on.

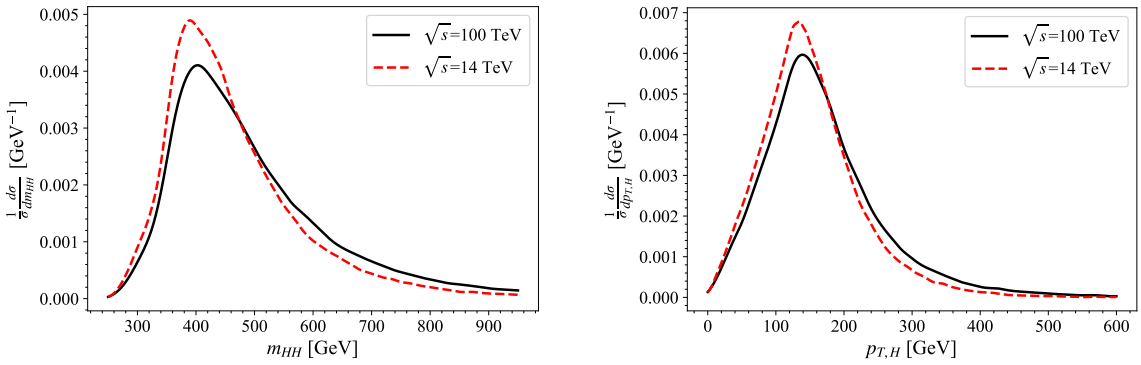

(a) (b)

Figure 13. *The SM expectation of LO m_{HH} and $p_{T,H}$ distributions at $\sqrt{s} = 14$ and 100 TeV.*

σ [pb]	MSTW 2008 LO 4F				PDF4LHC15			
	Total	Triangle	Box	HHtt	Total	Triangle	Box	HHtt
14 TeV	0.01956	0.00567	0.04125	0.04999	0.0167	0.004692	0.0349	0.0424
100 TeV	1.0001	0.2252	1.946	2.800	0.6923	0.146	1.32	1.987

TABLE I

Individual contribution of cross-section from Triangle, Box and HHtt in 14 and 100 TeV hadron colliders.

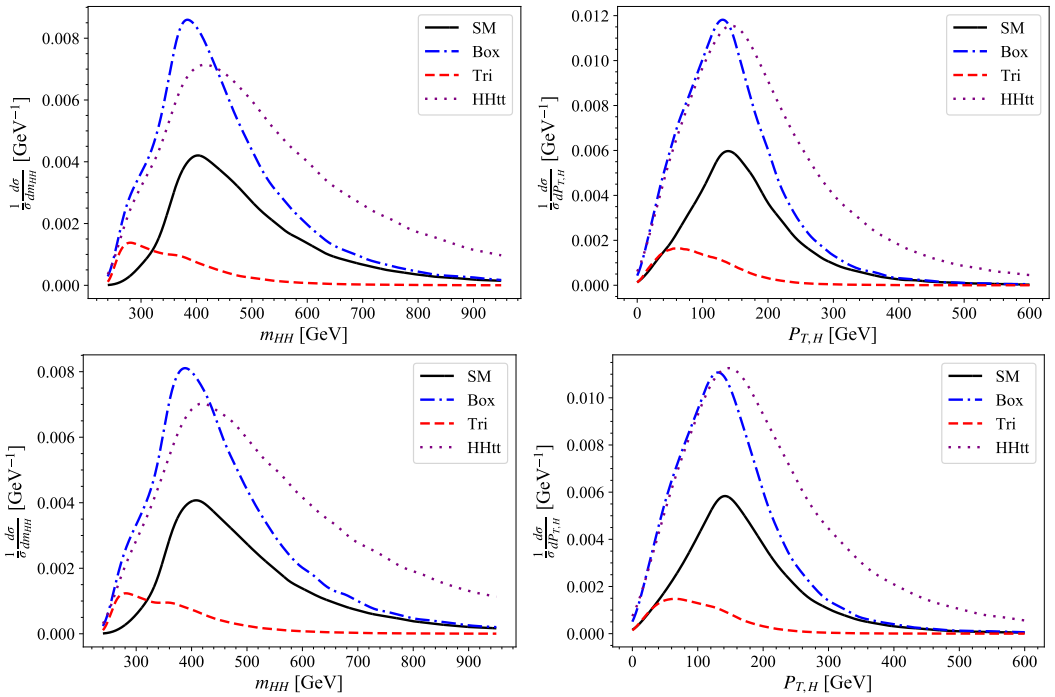

Figure 14. *Individual contribution from Triangle, Box, HHtt to the LO m_{HH} and $p_{T,H}$ distributions in a hadron collider at $\sqrt{s} = 100$ TeV. The results obtained by adopting MSTW 2008 LO 4F are in the upper row while the results obtained by adopting* `PDF4LHC15` *are in the lower row of the figure.*

For p_T spectrum of individual contribution, $G_\Box$ has a strong p_T dependence, and p_T dependence in $F_\Box$ is not as strong as $G_\Box$ while $F_\triangle$ has no p_T dependence. This is because the projection of the angular momentum of head-on gluons with the same helicity on the beam axis is zero, $J_z = 0$, which corresponds to $F_\triangle$ and $F_\Box$. On the other hand, $G_\Box$ has $J_z = 2$ on the beam axis resulted from opposite helicity gluons [29, 31]. Nevertheless, only the S-wave orbital angular momentum is contained by $F_\triangle$ since only the scalar Higgs couplings are included in Figure 3(a) and Figure 3(c). In other words, $F_\triangle$ is p_T independent. Therefore, the phase space

is the only source of all the p_T dependence in the c_{3H} and c_{HHtt}. However, the higher-order terms of $\hat{s}/m_t^2$ expansion for the $J_z = 0$ component of the D-wave angular dependence leave some p_T dependence for $F_\square$ [105]. $G_\square$ has a strong p_T dependence due to the D-wave nature. Furthermore, the difference of the angular momentum projection between $F_\triangle/F_\square$, and $G_\square$ also explains the lack of interference between the two contributions in (Equation 4.7). In Figure 14 we also show the p_T spectrum of individual contribution from Triangle, Box and HHtt. The contribution from Triangle are suppressed in general, as in the m_{HH} distribution since the Higgs propagator in Figure 3(b) is off-shell.

5.1.2 $g\ g \to H\ H\ g$ Contribution

Numerical calculations of $gg \to HHg$ are performed in 14 and 100 TeV hadron colliders. The standard model (SM) expectation of the cross-section at a 14 TeV pp collider for this channel is 0.014 pb. At 100 TeV, the SM rate rises significantly to 0.85 pb. The contribution of the double Higgs production from $gg \to HHg$ is comparable to LO $gg \to HH$, 0.0167 pb and 0.692 pb at 14 and 100 TeV, respectively, and consists half the total production rate.

In Figure 15, we present the SM m_{HH} and p_T distributions for $gg \to HHg$ in 14 and 100 TeV hadron colliders. Since the dominant contributions come from one loop triangle and box diagrams shown in Figure 5 and Figure 6, repectively, which has the same loop function as $gg \to HH$ channel. We therefore expect the general shapes of kinematic distributions shown in Figure 17 are insensitive to the center-of-mass energy of the hadron collider and share some similarity to Figure 13. Indeed, comparing to LO counterpart, the general shapes are very similar except they are wider.

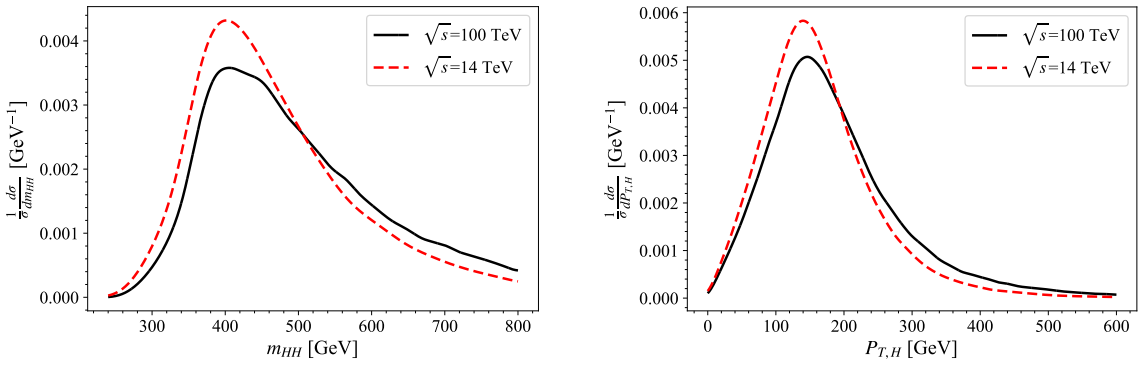

(a) (b)

Figure 15. *Kinematic distributions for $gg \to HHg$ in the SM at $\sqrt{s} = 14$ and 100 TeV.*

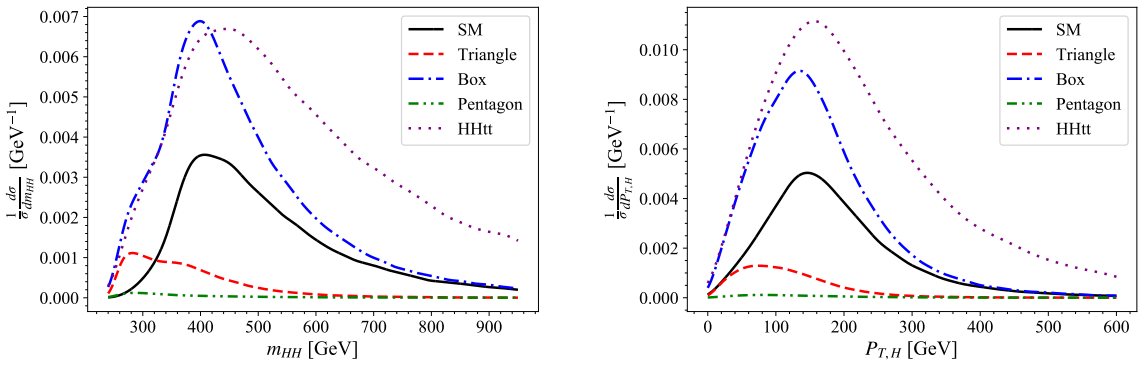

(a) (b)

Figure 16. *Individual contribution from Triangle, Box, Pentagon and HHtt to the kinematic distributions for $gg \to HHg$ in the SM at $\sqrt{s} = 100$ TeV.*

The invariant mass distribution peaks at slightly lower $m_{HH} \sim 380$ GeV, while the maximum of p_T distribution is still at $p_T \sim 150$ GeV. Unlike the $gg \to HH$ counterpart, we can easily see the peaks in Figure 13 move to the right slightly and get wider as the CM energy of the head-on hadrons increases. There are even more events that have $m_{HH} \gg 2m_H$. Hence the contribution to the total cross-section from c_{3H} will be further suppressed as we already discussed in Section 5.1.1.

In Figure 16 we show the individual contribution of $gg \to HHg$ channel from Triangle, Box, Pentagon, and HHtt diagrams, shown in Figure 5 to Figure 7 , in the m_{HH} and P_T distribution while comparing them with the SM expectation. Triangle, box, pentagon contributions come from SM diagrams, while HHtt is the contribution from diagrams with anomalous $HHtt$ coupling. As we can see, $gg \to HHg$ have similar kinematic distributions and similar reactions to the parameters, c_{3H}, c_{Htt} and c_{HHtt}, due to the same loop function in Equation 4.7. The c_{3H} contribution to the total cross-section is still suppressed when $c_{3H} \sim c_{HHtt}$, and c_{HHtt} would have a significant impact on the cross-section of $gg \to HHg$ process as we saw in the LO case.

5.1.3 $q\ g \to H\ H\ q$ Contribution

Again we perform numerical simulation for $qg \to HHq$ in 14 and 100 TeV hadron colliders.

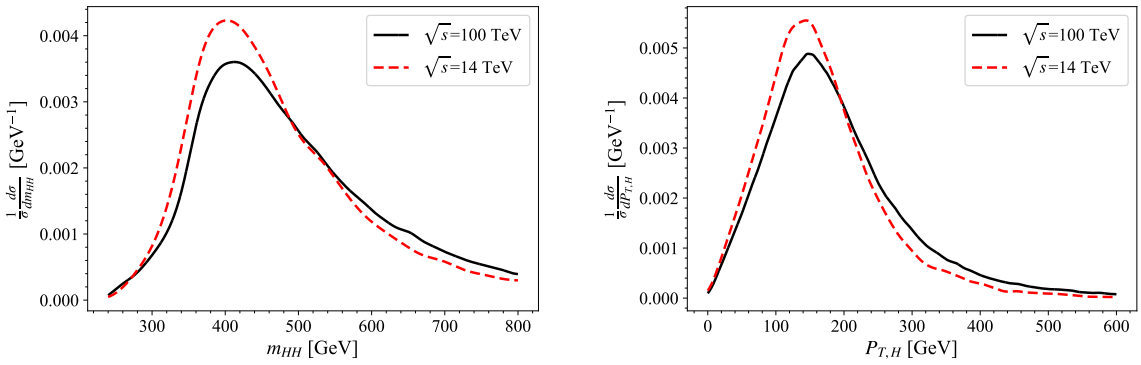

(a) (b)

Figure 17. *Kinematic distributions for $qg \to HHq$ in the SM at $\sqrt{s} = 14$ and 100 TeV.*

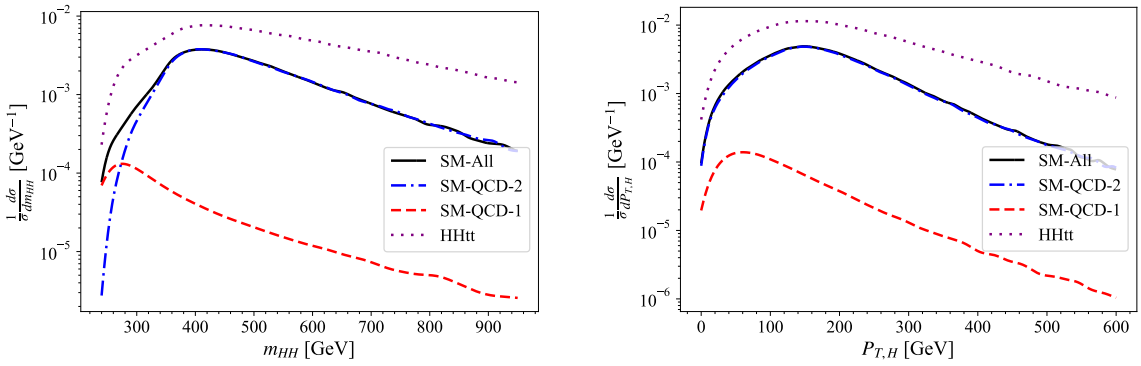

(a) (b)

Figure 18. *Individual contribution from QCD_1, QCD_2, $HHtt$ to the kinematic distributions for $qg \to HHq$ in the SM at $\sqrt{s} = 100$ TeV.*

In Figure 17, we show the kinematic distributions, including m_{HH} and p_T, for SM $qg \to HHq$ in the hadron collider at CM energies 14 and 100 TeV. Since the dominant contributions come from one loop triangle and box diagrams shown in Figure 8, which has the same loop function as $gg \to HH$, we expect Figure 17 to share some similarity to Figure 13. Comparing to $gg \to HH$ counterpart, the general shapes are very similar except they are wider. The maximum for invariant mass and p_T distributions are still the same, $m_{HH} \sim 420$ GeV and $p_T \sim 150$ GeV, respectively. For most events, the invariant mass is far above the threshold, $2m_H$ as we already discussed in Section 5.1.1. Unlike $gg \to HH$ counterpart, we can easily see the peaks in Figure 13 move to the right slightly and get wider as the CM energy of the hadron collider increases. This means even more events have $m_{HH} \gg 2m_H$.

Figure 18 shows the individual contribution of $qg \to HHq$ from QCD_2, QCD_1, and $HHtt$ in the m_{HH} and P_T distribution while comparing these contributions with the SM expectation. QCD_2 is the contribution from diagrams with more than one gluon coupling as shown in Figure 8. QCD_1 contribution includes all the rest of SM diagrams for $qg \to HHq$, including tree, triangle, box, and pentagon diagrams, while $HHtt$ contribution comes from diagrams with an $HHtt$ coupling. As we can see, QCD_2 is the dominant contribution of $qg \to HHq$ since weak couplings suppress QCD_1 contributions. Again we can expect $gg \to HH$, $qg \to HHq$ have similar kinematic distributions and similar reactions to the parameters, c_{3H}, c_{Htt} and c_{HHtt}, due to the same loop function in Equation 4.7. We find the CM energy insensitivity of the general shapes of these distributions. Therefore, in what follows, we only present the result for $\sqrt{s} = 100$ TeV. As we saw in the $gg \to HH$ channel, the contribution from diagrams that in-

volve the trilinear Higgs is still suppressed when $c_{3H} \sim c_{HHtt}$, and c_{HHtt} would have significant effects on the cross-section of $qg \to HHq$ process.

For QCD_1 contribution, more events have lower invariant mass, m_{HH}, and transverse momentum, p_T. The peak of invariant mass distribution is at $m_{HH} \sim 280$ GeV, while the maximum of p_T distribution is at $p_T \sim 60$ GeV. Hence, the QCD_1 contribution at small invariant mass, $m_{HH} \sim 2m_H$, is more important than the QCD_2 contribution, which is dominant at large m_{HH}.

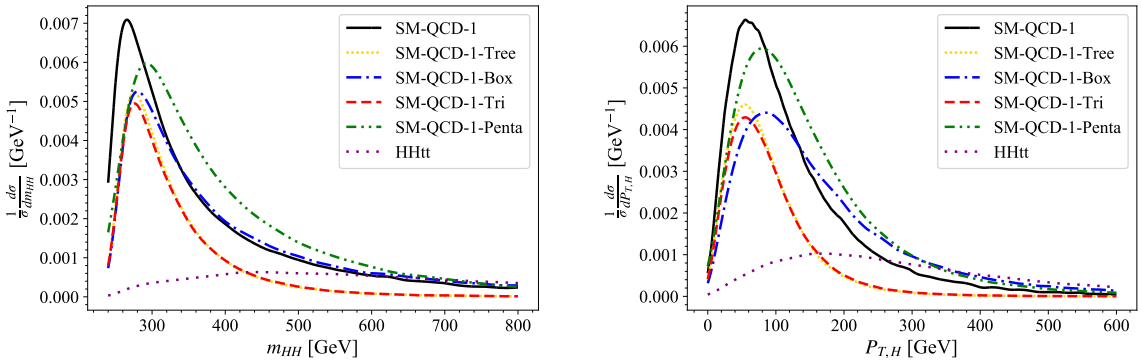

(a) (b)

Figure 19. *Individual QCD_1 contribution from tree, triangle, box, pentagon diagrams to the kinematic distributions for $qg \to HHq$ in the SM at $\sqrt{s} = 100$ TeV.*

In Figure 19, for completeness, we further divide the QCD_1 contribution into the individual contribution from the tree, triangle, box, pentagon, and $HHtt$ contributions from corresponding

diagrams and compare them with the total QCD_1 contribution. We can categorize individual contributions shown in Figure 19 into two groups. Group one consists of tree and box diagrams, while group two consists of the triangle and pentagon diagrams. As a result, the interference between the contribution from group one and group two is destructive, which can also be inferred from Figure 19. The $HHtt$ contribution when $c_{HHtt} = 1$ comes from diagrams with only one gluon coupling, as shown in Figure 11 and Figure 12 is very small compared to the QCD_1 contribution, which is already small. However, the $HHtt$ contribution shown in Figure 18 is dominant over SM value. Therefore, most of $HHtt$ contribution to $qg \to HHq$ channel comes from diagrams shown in Figure 8.

5.1.4 NLO

In Figure 20, we show the individual SM contributions from all processes up to NLO, including $gg \to HH$, $gg \to HHg$, $qg \to HHq$ and $qq \to HHg$, while comparing them with the total NLO SM contributions in the m_{HH} and P_T distribution.

We can see that $gg \to HH$ and $gg \to HHg$ contributions are equivalently dominant while $qg \to HHq$ only contributes about 10% of the total cross-section. Similar kinematic distributions to $gg \to HH$ contribution are found in $gg \to HHg$ and $qg \to HHq$ contributions. We can therefore expect the full NLO contribution have similar kinematic distributions and similar reactions to the parameters. As expected, The peaks of invariant mass and p_T are still at $m_{HH} \sim 420$ GeV and $p_T \sim 150$ GeV, respectively.

The parameters we previously used, c_{3H}, c_{Htt} and c_{HHtt}, have to be generalized since the contributions from diagrams such as Figure 11 do not have HHH, Htt, or $HHtt$ couplings. By

following the same idea, we can create a new parameter set based on all Higgs couplings c_{3H}, c_{Htt}, c_{HHtt}, c_{HWW}, c_{HZZ}, $c_{HZZ,Htt}$, and $c_{Hbb(cc)}$ such that

$$\begin{aligned}\mathcal{M} &= c_{3H}\mathcal{M}_{3H} + c_{Htt}\mathcal{M}_{Htt} + c_{Htt}\mathcal{M}_{HHtt} + c_{HWW}\mathcal{M}_{HWW} \\ &\quad + c_{HZZ}\mathcal{M}_{HZZ} + c_{HZZ,Htt}\mathcal{M}_{HZZ,Htt} + c_{Hbb(cc)}\mathcal{M}_{Hbb(cc)}, \end{aligned} \tag{5.6}$$

where

$$\begin{aligned} c_{3H} &= g_{H^3} g_{Htt} \frac{v^2}{3m_H^2 m_t}, \quad c_{HHtt} = g_{HHtt}\frac{v^2}{m_t}, \quad c_{Htt} = \left(g_{Htt}\frac{v}{m_t}\right)^2 \\ c_{Hbb(cc)} &= \left(g_{Hbb(cc)}\frac{v}{m_b}\right)^2, \quad c_{HWW} = \left(g_{HWW}\frac{v}{2m_W^2}\right)^2, \quad c_{HZZ} = \left(g_{HZZ}\frac{v}{2m_Z^2}\right)^2 \\ c_{HWW,Htt} &= \left(g_{HWW} g_{Htt}\frac{v^2}{2m_W^2 m_t}\right)^2. \end{aligned}$$

$\mathcal{M}_x$ is amplitude of diagrams with coupling x while $\mathcal{M}_{HWW,Htt}/\mathcal{M}_{HZZ,Htt}$ is amplitude of diagram with HWW/HZZ and Htt couplings. If we adopt this new set of parameters into $gg \to HH$ channel, we can see that

$$c_{3H} = c_{3H}, \quad c_{Htt} = c_{Htt} \text{ and } c_{HHtt} = c_{HHtt}. \tag{5.7}$$

Figure 21 shows the individual contribution from c_{3H}, c_{Htt}, c_{HHtt}, and the distribution of SM expectation in the m_{HH} and $p_{T,H}$ distribution. The Higgs low-energy theorem breaks down since most events have an invariant mass much higher than the kinematic threshold at $2m_H$ as discussed at the end of Section 4.1. We note that c_{HHtt} is even more dominant over c_{3H} at

large m_{HH} in Figure 20 compare to $gg \to HH$ counterpart shown in Figure 14. Turning on a small c_{HHtt} would significantly impact the measurement of c_{3H} when $c_{3H} \sim c_{Htt}$ since the contribution from the Higgs trilinear coupling to the total cross-section is relatively small, and the destructive interference between the box and triangle diagrams. These facts make a truly model-independent Higgs trilinear coupling measurement from the total rate of the Higgs pair production challenging since most of the events have $m_{HH} \gg 2m_H$, the contribution of the total cross-section from c_{3H} will be suppressed.

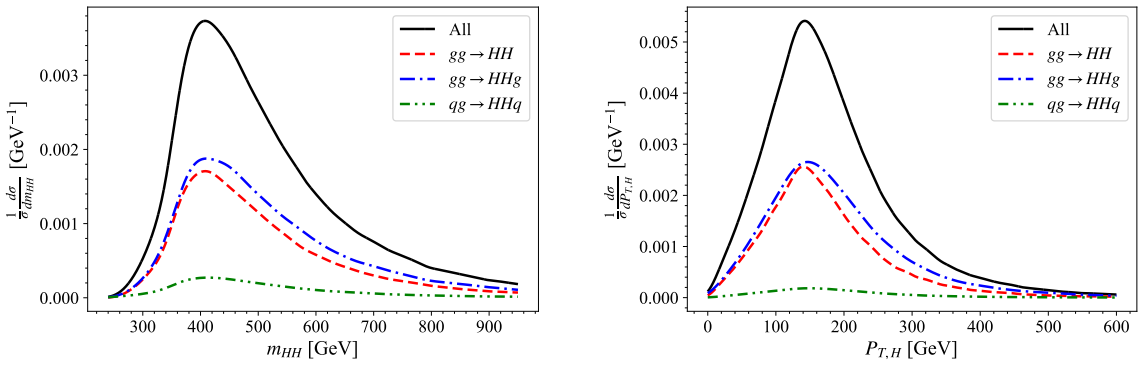

(a) (b)

Figure 20. *Individual contribution from $gg \to HH$, $gg \to HHg$, $qg \to HHq$ to the kinematic distributions for double Higgs production in the SM at $\sqrt{s} = 100$ TeV.*

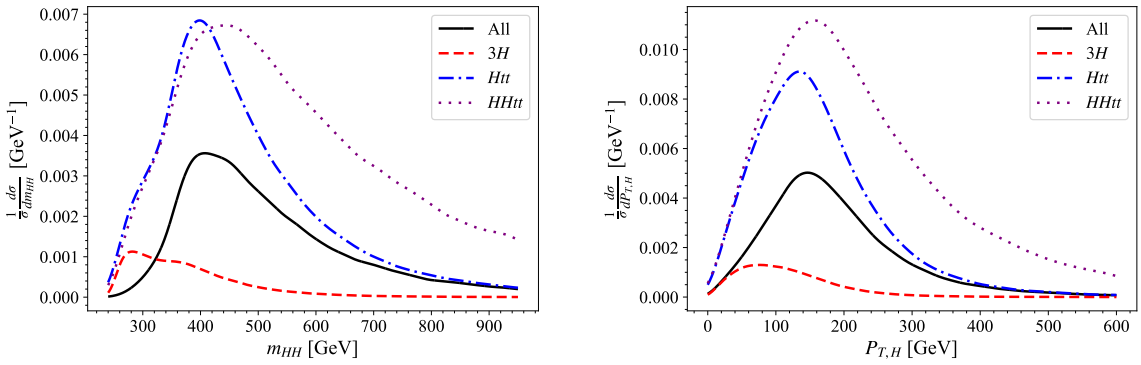

(a) (b)

Figure 21. *Individual contribution from c_{3H}, c_{Htt} and c_{HHtt} to the kinematic distributions for double Higgs production at $\sqrt{s} = 100$ TeV.*

5.2 The $b\bar{b}\gamma\gamma$ Decay Channel

In this section e investigate $HH \to b\bar{b}\gamma\gamma$ channel, which is the process that has the highest signal significance and in SM has the most sensitivity to the trilinear Higgs self-coupling as pointed out in the literature. Earlier studies can be found in [116, 117, 118, 119, 26]. Recent searches [120] for pairs of Higgs bosons in $HH \to \gamma\gamma b\bar{b}$ process have narrowed the upper bound of the Higgs pair production rate down to 4.1 times the SM expectation, created a portal of better understanding into the fundamental Higgs mechanism. We perform the partonic event generation for the signal and backgrounds by using `MadGraph5_aMC@NLO` with the parton density functions `PDF4LHC15` [111]. We include the effects of full NLO corrections for the signal,

$H(b\bar{b})H(\gamma\gamma)$. The background signal is generated at LO with the finite-top-mass effects and rescaled by a K-factor afterward (See Table Table II).

We include the following major backgrounds in the analysis: the resonant processes , $t\bar{t}\gamma\gamma$ and $t\bar{t}H(\gamma\gamma)$ with $t \to bW$ subdecay , as well as $b\bar{b}H(\gamma\gamma)$ and $Z(b\bar{b})H$, and the non-resonant processes $b\bar{b}\gamma\gamma$, $b\bar{b}j\gamma$ (with one fake photon), $bj\gamma\gamma$, $jj\gamma\gamma$ (with one and two fake b-jets). The $b\bar{b}jj$ background is not included since it is negligible compared to other faked backgrounds after selection cuts. The MLM matching is applied to all background processes with at most one extra parton to avoid double-counting.

We generate events with exclusive cuts for signal and background processes. In what follows, the acceptance cuts are applied to each final state for each plot. Here is the detailed event selection: We require exactly two b quarks and two photons in the final state with the following cuts $p_{T,b} > 30$ GeV, $|\eta_b| < 2.5$ and $\Delta R(b,b) > 0.4$, where the distance is defined as $\Delta R = \sqrt{(\Delta\eta)^2 + (\Delta\phi)^2}$. For leptons, the allowed soft transverse momentum and the allowed pseudorapidity are set to $p_{T,\ell} > 20$ GeV and $|\eta_\ell| < 2.5$, respectively, to diminish the $t\bar{t}H$ background. Moreover, the select events are selected to satisfy $|\eta_{jet}| < 2.5$ and $p_{T,jet} > 20$ GeV for QCD jets to diminish the $t\bar{t}H$ background further. The two photons has to fulfill $\Delta R(\gamma,\gamma) > 0.4$, $|\eta_\gamma| < 2.5$, and$p_{T,\gamma} > 30$ GeV. To reconstruct the Higgs bosons, the allowed invariant masses are within a range of 25 GeV, 112.5 GeV $< M_{b\bar{b}} <$ 137.5 GeV for the b quark pair, and a smaller range of 10 GeV, 120 GeV $< M_{\gamma\gamma} <$ 130 GeV for the photon pair. In addition, we induce $\Delta R(\gamma, b) > 0.4$ to isolate the b quarks with the photons.

Besides the acceptance cuts shown above, more advanced cuts have been applied based on the distributions shown in Figure 22 for the parton-level analysis. First, we select the events with a reconstructed invariant mass of the Higgs pair that satisfy $m_{HH} > 300$ GeV. Moreover, we select events that satisfy $P_{T,H} > 100$ GeV. We also require $\Delta R(b,b) < 2.5$ to divide the two b jet and require the reconstructed Higgs boson to have the pseudorapidity $|\eta_H| < 2$.

For the $b\bar{b}\gamma\gamma$ final state, a realistic estimation of the diphoton fake rate is the most important factor of an accurate assessment for measuring the signal since the production of multijet, which is the dominant background in this case, give rise to this fake rate.

To gain more reliable results and verify if any promising feature can be found in real experiments, we include showering and hadronization effects by using the `Pythia 8`[112] package [112] for the signal and background samples. Detector simulation effects based on the current performance of ATLAS and CMS are included by using the `Delphes` [113] package. We follow the parameter settings and the cut selections in [61]. We chose the operation points of b-tagging to have 18.8%, 75%, and 1% for charm, bottom, and light quark jets in the central region, $|\eta| < 2.5$ and $P_{T,j} > 50\,\text{GeV}$, respectively. The photon identification efficiency is about 80% for photons with $P_{T,\gamma} > 50\,\text{GeV}$ and $|\eta| < 2.5$. For the background with fake photons from misidentified jets, we assign a mistag rate of $f_j = 0.0093\exp(-P_T/27)$ as a function of P_T in GeV of the jet with the fake photon energy equal to the jet energy scaled by 0.75 ± 0.12 [121]. At $M_h = 125\,\text{GeV}$, the mass resolution is 17 GeV for $h \to b\bar{b}$ and 2 GeV for $h \to \gamma\gamma$. In order to be consistent with the signal, the isolated photon pair and two tagged b-jets in the final states are selected to satisfy $P_T > 25\,\text{GeV}$ and $|\eta| < 2.5$.

$\sqrt{s}$ [TeV]	HH	$b\bar{b}\gamma\gamma$	$t\bar{t}H$	ZH	$b\bar{b}H$	$\gamma\gamma jj$	$b\bar{b}j\gamma$
100	1	1.0	1.3	1.2	0.87	1.43	1.08

TABLE II

K–factors for ZH, $b\bar{b}\gamma\gamma$ and $t\bar{t}H$ production at $\sqrt{s} = 100$ TeV [1].

Observables	Acceptance cuts
Total number n of jets (j, γ, l)	$n < 7$ in each event
Pseudorapidity	$\eta_{b,\gamma} < 2.5$
Invariant mass	$120 < m_{b\bar{b}} < 130$ GeV, $122 < m_{\gamma\gamma} < 128$ GeV, $m_{b\bar{b}\gamma\gamma} > 300$ GeV
Transverse momentum	$p_{T\gamma,b} > 35$ GeV, $p_{T\gamma\gamma,b\bar{b}} > 100$ GeV
ΔR	$0.4 < \Delta R(b,b) < 2.0$, $0.4 < \Delta R(\gamma,\gamma) < 2.5$

TABLE III

List of observables and acceptance cuts used for the analysis.

The cuts for mass-window are further applied to the invariant-masses of the two photons and two b-jets. For the photon pair, we impose $122\,\text{GeV} < M_{\gamma\gamma} < 128\,\text{GeV}$ on the invariant-mass window. The invariant-mass window for the two b-jets is $120\,\text{GeV} < m_{b\bar{b}} < 130\,\text{GeV}$.

The final value, shown at the bottom of Table IV, is $S/\sqrt{B} = 16.1$ for the integrated luminosity, $\int \mathcal{L} = 3$ ab^{-1}. Therefore this channel seems promising in the future upgrade of the LHC (HE-LHC) or Future-Circular-Collider (FCC).

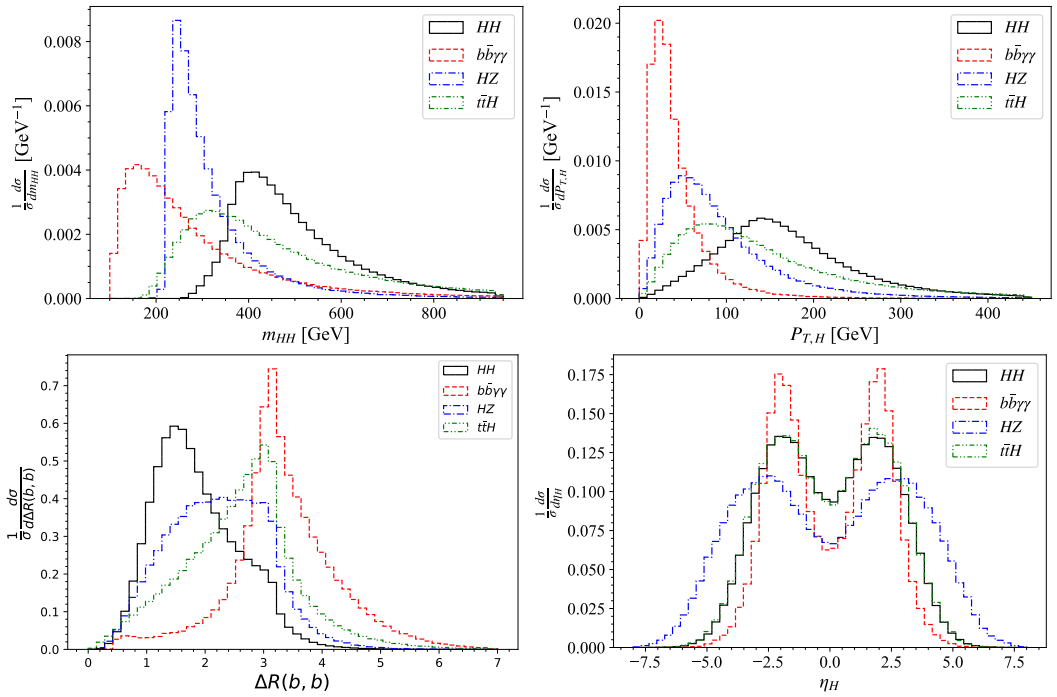

Figure 22. *Normalized signal and backgrounds distributions of $P_{T,H}$, m_{HH}, R_{bb} and η_H in the $b\bar{b}\gamma\gamma$ channel at a $\sqrt{s} = 100$ TeV pp collider.*

5.3 Sensitivity to effective self-couplings of Higgs bosons

In this section, the characteristic distributions of the double Higgs production for several observables are studied with different c_{3H}.

Figure 23, shows the distributions of the invariant mass m_{HH}, the transverse momentum $P_{T,H}$, the pseudorapidity η_H, and the rapidity y_{HH} of the Higgs pair with the area under the SM curve normalized to unity. Each observable distribution is shown for $c_{3H} = 0.5$, 1, 2.5, and -1.

TABLE IV

The table consists of $\sigma \times Br$, acceptance, and the expected events for signal and background processes at a proton-proton collider with CM energy of 100 TeV and integrated luminosity of $3\,ab^{-1}$.

Samples	$\sigma \times$BR (fb)	Accept	Expected
$h(b\bar{b})h(\gamma\gamma)$ (SM)	3.50	0.0403	420 ± 7
$b\bar{b}h(\gamma\gamma)$	51.8	0.00069	107.6 ± 13.4
$Z(b\bar{b})h(\gamma\gamma)$	7.73	0.00082	19.0 ± 0.7
$t\bar{t}h(\gamma\gamma)$	32.0	0.00161	155 ± 14.3
$t\bar{t}\gamma\gamma$	347.4	6.63×10^{-6}	6.88 ± 6.88
$t\bar{t}\gamma$	101176	4.78×10^{-8}	14.5 ± 3.2
$b\bar{b}\gamma\gamma$	5050	1.41×10^{-5}	212 ± 65.6
$b\bar{b}j\gamma$	8840000	4.83×10^{-9}	128 ± 31.9
$jj\gamma\gamma$	171600	6.93×10^{-8}	35.7 ± 2.4
Total background	–	–	677.3 ± 69.0
$S/\sqrt{B}$ $(S/\sqrt{B+S})$	–	–	16.1 (12.5)

As in the $P_{T,H}$ distribution plot of Figure 23 with the distribution max at $P_{T,H} \sim 150$ GeV, The Higgs bosons from the production of inclusive Higgs pair are usually boosted. The pseudorapidity of the Higgs pair shown in the lower left of Figure 23 is low and has a typical symmetric distribution with the maximum close to zero due to the high transverse momentum spectrum. For $c_{3H} = 2.5$, the interferences between the box and the triangle diagrams are destructive. This explains the dip in the $P_{T,H}$ distribution. Comparing to a lower peak value of $M_{ZH} \gtrsim 250$ GeV for the background shown in Figure 22, the peak value is $m_{HH} \gtrsim 420$ GeV

for the signal. Again, this destructive interference also causes a significant depletion in the signal when $c_{3H} = 2.5$. For smaller $c_{3H} = 0.5$, the destructive interference is diminished, and the signal is stronger than the SM expectation value for each distribution. For $c_{3H} = -1$, the differential cross-sections for all observables are enhanced significantly since the box diagram interferes constructively with the triangle diagram when c_{3H} becomes negative. For y_{HH} and η_H distribution, the overall shape is the same for different trilinear Higgs coupling values. We can infer that the y_{HH} distribution is significantly wider for the ZH background than for the signal shown in Figure 22.

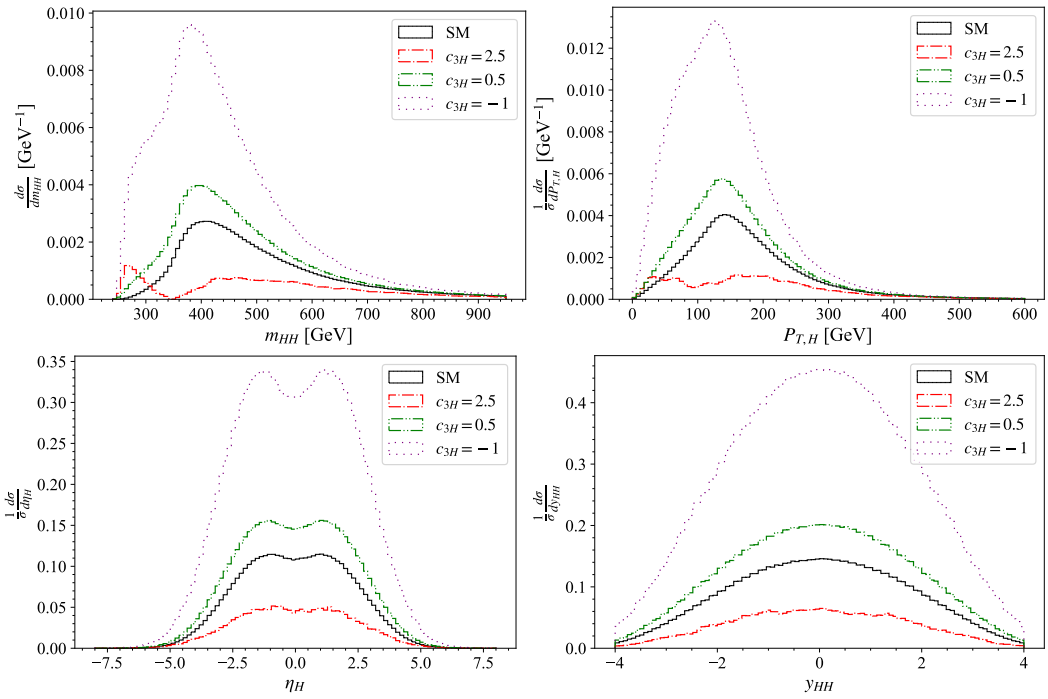

Figure 23. *Distributions of $P_{T,H}$, η_H, m_{HH} and y_{HH} for $c_{3H} = 0.5, 1, 2.5, -1$.*

A similar distribution analysis is shown in Figure 24 for c_{HHtt} = -0.5, 0.5, 1 and 0, the SM value.

For $c_{HHtt} > 0$, the destructive interference between the box and the $HHtt$ diagrams explains the dip in the distribution of $P_{T,H}$ and m_{HH}. We can see a significant depletion in the signal for $c_{HHtt} = 1$, and the destructive interference further depletes the signal for $c_{HHtt} = 0.5$. Peaks for $P_{T,H}$ and m_{HH} stay the same as SM expectations, $P_{T,H} \gtrsim 150$ and $m_{HH} \gtrsim 420$. For $c_{HHtt} < 0$, the differential cross-sections for all observables are enhanced due to the constructive interference between the $HHtt$ diagram and the box diagram. The enhancement is large even when c_{HHtt} is just -0.5. For y_{HH} and η_H distribution, the overall shape is the same for different values of the $HHtt$ coupling.

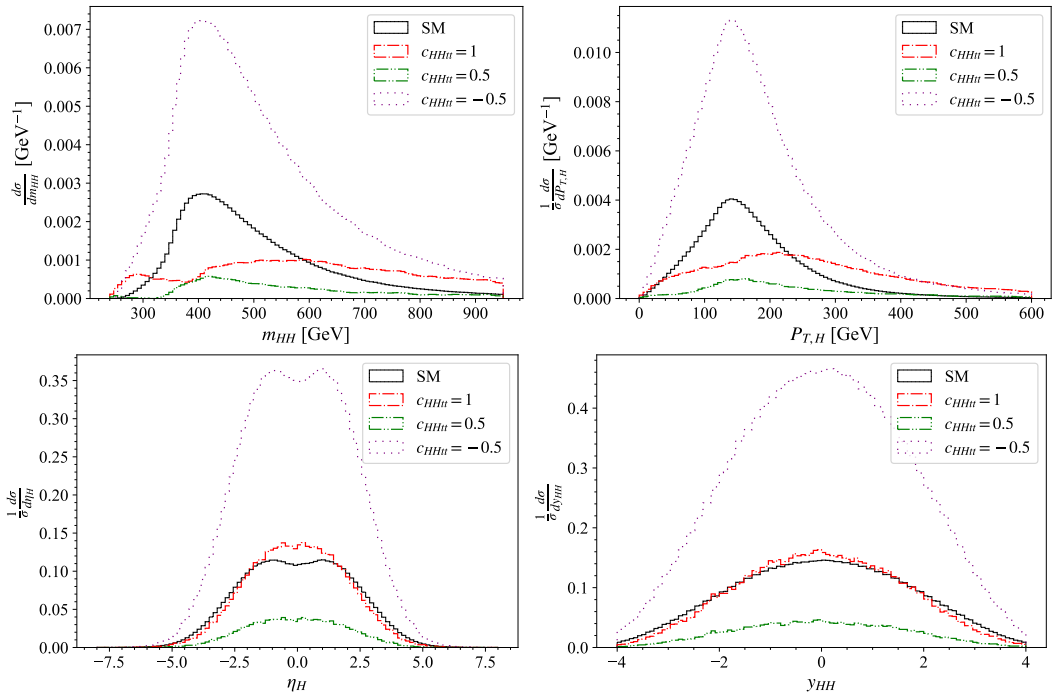

Figure 24. *Distributions of* $P_{T,H}$, η_H, m_{HH} *and* y_{HH} *with* $c_{HHtt} = 1, 0.5, 0, -0.5$.

By using the parameterization introduced in Equation 5.6, the total cross-section of Higgs pair production can be written as

$$\begin{aligned}
\sigma &= \sigma^{SM}\big[c_{3H}^2|\mathcal{M}_{3H}|^2 + c_{Htt}^2|\mathcal{M}_{Htt}|^2 + c_{HHtt}^2|\mathcal{M}_{HHtt}|^2 + c_{HWW}^2|\mathcal{M}_{HWW}|^2 \\
&\quad + c_{HZZ}^2|\mathcal{M}_{HZZ}|^2 + c_{HWW,Htt}^2|\mathcal{M}_{HWW,Htt}|^2 + c_{Hbb}^2|\mathcal{M}_{Hbb}|^2 + c_{Hcc}^2|\mathcal{M}_{Hcc}|^2 \\
&\quad + 2\,c_{3H}c_{Htt}|\mathcal{M}_{3H}\mathcal{M}_{Htt}| + 2\,c_{3H}c_{HHtt}|\mathcal{M}_{3H}\mathcal{M}_{HHtt}| + 2\,c_{3H}c_{HWW}|\mathcal{M}_{3H}\mathcal{M}_{HWW}| \\
&\quad + 2\,c_{3H}c_{HZZ}|\mathcal{M}_{3H}\mathcal{M}_{HZZ}| + 2\,c_{3H}c_{HWW,Htt}|\mathcal{M}_{3H}\mathcal{M}_{HWW,Htt}| \\
&\quad + 2\,c_{3H}c_{Hbb}|\mathcal{M}_{3H}\mathcal{M}_{Hbb}| + 2\,c_{3H}c_{Hcc}|\mathcal{M}_{3H}\mathcal{M}_{Hcc}| \\
&\quad + 2\,c_{Htt}c_{HHtt}|\mathcal{M}_{Htt}\mathcal{M}_{HHtt}| + 2\,c_{Htt}c_{HWW}|\mathcal{M}_{Htt}\mathcal{M}_{HWW}| + \ldots
\end{aligned} \tag{5.8}$$

This expression is lengthy and hard to analyze the effect of changing parameters. Fortunately, $\mathcal{M}_{HWW}$, $\mathcal{M}_{HZZ}$, $\mathcal{M}_{HWW,Htt}$, $\mathcal{M}_{Hbb}$ and $\mathcal{M}_{Hcc}$ are very small compare to $\mathcal{M}_{3H}$, $\mathcal{M}_{Htt}$ and $\mathcal{M}_{HHtt}$ since they comes from QCD_1 contributions. We can therefore safely drop these terms without change the overall properties, and we can write the total cross-section in the following form

$$\begin{aligned}
\sigma &= \sigma^{SM}\big[c_{3H}^2|\mathcal{M}_{3H}|^2 + c_{Htt}^2|\mathcal{M}_{Htt}|^2 + c_{HHtt}^2|\mathcal{M}_{HHtt}|^2 + 2\,c_{3H}c_{Htt}|\mathcal{M}_{3H}\mathcal{M}_{Htt}| \\
&\quad + 2\,c_{3H}c_{HHtt}|\mathcal{M}_{3H}\mathcal{M}_{HHtt}| + 2\,c_{Htt}c_{HHtt}|\mathcal{M}_{Htt}\mathcal{M}_{HHtt}|\big]
\end{aligned} \tag{5.9}$$

For all contributions to the Higgs pair production including $gg \to HH$, $gg \to HHg$, $qg \to HHq$ and $q\bar{q} \to HHg$, we have

$$\sigma = \sigma^{SM}[1.8590\ c_{Htt}^2 + 0.21485\ c_{3H}^2 + 2.9524\ c_{HHtt}^2 - 1.0739\ c_{Htt}c_{3H} \\ -4.1431\ c_{Htt}c_{HHtt} + 1.2271\ c_{3H}c_{HHtt}]. \tag{5.10}$$

A similar result for the LO $gg \to HH$ at $\sqrt{s} = 100$ is calculated in [103]. For the LHC with $\sqrt{s} = 14$, similar numerical coefficients are found. We stress that the coefficient of c_{3H}^2 is around one order of magnitude lower than those of c_{Htt}^2 and c_{HHtt}^2, which agrees with the observation made in [62]. Figure 25 visualize Equation 5.10 by showing new physics effects in the total rate of Higgs production rate to the SM expectation ratio. Recently, the upper bound of the Higgs pair production rate was set to 4.1 times the SM value [120]. In the following discussion, the parameters are allowed to vary between -3 and 3 for c_{Htt} and c_{HHtt}, while c_{3H} is allowed to vary between -8 and 8. In Figure 25(a), c_{Htt} is fixed to unity, its SM value, while c_{HHtt} is allowed to vary. The green region shows the resulting total rate variation, and a strong enhancement can be found on all allowed regions. When $c_{3H} \lesssim -1.5$ or $c_{3H} \gtrsim 4.1$, the production rate is always enhanced. The red dash-dotted, blue-dashed, and black-solid curves represent three reference cases in the plot for $c_{HHtt} = -1$, $c_{HHtt} = 0$, and $c_{HHtt} = 1$, respectively. The yellow band shows where c_{HHtt} is within ± 0.1 of its expected SM value. Even with vanishing or negative, opposite sign to the SM expectation, trilinear Higgs boson coupling, we can see a large area of the parameter space in c_{Htt} and c_{3H}, which reproduce

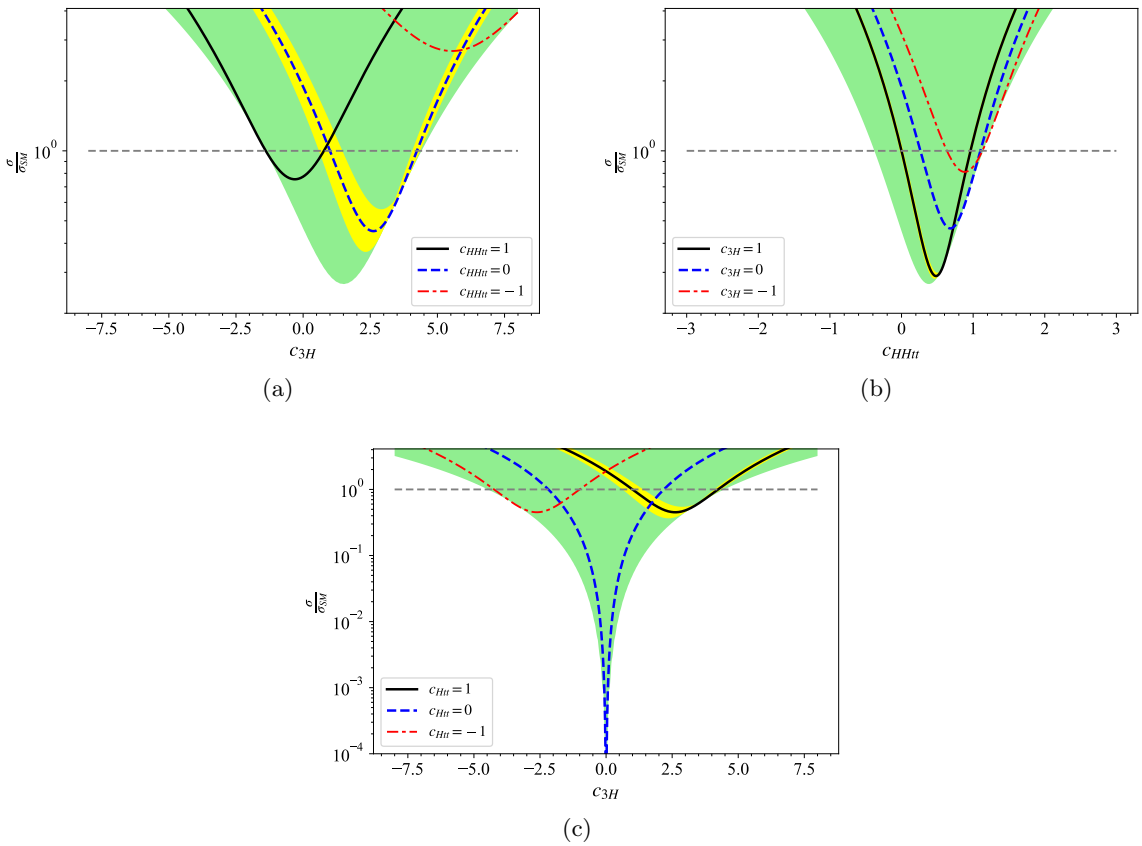

Figure 25. (a) *The ratio of* σ/σ^{SM}*, with varying* c_{HHtt} *and* c_{3H} *while fixing* c_{Htt} *at unity, are shown as the green region. The yellow band denotes the region where* c_{HHtt} *is within* ± 0.1 *of its expected SM value.* c_{HHtt} *is allowed to vary from -3 to 3 and* c_{3H} *is allowed to vary from -8 to 8. The SM rate is the dashed horizontal line.* (b) *Same as* (a)*, but with* c_{HHtt} *along the horizontal axis.* (c) $c_{HHtt} = 0$ *with* c_{Htt} *and* c_{3H} *varying from* -3 *to* 3 *and* -8 *to* 8 *respectively. The yellow band denotes the region where* c_{Htt} *is within* ± 0.1 *of its expected SM value.*

the same cross-section of the Higgs pair production as in the SM. For the case that c_{HHtt} and c_{Htt} are both close to their SM value, the small area around two intersections of the yellow band and the gray dashed line indicates two possible regions of parameter space that allows c_{3H} to produce the expected SM cross-section value. We can set the allowed limit for SM parameter c_{3H} by finding where the SM curve, blue-dashed curve, reaches the observed limit of production cross-section, 4.1 times the Standard Model prediction. Our result agrees with the finding of [120], $-1.5 < c_{3H}^{SM} < 6.7$, and we can easily see that c_{HHtt} parameter greatly expand the allowed limit of c_{3H} to $-5 < c_{3H} < 8$ In Figure 25(b), c_{Htt} is still fixed to unity, but with c_{HHtt} along the horizontal axis. The production cross-section is always enhanced when $c_{HHtt} \lesssim -0.4$ or $c_{HHtt} \gtrsim 1.1$. The yellow band for c_{3H} within ± 0.1 of its expected SM value is very narrow due to the fact that c_{3H} contribution is very small compare to c_{Htt} and c_{HHtt} contributions when $c_{3H} = 1$ (See Figure 21). Again, two possible regions of parameter space allow c_{HHtt} to produce the expected SM cross-section value when c_{3H} and c_{Htt} are both close to their SM value.

In Figure 25(c), we fix c_{HHtt} to be its SM value, zero, and c_{Htt} and c_{3H} are both allowed to vary. The black-solid curve in Figure 25(c) is for the SM c_{Htt} that corresponds to the blue-dashed curve in Figure 25(a). The minimum σ/σ^{SM} ratio occurs at $c_{3H} \lesssim 2.5$ and has a value around 0.45, which agrees with the finding of [24]. Notice that zero production cross-section can only occur trivially when three parameters are all zero, and it becomes a minimum point when we vary c_{HHtt} since each contribution can not cancel each other at every phase space

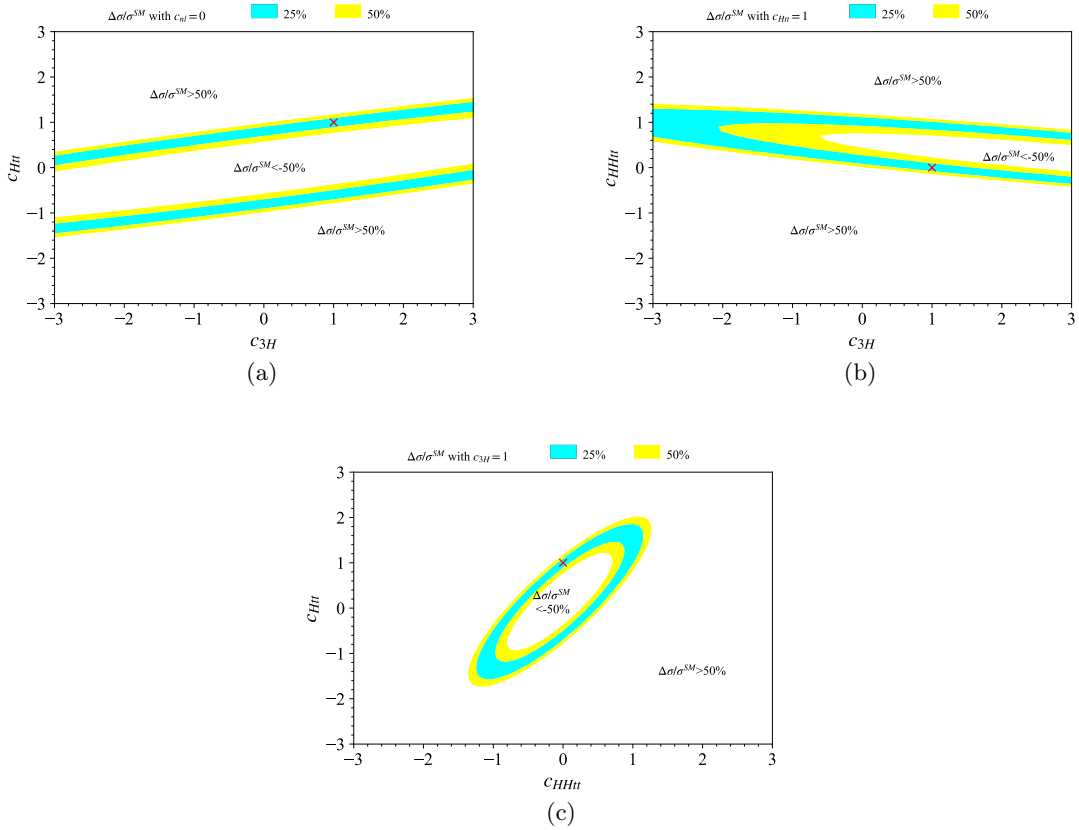

Figure 26. *Cross-section contour plot for $gg \to hh \to \gamma\gamma b\bar{b}$ channel after including the veto cuts in Table III. The parameter space that match the expected SM values within* 25% *and* 50% *are indicated by cyan and yellow areas, respectively. The red cross marks the SM value.*

point, as we can see in Figure 23. The SM total rate for the Higgs pair production could be again reproduced by a large area of the parameter space in c_{3H} and c_{Htt}.

We have discussed that it is possible to discover the Higgs pair production in a 100 TeV pp collider which was already shown in [26, 27, 61]. Then, we study how the event selections affect the extraction of new physics effects in the Higgs pair production. In what follows, the event

selections Table III was imposed again. For the signal analysis, full simulations are performed for parameters within the range $-3 < c_{3H,Htt,HHtt} < 3$. Then, as the partonic case, we can fit the number of selected signal events by a similar function shown in Equation 5.10. The contributions of different diagrams would cause different selection efficiency due to the fact that the kinematic distributions are different for each diagram. However, we can still factor out the parameters c_{Htt}, c_{3H} and c_{HHtt} during the calculations, and this will again give a simple parameterization:

$$\sigma = \sigma^{SM}[3.1265\ c_{HHtt}^2 + 1.5332\ c_{Htt}^2 + 0.072904\ c_{3H}^2 - 3.7322\ c_{Htt}c_{HHtt} \\ -0.60614\ c_{3H}c_{HHtt} + 0.81739\ c_{3H}c_{Htt}]. \tag{5.11}$$

In Figure 26, we consider constraints on c_{Htt}, c_{3H} and c_{HHtt} from measurements of the total cross-section at CM energy of 100 TeV with contour lines go along 25% and 50% deviations from the SM value. For each plot in Figure 26, we vary two of c_{3H}, c_{Htt} and c_{HHtt} and fix the rest to the SM value. For example, in Figure 26(a), c_{Htt} and c_{3H} are allowed to vary within the interval $(-3, 3)$, while $c_{HHtt} = 0$ as in the SM. The cyan and yellow bands represent the parameter spaces that match the result of SM within 25% and 50%, respectively. We see that the sensitivity of cross-section to c_{3H} is low. The same insensitivity persists in Figure 26(b), where we set $c_{Htt} = 1$ as in the SM.

In Figure 26(c), where $c_{3H} = 1$ takes the SM value and c_{Htt}, c_{HHtt} are varying within the interval $(-3, 3)$. Moreover, due to the destructive interference between the triangle and box diagrams, increasing c_{HHtt} can offset any effect of increasing c_{Htt}. Therefore, to explain the various contributions of new physics in double Higgs production, total cross-section alone is not sufficient, and further studies for additional kinematic information are needed.

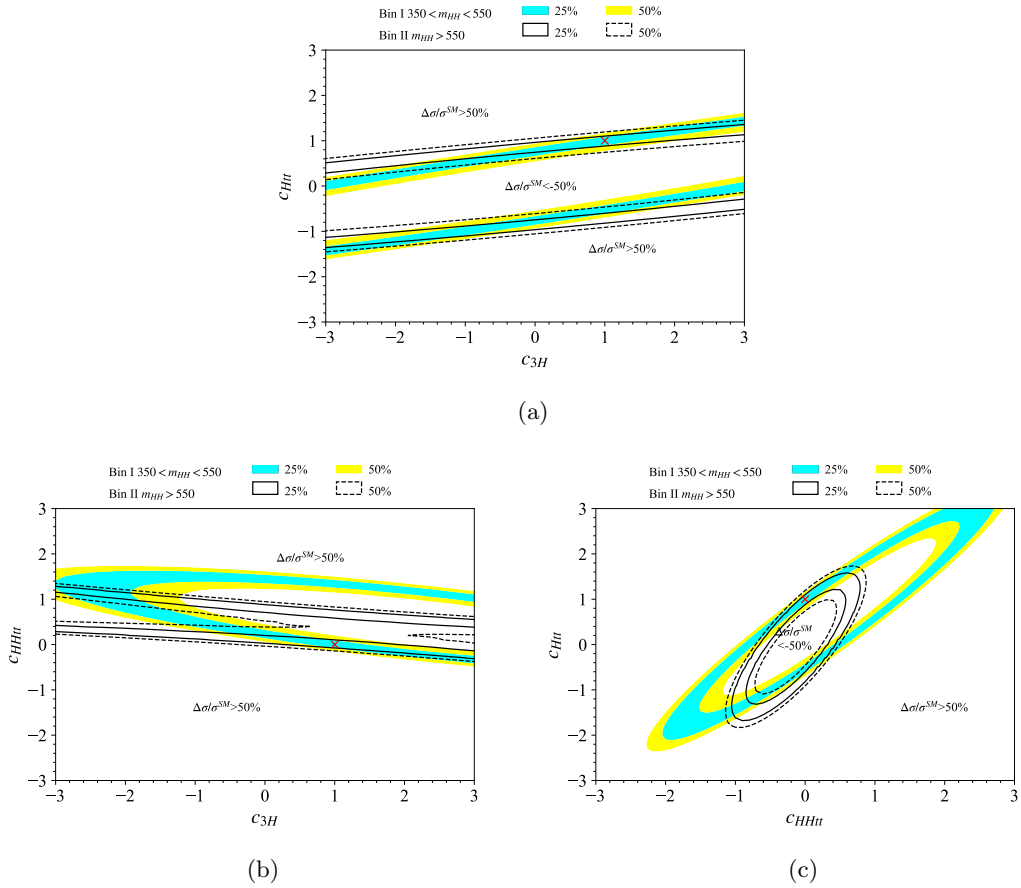

Figure 27. *Contour plots for the cross-sections of a high energy and a low energy bin. Bin I:* 350 $GeV < m_{HH} <$ 550 GeV *and Bin II:* $m_{HH} >$ 550 GeV. *The cross-section matching the value of SM within* 25% *is shown as the cyan region for Bin I and the region between two solid-black curves for Bin II. The cross-section that is within* $25 - 50\%$ *of SM expectation is shown as the yellow region for Bin I and the region between solid and dashed curves for Bin II. The red cross mark the SM value.*

As we have already seen, the contributions of c_{Htt}, c_{3H} and c_{HHtt} have very different distributions of p_T^h and m_{HH}. The c_{3H} component peaks at low m_{HH}, the c_{Htt} peaks at a higher m_{HH}, and the c_{HHtt} shifts the m_{HH} distribution to even larger values. (See Figure 21). Following the analysis in [103], we divide the m_{HH} and p_T distributions into a low bin and a high bin, and the differential cross-section in each bin is used to constrain c_{Htt}, c_{3H}, and c_{HHtt}. We note that fitting the two p_T bins and the two m_{HH} bins give quite similar constraints, which are consistent with the results of [103]. Therefore, in the following, we only show the contour plots of the constraints from fitting the two m_{HH} bins. From Figure 20, the following two m_{HH} bins are chosen in our analysis.

$$\begin{aligned} \text{Bin I} &: 350 \text{ GeV} \leq m_{HH} \leq 550 \text{ GeV} \\ \text{Bin II} &: 550 \text{ GeV} \leq m_{HH} \end{aligned}$$

For Bin I and Bin II, the parameterizations of the cross-sections with respect to c_{Htt}, c_{3H} and c_{HHtt} are given in Equation 5.11.

$$\begin{aligned} \sigma_I &= \sigma_I^{SM}[2.1837\ c_{HHtt}^2 + 1.6984\ c_{Htt}^2 + 0.10647\ c_{3H}^2 - 3.6533\ c_{Htt}c_{HHtt} \\ &\quad -0.80491\ c_{3H}c_{HHtt} + 0.71334\ c_{3H}c_{Htt}]. \\ \sigma_{II} &= \sigma_{II}^{SM}[4.2030\ c_{HHtt}^2 + 1.3446\ c_{Htt}^2 + 0.03458\ c_{3H}^2 - 3.8224\ c_{Htt}c_{HHtt} \\ &\quad -0.37915\ c_{3H}c_{HHtt} + 0.93621\ c_{3H}c_{Htt}]. \end{aligned} \tag{5.12}$$

Figure 27 shows the constraints from the differential cross-section, which lie within 25% and 50% of SM expectations in each bin. Again, two of c_{Htt}, c_{3H}, and c_{HHtt} are allowed to vary, while the other is fixed at the SM value. In Figure 27(a), where c_{HHtt} is fixed while c_{3H} and c_{Htt} are allowed to vary, this set of contours has the largest overlap among all three sets of contours. In Figure 27(b), where $c_{3H} = 1$, we see that there is only a small overlap between the contour from Bin I and Bin II, and the degeneracies in c_{3H} and c_{HHtt} are broken effectively by the measurements in the two bins. In Figure 27(c), where c_{Htt} is allowed to vary, along with c_{HHtt}, we see the non-overlapping region becomes larger than in Figure 27(b). However, the change of c_{Htt} from its SM value is expected to be small due to the precise weak interaction measurements already done. Therefore, the relation present in Figure 27(c) may not be as useful as in Figure 27(b). Our results shown in Figure 27(a) and Figure 27(c) are similar to the finding of [103] by using LO with Higgs effective theory corrections to calculate the cross-section. For the contour shown in Figure 27(b), on the other hand, we have a much larger non-overlapping region near SM expectation compare to the finding of [103]. Therefore full NLO calculations are required due to the effects of event selections on $gg \to HHg$ and $qg \to HHq$ channels. Nonetheless, we note that some degeneracy remains when the differential cross-sections in the low and high bins meet the expected SM values. When it comes to constraining c_{3H}, the situation worsens. However, a significant improvement in constraining c_{3H} from using the measurement of total cross-section alone can still be achieved by including the kinematic information from both low and high m_{HH} bins.

CHAPTER 6

CONCLUSION AND OUTLOOK

In this work, we investigated the use of the kinematic distribution to reveal the new physics effects in the Higgs pair production, including LO channel, $gg \to HH$, and all NLO channels, $gg \to HHg$, $qg \to HHq$, and $qq \to HHg$. We showed that three dimensionless coefficients, c_{Htt}, c_{3H}, and c_{HHtt}, can be used to parameterize the differential cross-section with various new physics effects. We investigated the interactions of different contributions in the p_T spectra and the invariant mass spectra of the Higgs pair. We then numerically study the constraints of these parameters in a 100 TeV proton-proton collider under planning by finding the best fit for the differential rates in a low and a high m_{HH} as well as p_T bins. The constraints from low and high bins ended up being very similar to those from the two p_T bins. Finally, it was found that we can constrain c_{Htt} and c_{HHtt} effectively, despite some degeneracy persists. Moreover, the coefficient c_{3H}, which directly reveals the effect of trilinear Higgs self-coupling, is less constrained. This is roughly consistent with the earlier result in the LO $gg \to HH$ channel [103], full NLO calculations that more effectively break the degeneracy in c_{3H} and c_{HHtt} are therefore required.

Nonetheless, the extra kinematic information from the two invariant mass bins still gives much better results than the total cross-section alone.

Measurements of the trilinear Higgs coupling should be a top priority in upcoming research programs on the Higgs boson, since only the properties of Higgs self-interaction of the 125 GeV

Higgs boson have not been thoroughly tested experimentally. Recent searches [120] for pairs of Higgs bosons in $HH \rightarrow \gamma\gamma b\bar{b}$ process set a limit on the double Higgs production rate of 4.1 times the SM value and created a portal to better understanding the fundamental Higgs mechanism.

The work is far from done. Much more work needs to be done in the phenomenology of double Higgs production. The Matrix Element Method based multivariate analysis [122], which has been applied to the Higgs discovery in the 4ℓ channel [123, 124, 125, 126, 127, 128] and the top quark analyses [129, 130, 131, 132, 133] can be performed to exploit the full kinematic information in the future . Also, the recent search for the Higgs pair performed by the ATLAS collaboration, which applied multivariate analysis based on Boosted Decision Trees (BDT) to event selection in the SM process, obtained the best limit for the double Higgs boson production currently. The same technique can be applied to searches for new physics in the future.

CITED LITERATURE

Bibliography

[1] R. Contino and Others, Physics at a 100 TeV pp collider: Higgs and EW symmetry breaking studies, Cern Yellow Rep. pp. 255–440 (2017), 1606.09408.

[2] A. Abada *et al.*, FCC Physics Opportunities, Eur. Phys. J. C **79**, 474 (2019).

[3] A. Abada *et al.*, FCC-hh: The Hadron Collider, Eur. Phys. J. Spec. Top. **228**, 755 (2019).

[4] G. Aad *et al.*, Observation of a new particle in the search for the Standard Model Higgs boson with the ATLAS detector at the LHC, Phys. Lett. Sect. B Nucl. Elem. Part. High-Energy Phys. **716**, 1 (2012), 1207.7214.

[5] S. Chatrchyan *et al.*, Observation of a new boson at a mass of 125 GeV with the CMS experiment at the LHC, Phys. Lett. Sect. B Nucl. Elem. Part. High-Energy Phys. **716**, 30 (2012), 1207.7235.

[6] A. collaboration, Measurements of the Higgs boson production and decay rates and constraints on its couplings from a combined ATLAS and CMS analysis of the LHC pp collision data at $\sqrt{s} = 7$ and 8 TeV, J. High Energy Phys. **2016** (2016), 1606.02266.

[7] P. W. Higgs, Broken symmetries, massless particlees and gauge fields, Phys. Lett. **12**, 132 (1964).

[8] P. W. Higgs, Broken symmetries and the masses of gauge bosons, Phys. Rev. Lett. **13**, 508 (1964).

[9] P. W. Higgs, Spontaneous symmetry breakdown without massless bosons, Phys. Rev. **145**, 1156 (1966).

[10] F. Englert and R. Brout, Broken symmetry and the mass of gauge vector mesons, Phys. Rev. Lett. **13**, 321 (1964).

[11] G. S. Guralnik, C. R. Hagen, and T. W. Kibble, Global conservation laws and massless particles, Phys. Rev. Lett. **13**, 585 (1964).

[12] T. W. Kibble, Symmetry breaking in n-Abelian gauge theories, Phys. Rev. **155**, 1554 (1967).

[13] ATLAS Collaboration, Update of the Combination of Higgs Boson Searches in 1.0 to 2.3 fb^{-1} of pp Collisions Data Taken at $\sqrt{s} = 7$ TeV with the ATLAS Experiment at the LHC, Cern. Geneva Switz. (2011).

[14] C. collaboration, Combined results of searches for a Higgs boson in the context of the standard model and beyond-standard models, Hig-12-008 **600** (2012).

[15] C. Anastasiou, R. Boughezal, and E. Furlan, The NNLO gluon fusion Higgs production cross-section with many heavy quarks, J. High Energy Phys. **2010** (2010), 1003.4677.

[16] C. Anastasiou, S. Buehler, E. Furlan, F. Herzog, and A. Lazopoulos, Higgs production cross-section in a Standard Model with four generations at the LHC, Phys. Lett. Sect. B Nucl. Elem. Part. High-Energy Phys. **702**, 224 (2011), 1103.3645.

[17] A. Djouadi and A. Lenz, Sealing the fate of a fourth generation of fermions, Phys. Lett. Sect. B Nucl. Elem. Part. High-Energy Phys. **715**, 310 (2012), 1204.1252.

[18] A. Denner, S. Dittmaier, A. Mück, G. Passarino, M. Spira, C. Sturm, S. Uccirati, and M. M. Weber, Higgs production and decay with a fourth Standard-Model-like fermion generation, Eur. Phys. J. C **72**, 1 (2012), 1111.6395.

[19] O. Eberhardt, G. Herbert, H. Lacker, A. Lenz, A. Menzel, U. Nierste, and M. Wiebusch, Impact of a Higgs boson at a mass of 126 GeV on the standard model with three and four fermion generations, Phys. Rev. Lett. **109** (2012), 1209.1101.

[20] V. Khachatryan *et al.*, Precise determination of the mass of the Higgs boson and tests of compatibility of its couplings with the standard model predictions using proton collisions at 7 and 8 TeV, Eur. Phys. J. C **75** (2015), 1412.8662.

[21] ATLAS Collaboration, Combined measurements of the Higgs boson production and decay rates in $H \to ZZ^* \to 4\ell$ and $H \to \gamma\gamma$ final states using pp collision data at $\sqrt{s} = 13$ TeV in the ATLAS experiment, ATLAS-CONF-2016-081 (2016).

[22] G. Degrassi, P. Giardino, F. Maltoni, and D. Pagani, Probing the Higgs self coupling via single Higgs production at the LHC, J. High Energy Phys. **2016**, 80 (2016).

[23] G. Degrassi, M. Fedele, and P. Giardino, Constraints on the trilinear Higgs self coupling from precision observables, J. High Energy Phys. **2017**, 155 (2017).

[24] J. Baglio, F. Campanario, S. Glaus, M. Mühlleitner, J. Ronca, M. Spira, and J. Streicher, Higgs-pair production via gluon fusion at hadron colliders: NLO QCD corrections, J. High Energy Phys. **2020** (2020).

[25] X. Li and M. B. Voloshin, Remarks on double Higgs boson production by gluon fusion at threshold, Phys. Rev. D - Part. Fields, Gravit. Cosmol. **89** (2014), 1311.5156.

[26] J. Baglio, A. Djouadi, R. Gröber, M. M. Mühlleitner, J. Quevillon, and M. Spira, The measurement of the Higgs self-coupling at the LHC: Theoretical status, J. High Energy Phys. **2013** (2013), 1212.5581.

[27] W. Yao, Studies of measuring Higgs self-coupling with $HH \to b\bar{b}\gamma\gamma$ at the future hadron colliders **1**, 8 (2013), 1308.6302.

[28] O. J. Éboli, G. C. Marques, S. F. Novaes, and A. A. Natale, Twin Higgs-boson production, Phys. Lett. B **197**, 269 (1987).

[29] E. W. Glover and J. J. van der Bij, Higgs boson pair production via gluon fusion, Nucl. Physics, Sect. B **309**, 282 (1988).

[30] D. A. Dicus, C. Kao, and S. S. Willenbrock, Higgs boson pair production from gluon fusion, Phys. Lett. B **203**, 457 (1988).

[31] T. Plehn, M. Spira, and P. M. Zerwas, Pair production of neutral Higgs particles in gluon-gluon collisions, Nucl. Phys. B **479**, 46 (1996), 9603205.

[32] A. Dobrovolskaya and V. Novikov, On heavy Higgs boson production, Zeitschrift für Phys. C Part. Fields **52**, 427 (1991).

[33] D. A. Dicus, K. J. Kallianpur, and S. S. Willenbrock, Higgs boson pair production in the effective-W approximation, Phys. Lett. B **200**, 187 (1988).

[34] W.-Y. Keung, DOUBLE HIGGS FROM W-W FUSION, Mod. Phys. Lett. A **02**, 765 (1987).

[35] A. Abbasabadi, W. W. Repko, D. A. Dicus, and R. Vega, Comparison of exact and effective-gauge-boson calculations for gauge-boson fusion processes, Phys. Rev. D **38**, 2770 (1988).

[36] V. Barger, T. Han, and R. J. Phillips, Double Higgs-boson bremsstrahlung from W and Z bosons at supercolliders, Phys. Rev. D **38**, 2766 (1988).

[37] M. Moretti, S. Moretti, F. Piccinini, R. Pittau, and A. D. Polosa, Higgs boson self-couplings at the LHC as a probe of extended Higgs sectors, J. High Energy Phys. **2005**, 603 (2005).

[38] T. Plehn and M. Rauch, Quartic Higgs coupling at hadron colliders, Phys. Rev. D **72**, 053008 (2005).

[39] T. Binoth, S. Karg, N. Kauer, and R. Rückl, Multi-Higgs boson production in the standard model and beyond, Phys. Rev. D **74**, 113008 (2006).

[40] B. Fuks, J. H. Kim, and S. J. Lee, Probing Higgs boson self-interactions in proton-proton collisions at a center-of-mass energy of 100 TeV, Phys. Rev. D **93**, 035026 (2016).

[41] D. de Florian and J. Mazzitelli, Two-loop corrections to the triple Higgs boson production cross section, J. High Energy Phys. **2017**, 107 (2017).

[42] D. de Florian, I. Fabre, and J. Mazzitelli, Triple Higgs production at hadron colliders at NNLO in QCD, J. High Energy Phys. **2020** (2020), 1912.02760.

[43] T. Liu, K.-F. Lyu, J. Ren, and H. X. Zhu, Probing the quartic Higgs boson self-interaction, Phys. Rev. D **98**, 093004 (2018).

[44] W. Bizoń, U. Haisch, and L. Rottoli, Constraints on the quartic Higgs self-coupling from double-Higgs production at future hadron colliders, J. High Energy Phys. **2019**, 267 (2019).

[45] S. Borowka, C. Duhr, F. Maltoni, D. Pagani, A. Shivaji, and X. Zhao, Probing the scalar potential via double Higgs boson production at hadron colliders, J. High Energy Phys. **2019**, 16 (2019).

[46] S. Borowka, N. Greiner, G. Heinrich, S. P. Jones, M. Kerner, J. Schlenk, U. Schubert, and T. Zirke, Higgs Boson Pair Production in Gluon Fusion at Next-to-Leading Order with Full Top-Quark Mass Dependence [Phys. Rev. Lett. 117 , 012001 (2016)], Phys. Rev. Lett. **117**, 079901 (2016).

[47] S. Borowka, N. Greiner, G. Heinrich, S. Jones, M. Kerner, J. Schlenk, and T. Zirke, Full top quark mass dependence in Higgs boson pair production at NLO, J. High Energy Phys. **2016**, 107 (2016).

[48] J. Baglio, F. Campanario, S. Glaus, M. Mühlleitner, M. Spira, and J. Streicher, Gluon fusion into Higgs pairs at NLO QCD and the top mass scheme, Eur. Phys. J. C **79**, 459 (2019).

[49] D. de Florian and J. Mazzitelli, Two-loop virtual corrections to Higgs pair production, Phys. Lett. B **724**, 306 (2013).

[50] D. de Florian and J. Mazzitelli, Higgs Boson Pair Production at Next-to-Next-to-Leading Order in QCD, Phys. Rev. Lett. **111**, 201801 (2013).

[51] J. Grigo, K. Melnikov, and M. Steinhauser, Virtual corrections to Higgs boson pair production in the large top quark mass limit, Nucl. Phys. B **888**, 17 (2014), 1408.2422.

[52] M. Spira, Effective multi-Higgs couplings to gluons, J. High Energy Phys. **2016** (2016), 1607.05548.

[53] P. Banerjee, S. Borowka, P. K. Dhani, T. Gehrmann, and V. Ravindran, Two-loop massless QCD corrections to the g + g $\to$ H + H four-point amplitude, J. High Energy Phys. **2018**, 130 (2018).

[54] L. B. Chen, H. T. Li, H. S. Shao, and J. Wang, Higgs boson pair production via gluon fusion at N3LO in QCD, Phys. Lett. Sect. B Nucl. Elem. Part. High-Energy Phys. **803** (2020), 1909.06808.

[55] L. B. Chen, H. T. Li, H. S. Shao, and J. Wang, The gluon-fusion production of Higgs boson pair: N3LO QCD corrections and top-quark mass effects, J. High Energy Phys. **2020** (2020), 1912.13001.

[56] G. Heinrich, S. P. Jones, M. Kerner, G. Luisoni, and E. Vryonidou, NLO predictions for Higgs boson pair production with full top quark mass dependence matched to parton showers, J. High Energy Phys. **2017** (2017), 1703.09252.

[57] S. Jones and S. Kuttimalai, Parton shower and NLO-matching uncertainties in Higgs boson pair production, J. High Energy Phys. **2018** (2018), 1711.03319.

[58] M. Grazzini, G. Heinrich, S. Jones, S. Kallweit, M. Kerner, J. M. Lindert, and J. Mazzitelli, Higgs boson pair production at NNLO with top quark mass effects, J. High Energy Phys. **2018** (2018), 1803.02463.

[59] C. O. Dib, R. Rosenfeld, and A. Zerwekh, Double Higgs production and quadratic divergence cancellation in little Higgs models with T-parity, J. High Energy Phys. **2006** (2006), 0509179.

[60] R. Gröber and M. Mühlleitner, Composite Higgs boson pair production at the LHC, J. High Energy Phys. **2011** (2011), 1012.1562.

[61] H.-J. He, J. Ren, and W. Yao, Probing New Physics of Cubic Higgs Interaction via Higgs Pair Production at Hadron Colliders (2015), 1506.03302.

[62] R. Contino, M. Ghezzi, M. Moretti, G. Panico, F. Piccinini, and A. Wulzer, Anomalous couplings in double Higgs production, J. High Energy Phys. **2012** (2012), 1205.5444.

[63] R. P. Feynman, Space-Time Approach to Quantum Electrodynamics, Phys. Rev. **76**, 769 (1949).

[64] S. Tomonaga, On a Relativistically Invariant Formulation of the Quantum Theory of Wave Fields*, Prog. Theor. Phys. **1**, 27 (1946).

[65] J. Schwinger, Quantum Electrodynamics. I. A Covariant Formulation, Phys. Rev. **74**, 1439 (1948).

[66] C. N. Yang and R. L. Mills, Conservation of Isotopic Spin and Isotopic Gauge Invariance, Phys. Rev. **96**, 191 (1954).

[67] S. L. Glashow, Partial-symmetries of weak interactions, Nucl. Phys. **22**, 579 (1961).

[68] A. Salam, in Elementary Particle Theory, ed. N. Svartholm (Almqvist and Wiksell, Stockholm, 1968) p. 367.

[69] S. Weinberg, A Model of Leptons, Phys. Rev. Lett. **19**, 1264 (1967).

[70] D. J. Gross and F. Wilczek, Ultraviolet Behavior of Non-Abelian Gauge Theories, Phys. Rev. Lett. **30**, 1343 (1973).

[71] H. D. Politzer, Reliable Perturbative Results for Strong Interactions?, Phys. Rev. Lett. **30**, 1346 (1973).

[72] J. J. Aubert *et al.*, Experimental Observation of a Heavy Particle J, Phys. Rev. Lett. **33**, 1404 (1974).

[73] J. E. Augustin *et al.*, Discovery of a Narrow Resonance in e^+e^- Annihilation, Phys. Rev. Lett. **33**, 1406 (1974).

[74] F. Dydak, in 'Proceedings of the 25th International Conference on High Energy Physics', eds. K. K. Phua and Y. Yamaguchi, World Scientific, Singapore (1991) **1**, 3.

[75] G. 'tHooft, Renormalizable Lagrangians for massive Yang-Mills fields, Nucl. Phys. B **35**, 167 (1971).

[76] G. 'tHooft, Renormalization of massless Yang-Mills fields, Nucl. Phys. B **33**, 173 (1971).

[77] M. Green and M. Veltman, Weak and E.M. radiative corrections to low-energy processes, Nucl. Phys. B **169**, 137 (1980).

[78] M. Consoli, One-loop corrections to $e^+e^- \to e^+e^-$ in the weinberg model, Nucl. Phys. B **160**, 208 (1979).

[79] G. 't Hooft and M. Veltman, Scalar one-loop integrals, Nucl. Phys. B **153**, 365 (1979).

[80] D. B. Melrose, Reduction of feynman diagrams, Nuovo Cim. A **40**, 181 (1965).

[81] A. Denner, U. Nierste, and R. Scharf, A compact expression for the scalar one-loop four-point function, Nucl. Phys. B **367**, 637 (1991).

[82] A. Denner and S. Dittmaier, Reduction of one-loop tensor 5-point integrals, Nucl. Phys. B **658**, 175 (2003).

[83] A. Denner and S. Dittmaier, Reduction schemes for one-loop tensor integrals, Nucl. Phys. B **734**, 62 (2006).

[84] A. Denner, S. Dittmaier, and L. Hofer, Collier: A fortran-based complex one-loop library in extended regularizations, Comput. Phys. Commun. **212**, 220 (2017).

[85] G. 't Hooft and M. Veltman, Regularization and renormalization of gauge fields, Nucl. Physics, Sect. B **44**, 189 (1972).

[86] W. L. van Neerven and J. A. M. Vermaseren, Large loop integrals, Phys. Lett. B **137**, 241 (1984).

[87] Z. Bern, L. Dixon, and D. A. Kosower, Dimensionally regulated one-loop integrals, Phys. Lett. B **302**, 299 (1993).

[88] R. G. Stuart, Algebraic reduction of Feynman diagrams to scalar integrals: A Mathematica implementation of LERG-I, Comput. Phys. Commun. **85**, 267 (1995), 9409273.

[89] G. van Oldenborgh, FF — a package to evaluate one-loop Feynman diagrams, Comput. Phys. Commun. **66**, 1 (1991).

[90] A. Denner, Techniques for the Calculation of Electroweak Radiative Corrections at the One-Loop Level and Results forW-physics at LEP 200, Fortschritte der Phys. Phys. **41**, 307 (1993).

[91] A. Denner, S. Dittmaier, and M. Roth, Non-factorizable photonic corrections to e+e- → WW → 4 fermions, Nucl. Phys. B **519**, 39 (1998), 9710521.

[92] R. Guth and J. Kühn, Top-quark threshold and radiative corrections, Nucl. Phys. B **368**, 38 (1992).

[93] B. Grządkowski, J. Kühn, P. Krawczyk, and R. Stuart, Electroweak corrections on the toponium resonance, Nucl. Phys. B **281**, 18 (1987).

[94] G. Ossola, C. G. Papadopoulos, and R. Pittau, Reducing full one-loop amplitudes to scalar integrals at the integrand level, Nucl. Phys. B **763**, 147 (2007), 0609007.

[95] G. Ossola, C. G. Papadopoulos, and R. Pittau, Numerical evaluation of six-photon amplitudes, J. High Energy Phys. **2007**, 085 (2007).

[96] G. Ossola, C. G. Papadopoulos, and R. Pittau, CutTools: A program implementing the OPP reduction method to compute one-loop amplitudes, J. High Energy Phys. **2008**, 042 (2008).

[97] V. Barger, T. Han, P. Langacker, B. McElrath, and P. Zerwas, Effects of genuine dimension-six Higgs operators, Phys. Rev. D **67**, 115001 (2003).

[98] F. Boudjema and E. Chopin, Double Higgs production at the linear colliders and the probing of the Higgs self-coupling, Zeitschrift fur Phys. C-Particles Fields **73**, 85 (1997), 9507396.

[99] E. Asakawa, D. Harada, S. Kanemura, Y. Okada, and K. Tsumura, Higgs boson pair production in new physics models at hadron, lepton, and photon colliders, Phys. Rev. D - Part. Fields, Gravit. Cosmol. **82**, 115002 (2010), 1009.4670.

[100] P. N. Pandita and P. Osland, Measuring the trilinear couplings of MSSM neutral Higgs bosons at high-energy e^+e^- colliders, Phys. Rev. D - Part. Fields, Gravit. Cosmol. **59**, 055013 (1999).

[101] A. Djouadi, W. Kilian, M. Mühlleitner, and P. M. Zerwas, Production of neutral Higgs-boson pairs at LHC, Eur. Phys. J. C **10**, 45 (1999).

[102] R. Gröber and M. Mühlleitner, Composite Higgs boson pair production at the LHC, J. High Energy Phys. **2011** (2011).

[103] C.-R. Chen and I. Low, Double take on new physics in double Higgs boson production, Phys. Rev. D **90**, 013018 (2014).

[104] M. Gillioz, R. Gröber, C. Grojean, M. Mühlleitner, and E. Salvioni, Higgs low-energy theorem (and its corrections) in composite models, J. High Energy Phys. **2012** (2012), 1206.7120.

[105] S. Dawson, E. Furlan, and I. Lewis, Unravelling an extended quark sector through multiple higgs production?, Phys. Rev. D - Part. Fields, Gravit. Cosmol. **87** (2013), 1210.6663.

[106] J. Ellis, M. K. Gaillard, and D. Nanopoulos, A phenomenological profile of the Higgs boson, Nucl. Phys. B **106**, 292 (1976).

[107] F. Maltoni, E. Vryonidou, and M. Zaro, Top-quark mass effects in double and triple Higgs production in gluon-gluon fusion at NLO, J. High Energy Phys. **2014** (2014), 1408.6542.

[108] T. Hahn, Generating Feynman diagrams and amplitudes with FeynArts 3, Comput. Phys. Commun. **140**, 418 (2001).

[109] T. Hahn and M. Pérez-Victoria, Automated one-loop calculations in four and D dimensions, Comput. Phys. Commun. **118**, 153 (1999).

[110] R. Frederix, S. Frixione, V. Hirschi, D. Pagani, H. S. Shao, and M. Zaro, The automation of next-to-leading order electroweak calculations, J. High Energy Phys. **2018** (2018), 1804.10017.

[111] J. Butterworth *et al.*, PDF4LHC recommendations for LHC Run II, J. Phys. G Nucl. Part. Phys. **43**, 023001 (2016).

[112] T. Sjöstrand, S. Ask, J. R. Christiansen, R. Corke, N. Desai, P. Ilten, S. Mrenna, S. Prestel, C. O. Rasmussen, and P. Z. Skands, An introduction to PYTHIA 8.2, Comput. Phys. Commun. **191**, 159 (2015), 1410.3012.

[113] J. De Favereau, C. Delaere, P. Demin, A. Giammanco, V. Lemaître, A. Mertens, and M. Selvaggi, DELPHES 3: A modular framework for fast simulation of a generic collider experiment, J. High Energy Phys. **2014** (2014), 1307.6346.

[114] C. Degrande, C. Duhr, B. Fuks, D. Grellscheid, O. Mattelaer, and T. Reiter, UFO - The Universal FeynRules Output, Comput. Phys. Commun. **183**, 1201 (2012), 1108.2040.

[115] A. D. Martin, W. J. Stirling, R. S. Thorne, and G. Watt, Parton distributions for the LHC, Eur. Phys. J. C **63**, 189 (2009), 0901.0002.

[116] U. Baur, T. Plehn, and D. Rainwater, Measuring the Higgs boson self-coupling at the large hadron collider, Phys. Rev. Lett. **89**, 151801/1 (2002), 0206024.

[117] U. Baur, T. Plehn, and D. Rainwater, Determining the Higgs boson self-coupling at hadron colliders, Phys. Rev. D - Part. Fields, Gravit. Cosmol. **67**, 033003 (2003), 0211224.

[118] U. Baur, T. Plehn, and D. Rainwater, Examining the Higgs boson potential at lepton and hadron colliders: A comparative analysis, Phys. Rev. D **68**, 033001 (2003).

[119] U. Baur, T. Plehn, and D. Rainwater, Probing the Higgs self-coupling at hadron colliders using rare decays, Phys. Rev. D - Part. Fields, Gravit. Cosmol. **69**, 053004 (2004), 0310056.

[120] R. Owen and S. R. A. Laboratory, Higgs physics results at ATLAS on behalf of the ATLAS Collaboration, Technical report (2021).

[121] Performance assumptions for an upgraded ATLAS detector at a High-Luminosity LHC (2013).

[122] K. Kondo, Dynamical Likelihood Method for Reconstruction of Events with Missing Momentum. I. Method and Toy Models, J. Phys. Soc. Japan **57**, 4126 (1988).

[123] S. Chatrchyan *et al.*, Measurement of the properties of a Higgs boson in the four-lepton final state, Phys. Rev. D - Part. Fields, Gravit. Cosmol. **89** (2014), 1312.5353.

[124] A. De Rújula, J. Lykken, M. Pierini, C. Rogan, and M. Spiropulu, Higgs boson look-alikes at the LHC, Phys. Rev. D - Part. Fields, Gravit. Cosmol. **82** (2010), 1001.5300.

[125] J. S. Gainer, K. Kumar, I. Low, and R. Vega-Morales, Improving the sensitivity of Higgs boson searches in the golden channel, J. High Energy Phys. **2011** (2011), 1108.2274.

[126] Y. Gao, A. V. Gritsan, Z. Guo, K. Melnikov, M. Schulze, and N. V. Tran, Spin determination of single-produced resonances at hadron colliders, Phys. Rev. D - Part. Fields, Gravit. Cosmol. **81** (2010), 1001.3396.

[127] S. Chatrchyan *et al.*, Study of the mass and spin-parity of the Higgs boson candidate via its decays to Z boson pairs, Phys. Rev. Lett. **110** (2013), 1212.6639.

[128] S. Chatrchyan *et al.*, Observation of a new boson with mass near 125 GeV in pp collisions at $\sqrt{s}$ =7 and 8 TeV, J. High Energy Phys. **2013** (2013), 1303.4571.

[129] R. H. Dalitz and G. R. Goldstein, Decay and polarization properties of the top quark, Phys. Rev. D **45**, 1531 (1992).

[130] B. Abbott *et al.*, Measurement of the top quark mass in the dilepton channel, Phys. Rev. D - Part. Fields, Gravit. Cosmol. **60** (1999), 9808029.

[131] T. Aaltonen *et al.*, Measurement of the single-top-quark production cross section at CDF, Phys. Rev. Lett. **101** (2008), 0809.2581.

[132] A. Abulencia *et al.*, Top quark mass measurement from dilepton events at CDF II with the matrix-element method, Phys. Rev. D - Part. Fields, Gravit. Cosmol. **74** (2006), 0605118.

[133] V. M. Abazov *et al.*, Evidence for production of single top quarks, Phys. Rev. D - Part. Fields, Gravit. Cosmol. **78** (2008), 0803.0739.

VITA

NAME:	Bo-Yan Huang
EDUCATION:	B.A., Physics, National Tsing Hua University, Hsing Chu, Taiwan, 2006 M.S., Physics, National Taiwan University, Taipei, Taiwan, 2008
TEACHING	Department of Physics, University of Illinois at Chicago, Chicago, Illinois, 2013-2020
HONORS	Raccah Award, Department of Physics, University of Illinois at Chicago, Chicago, Illinois, 2012
Publications	Yuan Chao, Kai-Feng Chen, Shing-Kuo Chen, Wei-Shu Hou, Bo-Yan Huang, and Yeong-Jyi Lei.: Threshold effects in the decay of heavy b' and t' quarks. Phys. Rev. D 84, 014029, 2011.